②

GL-TR-90-0311

High-Altitude Non-Equilibrium
Infrared Emission Models

Peter P. Wintersteiner
Robert A. Joseph
Armand J. Paboojian

ARCON Corporation
260 Bear Hill Road
Waltham, MA 02154

AD-A232 503

30 November 1990

Final Report
11 June 1986-30 November 1990

DTIC
S ELECTE D
FEB 26 1991
B

GEOPHYSICS LABORATORY
AIR FORCE SYSTEMS COMMAND
UNITED STATES AIR FORCE
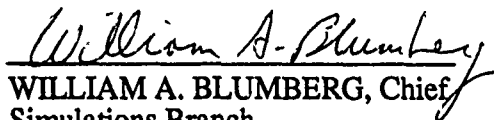HANSCOM AIR FORCE BASE. MASSACHUSETTS, 01731-5000

91 2 25 069

"This technical report has been reviewed and is approved for publication"

RICHARD H. PICARD
Contract Manager
Simulations Branch
Optical Environment Division

WILLIAM A. BLUMBERG, Chief
Simulations Branch
Optical Environment Division

FOR THE COMMANDER

R. EARL GOOD, SES, Director
Optical Environment Division

REPORT DOCUMENTATION PAGE

1. AGENCY USE ONLY (Leave blank)	2. REPORT DATE	3. REPORT TYPE AND DATES COVERED
	30 November 1990	Final, 11 June 1986 – 30 November 1990

4. TITLE AND SUBTITLE	5. FUNDING NUMBERS
High-Altitude Non-Equilibrium Infrared Emission Models	F19628-86-C-0118
6. AUTHOR(S)	PE61102F
Peter P. Wintersteiner Robert A. Joseph Armand J. Paboojian	P2310 TA G5 WUAB

7. PERFORMING ORGANIZATION NAME(S) AND ADDRESS(ES)	8. PERFORMING ORGANIZATION REPORT NUMBER
ARCON Corporation 260 Bear Hill Road Waltham, MA 02154	N/A

9. SPONSORING/MONITORING AGENCY NAME(S) AND ADDRESS(ES)	10. SPONSORING/MONITORING AGENCY REPORT NUMBER
Geophysics Laboratory Hanscom AFB, MA 01731 Contract Manager, Richard H. Picard/OPS	GL-TR-90-0311

11. SUPPLEMENTARY NOTES

N/A

12a. DISTRIBUTION/AVAILABILITY STATEMENT	12b. DISTRIBUTION CODE
Approved for public release; distribution unlimited	

13. ABSTRACT (Maximum 200 words)

In this report we decribe the development and implementation of models for predicting infrared emission in non-LTE regions of the Earth's atmosphere. Such models are used to simulate particular atmospheric conditions, both quiescent and aurorally-disturbed, in order to extract information from infrared radiance data sets and study the roles of different basic physical processes affecting the upper atmosphere. Specifically, we have developed the first line-by-line radiative excitation model for the upper atmosphere, RAD, applied it to the calculation of populations of infrared-active states of CO_2 and CO, simulated the conditions of the SPIRE experiment, and elucidated the role of atomic oxygen in exciting the CO_2 bending modes. We have modeled auroral emissions, analyzed the Field Widened Interferometer data set using a method of spectral decomposition, and identified NO band heads in the lower-thermosphere emissions. We describe the mathematical procedures underlying our models, especially the RAD model, and the physical processes incorporated in them. We present detailed results from running the models. We also report, briefly, on the current status of codes that we have developed.

14. SUBJECT TERMS		15. NUMBER OF PAGES
Infrared emission; upper atmosphere; auroral radiance; non-LTE; AARC; line-by-line radiative transfer; RAD; CO_2; CO; NO; SPIRE; FWI; band heads; spectral decomposition		130
		16. PRICE CODE

17. SECURITY CLASSIFICATION OF REPORT	18. SECURITY CLASSIFICATION OF THIS PAGE	19. SECURITY CLASSIFICATION OF ABSTRACT	20. LIMITATION OF ABSTRACT
Unclassified	Unclassified	Unclassified	UL

TABLE OF CONTENTS

PREFACE

The analysis, computer programs, and results discussed in this report are the result of analytical research performed for:

Geophysics Laboratory
Hanscom Air Force Base, MA 01731.

Throughout the duration of this contract, we have worked closely with Dr. Richard Picard, Dr. Ramesh Sharma, and Dr. Jeremy Winick of the Geophysics Lab. We have benefited greatly from their ideas and suggestions, and we would like to acknowledge their cooperation and support as having been instrumental in the success of our efforts.

Accession For	
NTIS GRA&I	☑
DTIC TAB	☐
Unannounced	☐
Justification	
By	
Distribution/	
Availability Codes	
Dist	Avail and/or Special
A-1	

v

INTRODUCTION

Infrared emissions from the upper atmosphere play an important role in the establishment of the heat balance, structure, and dynamical properties of the atmosphere as a whole. During the last four years, we have devoted considerable effort to constructing, testing, validating, and running models for infrared emission in the non-LTE regions of the terrestrial atmosphere. These state-of-the-art models have contributed to the understanding of radiative transfer processes in the quiescent and aurorally-disturbed upper atmosphere, and to the understanding of other basic physical processes. They are being used to simulate particular experimental conditions in order to extract information from existing data sets, and to predict infrared emissions for various conditions for which future data are anticipated. They are used as benchmark calculations for validating certain results from scene generators and large codes such as NORSE and SHARC, and have also been used to provide up-to-date vibrational temperature profiles for FASCODE.

This report describes the work accomplished under the provisions of contract F19628-86-C-0118. It has six principal sections, following this introduction. The first describes the formulation of the line-by-line infrared radiative excitation algorithm, RAD, which is an integral part of several models. The next three sections deal with its application to $CO_2(\nu_2)$ states, $CO_2(\nu_3)$ states, and the $CO(v=1)$ state. These models calculate the populations of infrared emitting states in the quiescent atmosphere and allow one to predict radiance levels that one might observe under a wide range of conditions.

Section V deals with problems associated with the aurora. It touches on the Auroral Atmospheric Radiance Code (AARC), the Geophysics Laboratory's auroral infrared code for which we have had much of the responsibility. It also discusses certain results from the Field Widened Interferometer (FWI) experiment. The last section reports briefly on the status of application codes that we have written or improved during the time this contract was in effect.

The equations, figures, and tables are numbered consecutively through all sections. References for all sections are listed together at the end, in alphabetical order of the first authors' names.

1

I. THE RAD ALGORITHM

We have developed a state of the art algorithm for infrared radiative transport in the upper atmosphere. The RAD algorithm calculates the rate of absorption of infrared photons due to emission occurring throughout the the entire atmosphere. This quantity, evaluated at discrete altitudes, is an essential component of any calculation of the populations of excited vibrational states that have strong infrared transitions; in many cases, the radiative transport is solely responsible for the non-LTE nature of the population distributions. We have incorporated the RAD algorithm into models that determine the vibrational populations of excited states of CO_2 and CO.

The RAD algorithm is unique in that it is a line-by-line (LBL) calculation. Existing models (e.g., *Lopez-Puertas et al, 1986a, 1986b*) have either relied upon a single source function, describing the emission from a single vibrational state into a rovibrational band as a whole, or else a few source functions describing coupled vibrational states with each one emitting into an entire band. The line-by-line approach uses source functions for individual rovibrational transitions. This allows it to take advantage of the individual line data compiled in the HITRAN molecular absorption parameters database *(Rothman et al, 1987)*. It is thus possible to incorporate the full altitude dependence of the Voigt emission and absorption lineshapes, for each line in each atmospheric layer, so that the monochromatic transfer functions reflect the proper temperature and pressure dependence of the all intervening layers. The full altitude dependence of the linestrengths—for example, due to the correction for lower-state populations—is also utilized. An efficient semiadaptive integration scheme allows us to account for absorption as far out into the wings as is necessary for each line. As a result of all this, the exchange of photons between atmospheric layers is calculated very accurately. Moreover, the contribution of each atmospheric source layer to the total radiative excitation at any given point is easily retrieved from the model calculation.

Another unique feature of our algorithm is that the integral equation for the radiative intensity and the rate equations for the level populations are solved iteratively. One advantage of this approach is that it does not require one to solve a large number of simultaneous equations because the separate layers of the atmosphere are not directly coupled; rather, one solves a separate equation set for each altitude, the number of equations in each set being equal to the number of vibrational levels whose populations are being sought. Secondly, one can relax the requirements on the altitude grid that is assumed, using finer or coarser layering as desired, and set the upper and lower boundaries to accommodate the bands in question. Thirdly, since there is no

requirement to linearize the equations in the unknown number densities, nonlinear terms accounting for stimulated emission and changes in the ground-state number densities (reflecting changes in the vibrational partition function) can be retained.

For all vibrational levels that we are considering, absorption of photons that are emitted by molecules within the atmosphere is an important excitation, or "pumping", mechanism. Absorption of solar photons can be treated separately. For radiative de-excitation in a band we calculate the thermally-averaged Einstein A coefficient from the individual line data on the HITRAN database *(Rothman et al, 1987)*. We assume that all other production and loss processes are properly parameterized by rate constants or other information that can be specified at the beginning. Most of the following discussion therefore deals with the pumping calculation.

The assumptions that underlie the LBL radiative excitation algorithm are that (1) plane-parallel geometry with no horizontal inhomogeneities in temperature, pressure, or number density is a sufficiently accurate description of the atmosphere; (2) the ro-vibrational lines do not overlap; (3) there is complete frequency redistribution within each line so that the emission and absorption lineshapes are the same; and (4) the rotational levels are always in equilibrium with translation, or (otherwise stated) the rotational temperature is always equal to the kinetic temperature.

The only discretization of physical quantities is that imposed by the thickness of the atmospheric layers, which are considered to be homogeneous in all respects. We usually use 150 one-km layers starting at a lower boundary of 40 or 50 km. Layer temperatures are taken to be simple averages of the values at the layer-boundaries; for number densities, the geometric mean is used.

RAD uses an iterative algorithm that operates by the method of successive substitution. That is, some provisional vibrational temperature for the upper radiating state(s) is selected so that emission rates everywhere in the atmosphere can be calculated. Using this, the absorption rate in the band(s) can be found at each observation point, as described below. Then an updated vibrational temperature profile is calculated, and the whole process repeats until convergence criteria are satisfied. The final profile must, of course, be insensitive to the choice of the initial profile.

In Section A we formulate the vibrational population calculation using the simplest example, a two-level system. In Section B we outline the means by which several infrared-active states are coupled, so that a simultaneous determination of their populations is possible.

A. Vibrational Populations in a Two-Level System

In this section we discuss a system with only two populated vibrational levels, coupled by radiative and collisional transitions. If N_1 and N_2 are the populations of the lower and upper vibrational levels (in mol/cm^3), then the steady-state solution is

$$\frac{N_2}{N_1} = \frac{J_{21} + K_{21}}{A_{12} + K_{12}} \tag{1}$$

where J_{21} is the local radiative excitation rate—the absorption rate per molecule—and is the only quantity that is difficult to calculate. A_{12} is the Einstein coefficient for spontaneous emission, K_{12} is the total collisional deactivation rate, and K_{21} is the reverse rate. These quantities all have units of transitions/mol-s. If the upper state is quenched by V-T collisions with nitrogen and oxygen molecules, having a total number density [M], and with oxygen atoms having a density [O], then

$$K_{12} = k_M[M] + k_o[O] \tag{2}$$

where k_M and k_o are the rate constants (in cm^3/mol-s) for the respective reactions. K_{21} is the same, except that the reverse rate constants appear.

Consider the previous discussion in terms of the ground and first excited state of CO_2. (The processes mentioned are, in fact, by far the most important ones affecting the population of the excited state.) N_1 is regarded here as a known quantity, so when all the terms on the right-hand side of Eq.(1) have been calculated, the solution for N_2 is trivial. It is true, however, that for molecules with low-lying excited states like CO_2, the total excited-state population is not negligibly small in comparison to that of the ground state, so N_1 is not truly known. One advantage of the method outlined below is the possibility of correcting N_1 on successive iterations; one accounts for even this small effect while retaining the very simple formulation represented by this equation.

For this simple case, a sufficient condition for LTE between the two levels is that J_{21} and A_{12} be in the same ratio as K_{21} and K_{12}—that is, related by a Boltzmann factor in the kinetic temperature. This will, in fact, occur if the absorbed photons nearly all come from nearby source regions with the same temperature. LTE due to "local pumping" can therefore be common when the lines are very thick. On the other hand, in the absence of strong attenuation over short distances, it is necessary that the collisional transition rates be much greater than the radiative transition rates to maintain LTE. Pumping from remote regions having differing emission rates will disrupt the balance between J_{21} and A_{12}, and if these rates are not negligible in

5

comparison to the collision transfer rates, the imbalance will cause a non-LTE distribution between N_1 and N_2.

1. Radiative Excitation in a Single Band

To calculate the actual absorption in a single line at a given observation point, one needs to know the specific intensity of radiation arriving from all directions, and also the probability of absorption occurring. By definition of the Einstein absorption coefficient, the absorption rate for photons of wavenumber ν is proportional to the product of the Einstein coefficient, the local energy density, and the number density of absorbers. By writing the Einstein B-coefficient in terms of the absorption cross section k_ν (in cm^2/mol) and the energy density in terms of the monochromatic specific intensity of radiation averaged over direction, $\bar{I}_\nu$ (in $photons/s\text{-}cm^2\text{-}sr\text{-}cm^{-1}$), one can show that this monochromatic absorption rate (in $photons/s\text{-}cm^3\text{-}cm^{-1}$) is given by

$$\mathfrak{z}_\nu(s) = 4\pi\rho(s)k_\nu(s)\bar{I}_\nu(s) \tag{3}$$

where ρ is the total number density (in mol/cm^3) of the absorbing and radiating specie. (The position variable (s) used as a parameter, as in $k_\nu(s)$, by implication specifies the values of other relevant parameters, such as temperature, that prevail at that point.) The absorption in the line is then

$$\mathfrak{z}(s) = 4\pi\rho(s)\int_{-\infty}^{\infty}k_\nu(s)\bar{I}_\nu(s)d\nu \tag{4}$$

The total absorption in the band is the sum of these quantities over all transitions (t) comprising the band, and for the simple two-vibrational-level problem it is related to J_{21} by

$$J_{21}(s)N_1(s) = \sum_t \mathfrak{z}^{(t)}(s) \tag{5}$$

2. Radiative Excitation in a Single Line

a. Formulation for $\mathfrak{z}^{(t)}$

For any single line, the absorption cross-section, k_ν, is the product of the transition line-strength S (in $cm^2\text{-}cm^{-1}/mol$) and the normalized Voigt lineshape f_ν (in cm). The linestrength for arbitrary conditions, S(s), can be calculated from the tabulated HITRAN linestrengths $S(T_0)$ *(Rothman et al, 1987)* representing conditions of LTE at standard temperature (T_0=296 K) and pressure (1 atm). The cross-section is

$$k_\nu(s) = f_\nu(s)\, S(s) = f_\nu(s)\, S(T_0) \frac{P_l(s)}{P_l(T_0))} \frac{(1-\gamma(s))}{(1-\gamma(T_0))} \tag{6}$$

P_l is the probability that the lower rovibrational state of the transition in question be populated, and is given in terms of the vibrational and rotational energies, temperatures, statistical weights, and partition functions. As before, the parameter (s) refers to conditions prevailing at an arbitrary location while (T_0) refers to "standard" conditions. γ is defined below. In Eq.(6) it corrects the linestrength for stimulated emission.

To calculate $\bar{I}_\nu(s)$, one takes the formal solution of the equation of transport in an emitting and absorbing medium and integrates over solid angle to account for photons arriving from every possible direction. For an arbitrary line of sight path extending from a reference point s' to the observation point s, the solution for the monochromatic specific intensity at wavenumber ν (in photons/s-cm²-sr-cm⁻¹) is *(Chandrasekhar, 1960)*

$$I_\nu(s) = I_\nu(s')e^{-\tau_\nu(s,s')} + \int_{s'}^{s} R(s'')k_\nu(s'')\rho(s'')e^{-\tau_\nu(s,s'')}\,ds'' \tag{7}$$

where τ_ν is the optical depth, defined by

$$\tau_\nu(s,s') = \int_{s'}^{s} k_\nu(s'')\rho(s'')ds''. \tag{8}$$

R, the source function for spontaneous emission, is

$$R(s) = 2c\nu_0^2 \frac{\gamma(s)}{1-\gamma(s)} \tag{9}$$

where ν_0 is the transition energy (in cm⁻¹), c is the speed of light, and

$$\gamma(s) = \frac{g_1 n_2(s)}{g_2 n_1(s)} \tag{10}$$

represents the upper- to lower-state population ratio, inversely weighted by the respective statistical weights, g_2 and g_1. For LTE conditions, n_2/n_1 is simply a Boltzmann factor and R is identical to the Planck source function. Note that n_1 and n_2 refer to populations of particular rotational states within the respective vibrational levels, and are not to be confused with the total vibrational populations, N_1 and N_2.

With the assumption of plane-parallel geometry, the integral of Eq.(7) over solid angle is quickly resolved into familiar forms with simple interpretations. If there is no solar pumping, the first term becomes a surface integral, representing the (attenuated) radiance contributions from the upper and lower plane boundaries. We assume that the "top" of the atmosphere contributes nothing and that the "bottom" is at LTE. The second term becomes a volume integral accounting for the attenuated radiant intensity from the continuum of source points within the atmosphere. We rewrite the position

7

dependence in terms of the altitude, z, and the zenith angle, θ, and let $\bar{\tau}_\nu$ represent the optical depth on a vertical path from z to z':

$$\bar{\tau}_\nu(z,z') = \tau_\nu(s,s')/\cos\theta = \tau_\nu(s,s')/\mu \tag{11}$$

Then, omitting the boundary term for the moment, and assuming a plane-parallel horizontally homogeneous atmosphere, one gets

$$\bar{I}_\nu(z) = \frac{1}{4\pi}\int I_\nu(z)d\Omega = -\frac{1}{2}\int_1^0 d\mu \int R(z'')\,k_\nu(z'')\,\rho(z'')\exp(-\bar{\tau}_\nu(z,z'')/\mu)\,\frac{dz''}{\mu} \tag{12}$$

The z'' integral actually has two parts—one extending from the observation point to the upper boundary, the other to the lower boundary. Interchanging the order of integration, one finds that the μ-integral is just the function $E_1(\bar{\tau}_\nu(z,z''))$, the exponential integral of order 1. In the end, the contribution of the volume emission to the absorption rate in a single line denoted by (t) at the observation altitude z is, from Eq.(4),

$$\mathfrak{z}^{(t)}(z) = 2\pi\rho(z)\int_{-\infty}^{\infty} k_\nu(z)\left\{\left[\int_{z_u}^{z} R(z'')\rho(z'')k_\nu(z'')E_1(\bar{\tau}_\nu(z,z''))\right]dz'' + \int_{z_l}^{z}(\quad)dz''\right\}d\nu \tag{13a}$$

where z_u and z_l are the altitudes of the upper and lower boundaries, and the second z-integral has the same form as the first. Clearly the wavenumber-dependence of the ν-integrand is strongly influenced by the absorption lineshape at the observation altitude (in $k_\nu(z)$), the emission lineshape at all altitudes (in $k_\nu(z'')$), and the attenuation of the intervening atmosphere.

The lower boundary contribution is derived by substituting the blackbody function R(s') for $I_\nu(s')$ in Eq.(7) and integrating the first term over the lower half-space. This time the μ-integral becomes E_2, the exponential integral of order 2. The "blackbody" contribution at the observation altitude is then

$$\mathfrak{z}^{(t)}(z) = 2\pi\rho(z)R(z_l)\int_{-\infty}^{\infty} k_\nu(z)E_2(\bar{\tau}_\nu(z,z_l))d\nu \tag{13b}$$

Since E_2 drops off very rapidly for arguments greater than unity, the lower boundary contribution to the pumping is negligible whenever the vertical-path optical depth to the boundary is greater than approximately five.

The total pumping in the line in question is the sum of Eqs.(13a) and (13b).

b. Evaluation of $\mathfrak{z}^{(t)}$

At this point we introduce the notation for the atmospheric layers. The layer-

boundaries are labeled by the index, k, in the order of increasing altitude:

$$z_l = z_1 < z_2 < \ldots\ldots z_k \ldots\ldots < z_{kmax} = z_u \tag{14}$$

The layers themselves are referenced by $\bar{z}_k$, where the bar indicates an average over the layer whose lower boundary is z_k. The set of observation points may be identical with this set, $\{\bar{z}_k\}$, but it is usually sufficient to explicitly calculate J_{21} for only a subset of layer-boundary points and interpolate the radiative excitation rates to the remaining points. We label the set of observation points $\{Z_i\}$ by a capital letter and the index i for clarity, and use the index k1(i) to identify the layer-boundary corresponding to the ith observation point, so that

$$Z_i \equiv z_{k1(i)} \tag{15}$$

Consider, then, the two z'' integrals in Eq.(13a). With no approximation, each can be written as a sum of z'' integrals over single layers, z_k to z_{k+1}. Then for each homogeneous layer, the source function $R(z'')$ is replaced by an average value, $R(\bar{z}_k)$, and taken outside the integral. Because of Eq.(8) and the relationship between exponential integrals of different orders, only a perfect differential remains inside the integral. Each term now contains

$$\int_{z_k}^{z_{k+1}} R(z'')\rho(z'')k_\nu(z'')E_1(\bar{\tau}_\nu(Z_i,z''))dz'' \sim R(\bar{z}_k)\left\{E_2(\bar{\tau}_\nu(Z_i,z_{k+1})) - E_2(\bar{\tau}_\nu(Z_i,z_k))\right\} \tag{16}$$

Rewriting the absorption cross-section in terms of the linestrength as in Eq.(6), the two contributions to the pumping—the volume emission and the boundary contribution—become

$$\mathfrak{z}^{(t)}(Z_i) = 2\pi\rho(Z_i)S(Z_i)\int_{-\infty}^{\infty} f_\nu(Z_i)\left\{\sum_{k=1}^{kmax-1} R(\bar{z}_k)T_{\nu k}(Z_i)\right\}d\nu \tag{17a}$$

and

$$\mathfrak{z}^{(t)}(Z_i) = 2\pi\rho(Z_i)S(Z_i)R(z_1)\int_{-\infty}^{\infty} f_\nu(Z_i)T_{\nu o}(Z_i)\,d\nu \tag{17b}$$

where $T_{\nu k}$ is

$$T_{\nu k}(Z_i) = E_2(\bar{\tau}_\nu(Z_i,z_1)) \qquad\qquad k = 0 \tag{18a}$$

$$T_{\nu k}(Z_i) = E_2(\bar{\tau}_\nu(Z_i,z_{k+1})) - E_2(\bar{\tau}_\nu(Z_i,z_k)) \qquad\qquad k = 1,\ldots,k1\text{-}1 \tag{18b}$$

$$T_{\nu k}(Z_i) = E_2(\bar{\tau}_\nu(Z_i,z_k)) - E_2(\tau_\nu(Z_i,z_{k+1})) \qquad\qquad k = k1,\ldots,kmax\text{-}1 \tag{18c}$$

This definition of $T_{\nu k}(Z_i)$, which is positive for all k and i, shows that the uplook sum—that is, the sum over layers above Z_i, with $k \geq k1$—is slightly different from the downlook sum, for layers indexed by $k < k1$. A slight revision of notation for the source function,

$$R_k = R(z_1) \qquad\qquad k = 0 \qquad\qquad (19a)$$

$$R_k = R(\bar{z}_k) \qquad\qquad k = 1,.....,kmax\text{-}1 \qquad\qquad (19b)$$

then allows one to write the radiative excitation rate for a single transition, t, for the ith observation point, Z_i, in terms of a single summation over layers. The lower boundary is now accounted for in the sum as a "layer" with an index of $k = 0$. Adding Eqs.(17a) and (17b), this sum is

$$\jmath^{(t)}(Z_i) = 2\pi\rho(Z_i)S(Z_i) \sum_{k=0}^{kmax-1} R_k \int_{-\infty}^{\infty} f_\nu(Z_i)T_{\nu k}(Z_i)\, d\nu \qquad (20)$$

We emphasize that for all physical quantities on the right hand side except for ρ, a superscript (t) is understood, to distinguish the lines. The desired quantity for the band, for each observation point Z_i, is

$$J_{21}(Z_i)\, N_1(Z_i) = \sum_t \jmath^{(t)}(Z_i) = 2\pi\rho(Z_i)\sum_t S(Z_i) \sum_{k=0}^{kmax-1} R_k \int_{-\infty}^{\infty} f_\nu(Z_i)T_{\nu k}(Z_i)\, d\nu \;(21)$$

3. Solar Pumping

Since the sun can be regarded as an infinitely-distant point source, accounting for solar pumping is straightforward and is carried out separately. Our procedure is to calculate the monochromatic absorption rates, integrate within each line and sum over all lines in a manner analogous to that of Eqs.(3)-(5). To simulate daytime conditions, the results of such a calculation are added to Eq.(21) before it is used in Eq.(1). In calculating the attenuation of solar flux prior to determining the absorption rates, we use a spherical-shell atmosphere.

4. The Iterative Process

To solve for the upper-state vibrational population, $N_2(z)$, at any point z one must know $J_{21}(z)$. But the latter quantity itself clearly depends, through the individual-line source functions $R(z'')$, on the continuum of values of N_2 throughout the volume of integration as implied by Eq.(13a), or at least on a fairly large number of discrete values, through R_k as in Eq.(21). As mentioned earlier, one basic approach is to directly

solve the integral equations that describe this interdependence. That is, one can plug Eq.(13) into Eq.(5) and then Eq.(1). Even though there is a sum over lines, the individual ratios of rovibrational populations, n_2/n_1, that appear in the numerator of R for each term in the sum contain a common factor N_2/N_1 that depends on the altitude z'' but not on the line. This factor determines the emission rate at z'' and represents the most influential, albeit not the only, role that the unknown N_2 plays on the right hand side of the rewritten Eq.(1). If one ignores the stimulated emission factor $(1-\gamma)$ appearing in R and k_ν, and also the possible influence (through the vibrational partition function) of the upper-state population on the lower-state population, this equation becomes a linear integral equation relating the value of the unknown upper-state vibrational population N_2 at a single point z to its values at all other points, z''. By choosing an altitude mesh (with, say, M points), invoking some appropriate quadrature to express the z'' integral as a weighted sum of integrands (evaluated at the M mesh points), and also writing M such equations, each with z chosen to be one of the mesh points, one ends up with a large set of linear equations in N_2 that can be solved by matrix inversion.

The iterative approach is quite different and is much simpler to implement since the different altitudes are <u>not</u> explicitly coupled. Rather, we assume some initial upper-state vibrational population profile and use Eq.(21)—with the provisional emission rates determined by this profile—to evaluate J_{21} at different altitudes. Then Eq.(1) is used, in the simple form given, to separately evaluate N_2 at these altitudes. These values of N_2 amount to a new provisional vibrational population profile, which is used to recalculate the emission rates and then J_{21}. Convergence to a final acceptable profile occurs after a number of repetitions.

We have already mentioned some of the advantages of the iterative approach. The major disadvantage is that if the lines are thick the convergence may be quite slow. We have been unable, except by fortuitous choices of initial provisional vibrational temperature profiles, to reduce substantially the number of iterations required. This is a problem because the effort involved in repeatedly evaluating Eq.(21) can be considerable. For each line, and for a sufficient number of wavenumbers within each line to enable a numerical evaluation of the ν-integral, it is necessary to calculate values of the optical depth, $\bar\tau_\nu$, between each observation point and every layer-boundary, and then in addition to evaluate $E_2(\bar\tau_\nu)$. We typically use 50 observation points, 150 layers, between 8 and 24 values of ν, and as many lines as significantly contribute to the overall radiative excitation in the band. Even with storage of repeatedly used quantities (like the Voigt lineshape), efficient algorithms for other functions, and cutoffs of the sums whenever

severe attenuation or weak emission makes the contributions from certain layers negligible, computer time requirements are severe.

The solution to this difficulty is to modify the iterative process slightly. We calculate the most computation-intensive quantities in detail only on the first iteration, and possibly on one or two subsequent iterations; otherwise we use an approximation that takes, by comparison, negligible time. The most costly part of the calculation is the computation of the optical depths and exponential integrals, required to determine the transmission factors $T_{\nu k}$. Since the lower-state populations may change very little, if at all, from iteration to iteration, the <u>transmission</u> is nearly the same; rather, the principal change from iteration to iteration is in the source function, R_k—in particular in the common ratio N_2/N_1 appearing therein—that determines the <u>emission</u> rates. We rewrite Eq.(21) in a convenient form, defining a transfer function W_{ik}:

$$J_{21}(Z_i) N_1(Z_i) = 2\pi N(Z_i) \sum_{k=0}^{k_u-1} \left\{ \sum_t S(Z_i) R_k \int_{-\infty}^{\infty} f_\nu(Z_i) T_{\nu k}(Z_i) d\nu \right\} = 2\pi N(Z_i) \sum_{k=0}^{k_u-1} W_{ik}. \quad (22)$$

Now let us label the iterations with a superscript (m). The first iteration (m=1) is accomplished using the initial (m=0) guesses for the vibrational populations, $^{(0)}N_2(z)$. The elements $^{(0)}W_{ik}$ are all proportional to $^{(0)}N_2(z_k)/^{(0)}N_1(z_k)$. The new populations $^{(1)}N_2(z_k)$ are found from Eq.(1) using Eq.(22). At this point, rather than recalculate W_{ik} from scratch, we can use the original values and simply "update" them with the new populations. That is, after the mth iteration, J_{21} is recalculated using Eq.(22) with

$$^{(m+1)}W_{ik} = \frac{^{(m)}N_2(z_k)}{^{(m)}N_1(z_k)} \frac{^{(0)}N_1(z_k)}{^{(0)}N_2(z_k)} \,^{(0)}W_{ik} \quad (23)$$

and Eq.(1) is then invoked to redetermine the populations. The cost of doing this is the storage required for the array W_{ik} and the neglect of the <u>changes</u> in N_2 in the nonlinear (stimulated-emission) terms. The benefit is that each iteration after the first consumes approximately one percent of the computation time that would otherwise be required; one can perform hundreds of iterations, if necessary, in the time that would be used to do two or three of the complete iterations. As a rule, to account for possible small effects of the nonlinear terms, we repeat the full calculation one time after the accelerated procedure has converged.

B. Vibrational Populations in a Multi-level System

For cases in which two or more vibrational levels are strongly enough coupled that their vibrational temperatures cannot be determined independently, modifications are

12

necessary but the basic advantages of the iterative procedure—the small size of the equation set and the separate determination of the radiative-excitation contributions in separate bands—are preserved.

The formulation is straightforward. If there are p unknown vibrational populations, $N_1,..., N_p$, there are p steady-state equations of the form

$$\frac{dN_j}{dt} = 0 = \sum_{i \neq j}^{p} \{J_{ji}N_i - A_{ij}N_j + K_{ji}N_i - K_{ij}N_j\} + P_j - L_jN_j \qquad (24)$$

where the J_{ji} and A_{ij} terms represent radiative excitation and loss, analogous to J_{12} and A_{21} in Eq.(1), and the K_{ij} and K_{ji} terms are similar to K_{12} and K_{21} in Eq.(1). P_j and L_j represent all production and loss for state j from and into states other than the p unknown ones. P_j may include a term of the form $J_{jo}N_o$ if N_o represents a fixed (known) vibrational population, such as that of a ground state. It is easy to transform a set of equations like Eq.(24) into a matrix equation,

$$[M][N] = [P] \qquad (25)$$

where [M] is a p by p matrix incorporating all coefficients multiplying the elements of the vector of unknowns, [N]. Evidently the solution vector [N] can be obtained by matrix inversion once the matrix elements and the inhomogeneous vector have been determined.

The iterative procedure for the multilevel case is exactly the same as what was described earlier. All radiative excitation terms, J_{ij}, are (separately) evaluated on the basis of initial estimates of the vibrational populations exactly as outlined in the discussion leading up to Eq.(21). Then the matrix equations, whose other terms are fixed, yield new estimates of the populations, and the process continues as long as necessary. There is no ambiguity about evaluating one pumping rate before another because the equations are simultaneous equations. It is, of course, necessary to have storage for the transfer functions, W, for all the bands.

13

This page intentionally blank.

II. CO$_2$ 15 μm EMISSION

We have incorporated the RAD algorithm in a model for predicting long-wavelength emission from CO$_2$, and used the model to simulate the SPIRE limb radiance data set *(Stair et al, 1985)*. In this section we outline the model, show the detailed results vibrational temperatures, excitation rates, limb radiance) for the conditions of the SPIRE experiment, and discuss the conclusions that we have drawn.

The most important vibrational energy levels of CO$_2$ are shown in Figure 1. Practically all CO$_2$ infrared bands of interest in the terrestrial atmosphere connect states that are included in this diagram. The levels that are important for emission in the 15 μm bands are the low-lying levels having ν_1 (symmetric stretch), ν_2 (bending mode) and $\nu_1\nu_2$ excitations. Collectively these states, which appear in the three leftmost columns of Figure 1, are known as the "bend-stretch manifold". Properties of the most important of these states *(Rothman, 1986)* and the corresponding radiative transitions are listed in Table 1.

To a good approximation, one can regard the small subset of states consisting of 01101, 02201, 10002, 10001, and 03301 as being entirely responsible for long-wavelength emissions from CO$_2$ that are seen in the earthlimb—provided that one recognizes the importance of minor-isotope bands originating in these states in addition to the bands of the principal $^{12}C^{16}O_2$ isotope.

A. Outline of the Model

1. Coupling Scheme

We consider the bend-stretch manifold as an entity in itself. This is justified for the purposes of modeling the 15 μm limb radiance because the mechanisms that couple these states to higher-lying CO$_2$ states or to excited vibrational states of other molecules are too weak to affect the populations of the principal radiating levels to such an extent that the observed radiance would be significantly enhanced if these effects were included. The 01101 level is coupled strongly to ground by thermal and radiative transitions, and we regard these interactions to be sufficient to determine its population. The effect of higher states on 01101 is, in this approximation, negligible. We regard the group of strongly-coupled 2ν_2 states to be in equilibrium with each other at all altitudes, and to be coupled to 01101 by V-T and radiative transitions while remaining unaffected by transitions to and from higher-energy states. The same considerations apply to the coupled 3ν_2 states. Our procedure is to first solve for the vibrational temperature of
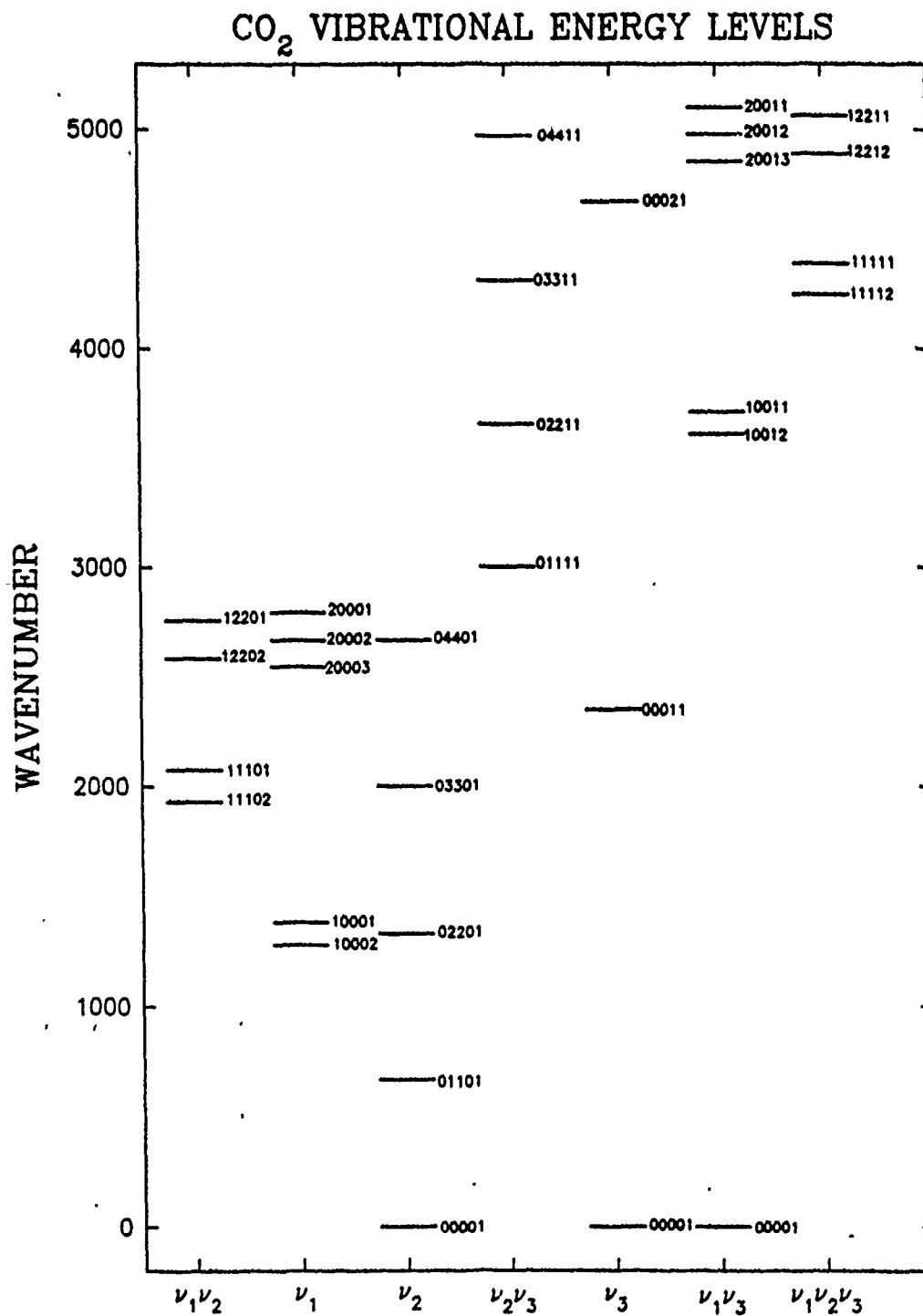
15

CO$_2$ VIBRATIONAL ENERGY LEVELS

Figure 1. Vibrational energy levels of CO$_2$ that are of interest in atmospheric radiance studies.

TABLE 1. Lowest-lying states in the bend-stretch manifold and the most important radiative transitions among them. The level designation is given in the AFGL (Benedict) notation and in the usual spectroscopic notation.

Isotope	Upper —Designation— AFGL	Usual	Level Energy (cm⁻¹)	Lower Level	Transition Energy (cm⁻¹)	Transition Wavelength (μm)	A (s⁻¹)
All	00001	00^00	0.0	—	—	—	—
626	01101	01^10	667.38	00001	667.38	14.98	1.52
626	10002	02^00	1285.41	01101	618.03	16.18	1.17
626	02201	02^20	1335.13	01101	667.75	14.98	3.08
626	10001	10^00	1388.18	01101	720.43	13.88	2.04
626	11102	03^10	1932.47	02201	597.34	16.74	0.51
				10002	647.06	15.45	2.00
626	03301	03^30	2003.25	02201	668.12	14.97	4.65
626	11101	11^10	2076.86	10001	688.68	14.52	2.50
				02201	741.73	13.48	1.18
636	01101	01^10	648.48	00001	648.48	15.42	1.35
636	10002	02^00	1265.83	01101	617.35	16.20	1.36
636	02201	02^20	1297.26	01101	648.79	15.41	2.70
636	10001	10^00	1370.06	01101	721.58	13.86	1.59
636	03301	03^30	1946.35	02201	649.09	15.41	4.05
628	01101	01^10	662.37	00001	662.37	15.10	1.47
627	01101	01^10	643.33	00001	643.33	15.54	1.54

01101 and then, using this as a known quantity, to determine the vibrational temperature of the three $2\nu_2$ states. Then, treating the latter as known, an analogous procedure yields the vibrational temperature of the $3\nu_2$ states. We follow this procedure for each of the four most abundant isotopes of CO_2, although the third step is unnecessary for all but 626 and even the second step is unnecessary for 628 and 627. Thus, the problem is reduced to a sequence of two-level calculations.

The collisional processes are shown in Table 2a, and the corresponding rate constants are listed in Table 2b. A rate constant having the form k_{ij} refers to a transition between an initial state j and a final state i. The ground and first excited states are 1 and 2, while the groups of Fermi-resonance states near 1335 cm^{-1} and 2000 cm^{-1} are collectively referenced as levels 3 and 4, respectively.

The expressions that we use for the V-T interactions have a high-temperature behavior of the Landau-Teller form. The $\sqrt{T}$ dependence in the first term implies a temperature-independent cross-section at low temperatures, but our choice of this form is empirical. For collisions of CO_2 with N_2 and O_2, the constants in these expressions were chosen to provide a fit to the published experimental data *(Allen et al, 1980; Lunt et al, 1985; Taine et al, 1978; Taine and Lepoutre, 1979; Simpson et al, 1977)*. Figures 2 and 3 show these data for the deactivation of $CO_2(01101)$, and our approximations to them. Figure 4 shows the scant data available for the V-T deactivation of $CO_2(02201)$ by N_2, and our parameterization.

In view of the great efficiency with which oxygen atoms excite the CO_2 bending mode, it is impossible to construct a model for the bend-stretch states without considering CO_2-O collisions carefully. There are no data whatsoever in the temperature range of interest to us, however. Therefore we ran our model with one of the constants in the expression for $k_{12}(O)$—the coefficient of the $\sqrt{T}$ term, which dominates the temperature-dependence of the rate constant—as a free parameter. That is, we used

$$k_{12}(O) = A_o \times 10^{-13}\sqrt{T} + 2.32 \times 10^{-9}\exp(-76.75/T^{0.33}) \qquad (26)$$

to describe the CO_2-O collisions, and varied A_o to obtain a good fit with the SPIRE data. In this way we determined that the oxygen-atom rate constant is much larger, for the range of temperatures found in the lower thermosphere, than values appearing in the literature *(Gordiets et al, 1982; Dickinson, 1984; Lopez-Puertas et al, 1986a)*, and also somewhat larger than values previously estimated on the basis of a preliminary analysis of the same SPIRE data set *(Sharma and Nadile, 1981; Kumer and James, 1982)*. This point is discussed in more detail in Section B.2.c. The value for A_o that

TABLE 2 a. Reactions included in the $CO_2(\nu_2)$ model.

Reaction			Type	Rate Constant	Exo-thermicity (cm^{-1})
$CO_2(01101) + M$	$\rightleftharpoons$	$CO_2(00001) + M$	V-T	$k_{12}(M)$	667.38
$CO_2(02201) + M$	$\rightleftharpoons$	$CO_2(01101) + M$	V-T	$k_{23}(M)$	667.75
$CO_2(03301) + M$	$\rightleftharpoons$	$CO_2(02201) + M$	V-T	$k_{34}(M)$	668.12
$CO_2(2\nu_2) + CO_2(00001)$	$\rightleftharpoons$	$CO_2(01101) + CO_2(01101)$	V-V	$k_v(CO_2)$	.37
$CO_2(3\nu_2) + CO_2(00001)$	$\rightleftharpoons$	$CO_2(02201) + CO_2(01101)$	V-V	$\overline{k}_v(CO_2)$	.73

TABLE 2 b. Rate constants describing the reactions, in the forward direction. Units are cm^3/mol-s.

Symbol	Parameterization	Value at 300 K $(cm^3/mol$-s)
$k_{12}(N_2)$	$7.0 \times 10^{-17}\sqrt{T} + 6.7 \times 10^{-10}\exp(-83.8/T^{0.33})$	3.7×10^{-15}
$k_{12}(O_2)$	$7.0 \times 10^{-17}\sqrt{T} + 1.0 \times 10^{-9}\exp(-83.8/T^{0.33})$	4.9×10^{-15}
$k_{12}(O) \equiv k_o$	$3.5 \times 10^{-13}\sqrt{T} + 2.32 \times 10^{-9}\exp(-76.75/T^{0.33})$	6.1×10^{-12}
$k_{23}(N_2)$	$3 \times k_{12}(N_2)$	1.1×10^{-14}
$k_{23}(O_2)$	$3 \times k_{12}(O_2)$	1.5×10^{-14}
$k_{23}(O)$	$k_{12}(O)$	6.1×10^{-12}
$k_{34}(N_2)$	$1.5 \times k_{23}(N_2)$	1.6×10^{-14}
$k_{34}(O_2)$	$1.5 \times k_{23}(O_2)$	2.2×10^{-14}
$k_{34}(O)$	$k_{12}(O)$	6.1×10^{-12}
$k_v(CO_2)$	1.2×10^{-11}	1.2×10^{-11}
$\overline{k}_v(CO_2)$	1.2×10^{-11}	1.2×10^{-11}

Figure 2. Experimental values for the rate constant describing the V-T deactivation of $CO_2(01101)$ by collisions with N_2, with typical experimental errors indicated. The parameterization given in Table 2 is plotted as the solid line.
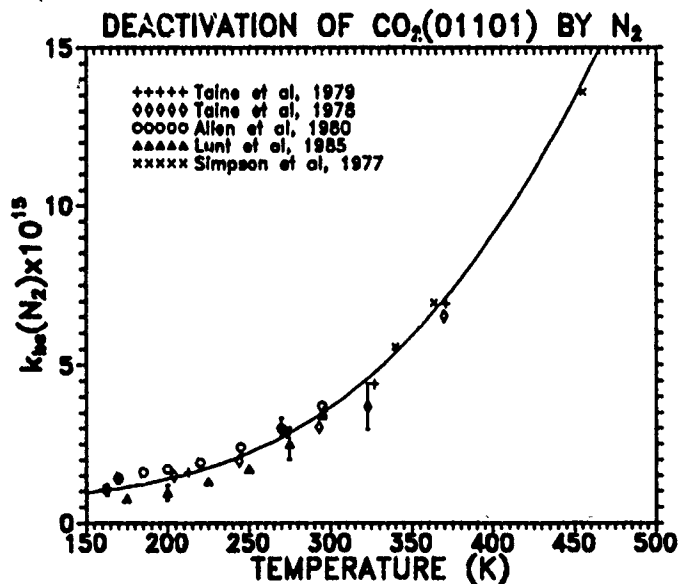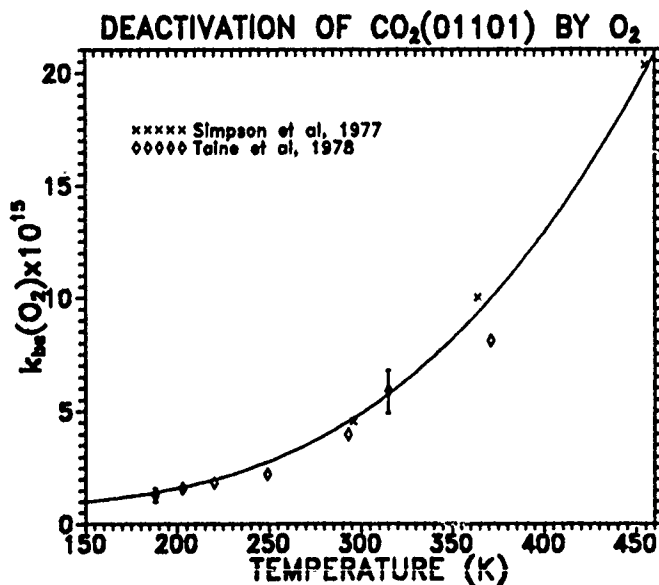

Figure 3. Experimental values for the rate constant describing the V-T deactivation of $CO_2(01101)$ by collisions with O_2, with typical experimental errors indicated. The parameterization given in Table 2 is plotted as the solid line.

DEACTIVATION OF $CO_2(2\nu_2)$ BY N_2

ooooo Taine et al, 1979

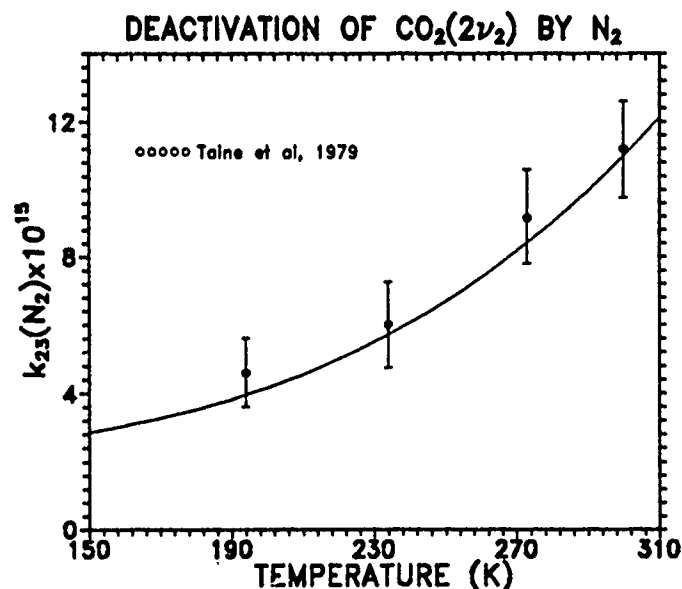y-axis: $k_{23}(N_2) \times 10^{15}$

x-axis: TEMPERATURE (K)

Figure 4. Experimental values for the rate constant describing the V-T deactivation of $CO_2(02201)$ by collisions with N_2. The parameterization given in Table 2 is plotted as the solid line.

appears in Table 2b, 3.5, is thus the optimal value according to our model and the SPIRE data.

2. Model Atmosphere for the SPIRE Simulation

a. [O]

Oxygen atom concentrations in the lower thermosphere are quite variable. We have used MSIS-86 *(Hedin, 1987)* for our [O] profile above 85 km. For altitudes below the MSIS lower boundary, we use an [O] profile from the model of *Keneshea et al (1979)* for the 60 to 85 km region, scaling it to match MSIS at 85 km. The model oxygen atom density is given in Figure 5 for altitudes above 80 km.

b. [CO$_2$]

To establish a CO_2 profile suitable for the conditions we were simulating, we examined the published measurements of CO_2 in the 50-150 km range. All the experiments were conducted at midlatitudes—between 30° and 40°—but at different times of day
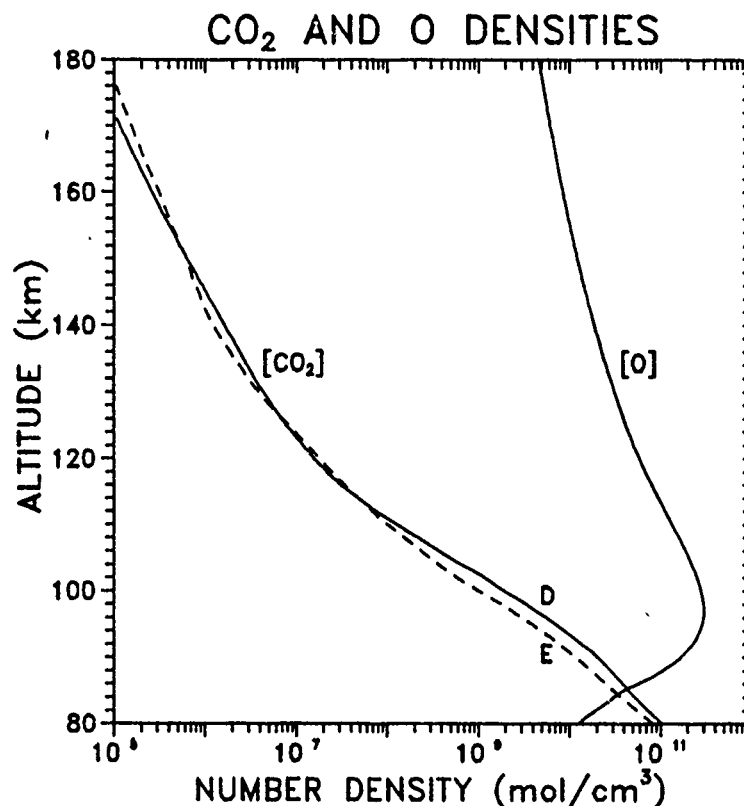
CO₂ AND O DENSITIES

Figure 5. Number density profiles for O and CO_2. The two CO_2 curves correspond to the "high" and "low" mixing ratio profiles, Models D and E respectively, that are shown in Figures 6a and 6b.

and year with different types of instruments. There is considerable variability in the reported number densities, but we assumed that the mixing ratio is less dependent on local conditions than the number density itself, and we calculated it for all experiments in which CO_2 and total number density were measured simultaneously.

Results from rocket experiments conducted in the 1970s, including those of the Aladdin program *(Trinks and Fricke, 1978; Trinks et al, 1978)*, the S75 and B2 experiments *(Offermann et al, 1981)*, and the SN5 payload *(Offermann and Grossmann, 1978)*, treated this way, are shown in Figure 6a. All are consistent with complete mixing at 330 ± 40 ppmv up to at least 90 km, followed by a rapid dropoff to about 83 ppmv at 110 km and to about 40 ppmv at 120 km, with a more gradual decline thereafter.

We also considered results of more recent solar-occultation experiments: the grille spectrometer experiment aboard Spacelab 1 *(Vercheval et al, 1986; Girard et al, 1988)* and the ATMOS experiment *(Beer et al, 1988)*. In the case of the grille spectrometer,
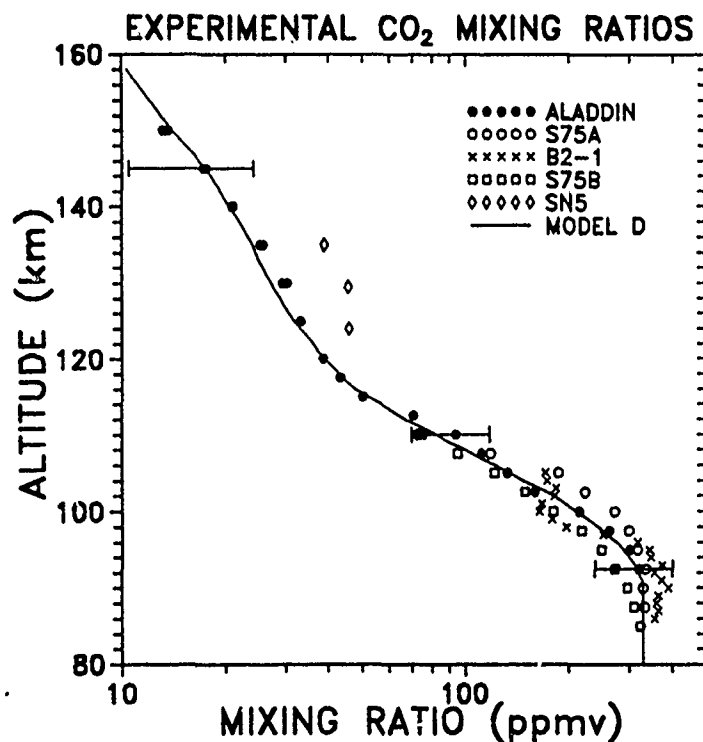
22

EXPERIMENTAL CO$_2$ MIXING RATIOS

Figure 6a. CO$_2$ mixing ratios from rocket experiments reported in the literature. Error bars show typical uncertainties. Also shown is the "high" mixing ratio profile, Model D, that we use to approximate these data.

mixing ratios are directly available in the results from one occultation, event 13 *(Vercheval et al, 1986)*. The results of three others are reported separately *(Girard et al, 1988)* as CO$_2$ number densities. To make use of the latter, we divided them by total number densities that were determined from MSIS-86 using input parameters that were appropriate for each event. These results are shown in Figure 6b.

The data shown in Figures 6a and 6b are inconsistent in the altitude range 80-110 km. That is, the experiments reported in Figure 6b (especially the ATMOS experiment, which suggests incomplete mixing as low as 80 km) show significantly lower mixing ratios than those reported in Figure 6a. Because of this disparity, we modeled the data with two different smoothed curves. Model D, the "high" profile, is shown as the solid line in Figure 6a; Model E, the "low" profile, is the solid line in Figure 6b. We ran our model using both profiles. The two profiles are also given in Figure 5.

c. [N$_2$], [O$_2$], and Total Density

Above 85 km, we took the major atmospheric constituents' densities from MSIS. We needed the total density to calculate [CO$_2$] from the mixing ratio, so we summed all the
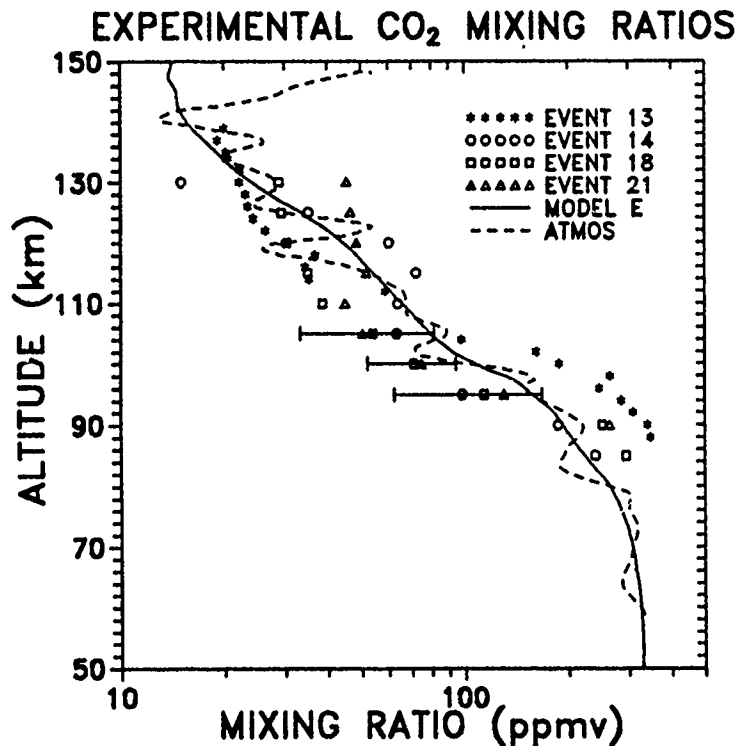
EXPERIMENTAL CO₂ MIXING RATIOS

Figure 6b. CO_2 mixing ratios from satellite experiments reported in the literature. Error bars show typical uncertainties. Also shown is the "low" mixing ratio profile, Model E, that we use to approximate these data.

densities reported in the MSIS output. Below 80 km, we used the FASCODE midwinter-subarctic total density *(Anderson et al, 1986)*, together with standard mixing ratios for the two major constituents. Since the two models have a small difference in the densities at 85 km, we interpolated smooth curves between them in the 80-85 km region.

d. Temperature

The kinetic temperature profile is from MSIS-86 above 87 km, using input conditions appropriate to SPIRE, and the FASCODE midwinter-subarctic atmosphere below 82 km. Interpolation was used between these altitudes. For the date of the experiment, 28 Sept. 1977, the model mesopause temperature is about 178 K, which is about 10 K warmer than the 65°N mean September mesopause in CIRA-86 *(Barnett and Corney, 1987)* but very slightly cooler than the mean October mesopause. The model temperature profile is shown below, superposed on all plots giving vibrational temperature results.

B. Results for the SPIRE Simulation

1. Vibrational Temperatures and Excitation Rates

Figures 7a and 7b show the vibrational temperatures of the 01101 state for the four CO_2 isotopes that we considered, for the "high" and "low" CO_2 profiles, Models D and E. For comparison, the kinetic temperature profile is also shown. The vibrational temperature of the principal 626 isotope is essentially the same as the kinetic temperature up to about 75 km. Beyond this altitude it drops slightly below the kinetic temperature until, at the mesopause, there is a difference of about 4 K. Its minimum occurs a few kilometers above the mesopause and is followed by a rapid increase with

CO$_2$ VIBRATIONAL TEMPERATURES

Figure 7a. Vibrational temperature profiles for the lowest excited CO_2 vibrational state, 01101, for the major isotope and the three most significant minor isotopes. The kinetic temperature, T, is also shown for purposes of comparison. Model D was used for the CO_2 profile.
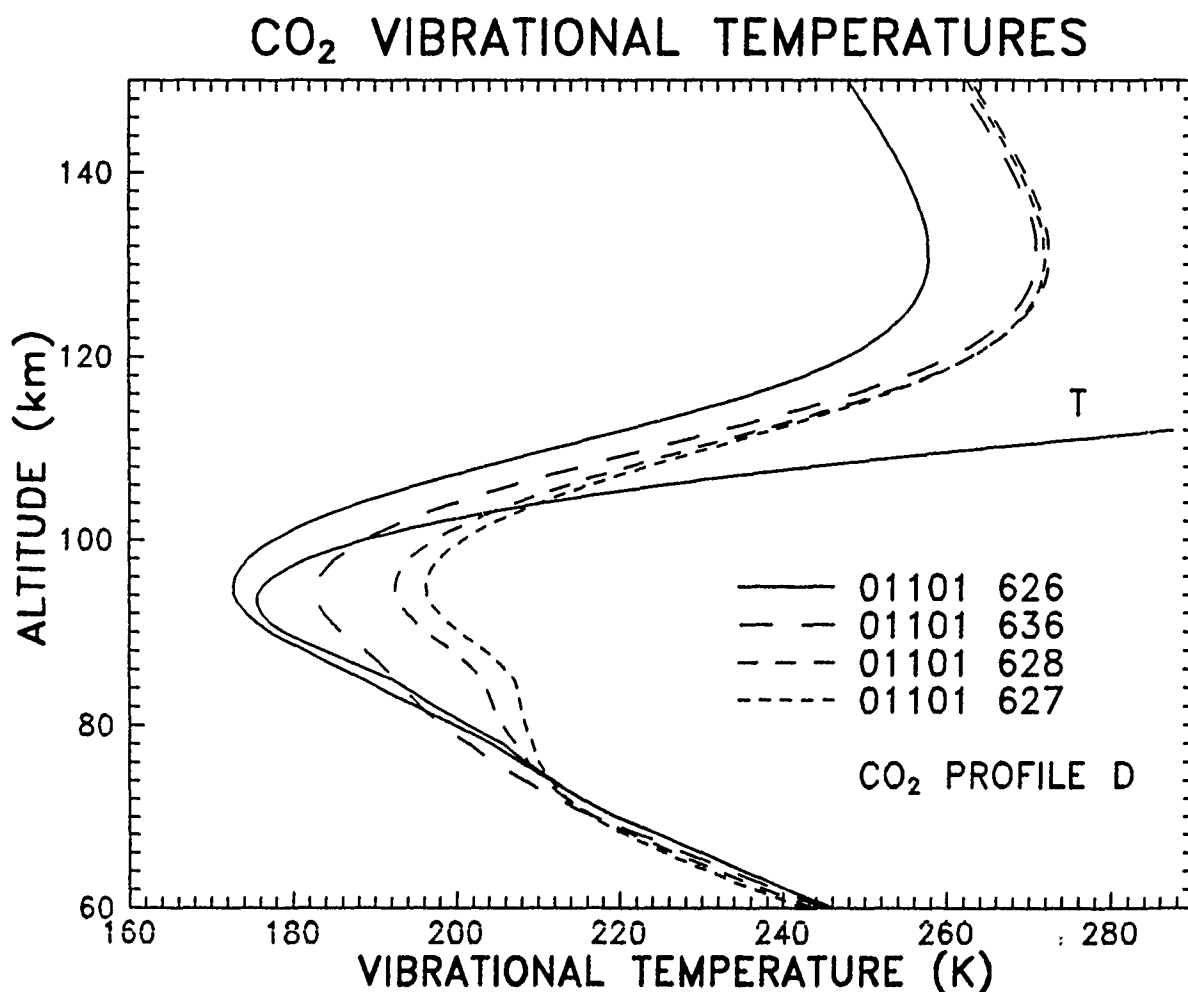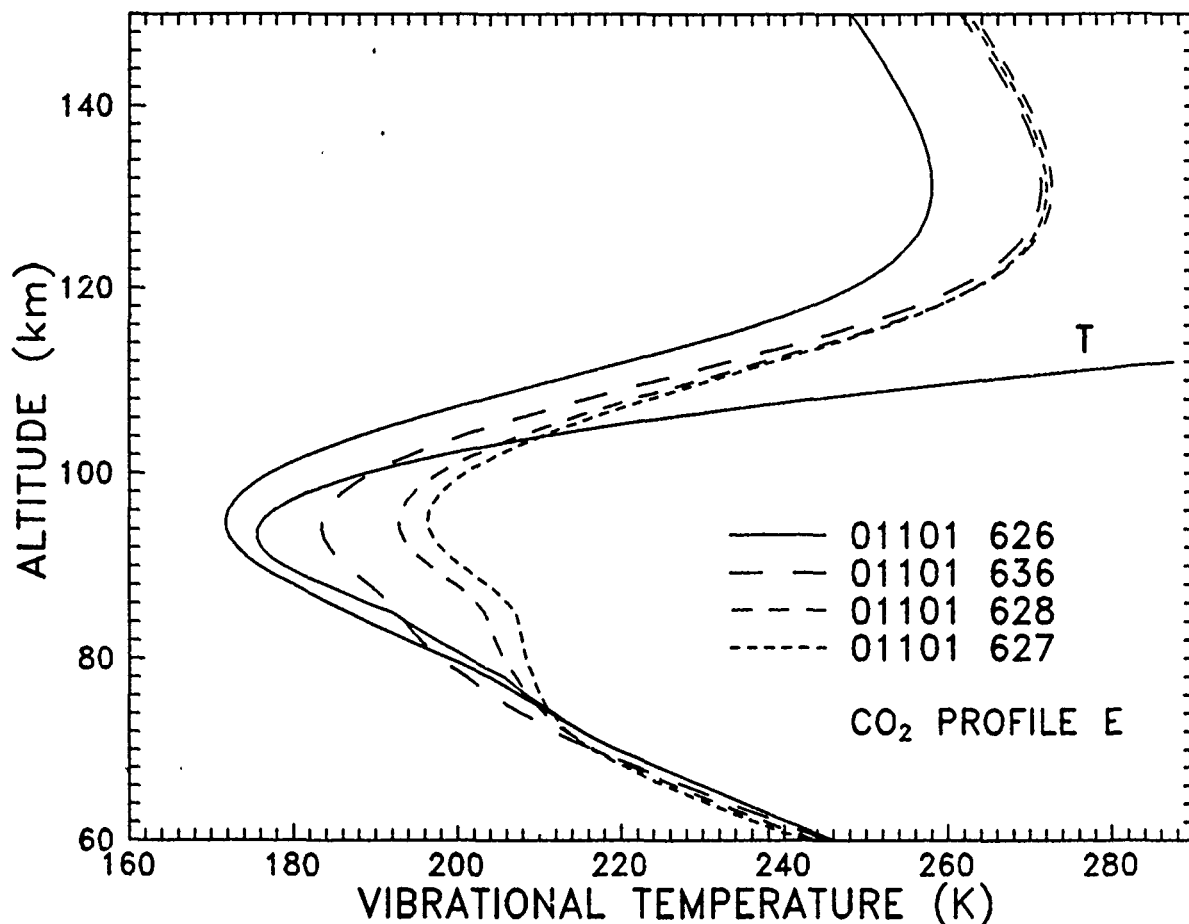
25

CO₂ VIBRATIONAL TEMPERATURES

Figure 7b. Vibrational temperature profiles for the lowest excited CO_2 vibrational state, 01101, for the major isotope and the three most significant minor isotopes. The kinetic temperature, T, is also shown for purposes of comparison. Model E was used for the CO_2 profile.

altitude to a maximum at about 130 km and then a slower drop-off continuing at least up to 200 km. The minor-isotope 01101 vibrational temperature profiles have similar patterns. The main differences are that (1) they have small but noticeable (negative) deviations from the kinetic temperature at and above the stratopause, and (2) they are substantially above the kinetic temperature in the mesopause region. The less abundant isotopes usually have larger deviations from the kinetic temperature.

There is very little difference in the vibrational temperature profiles derived for models D and E, despite the large differences in [CO₂] in the 80-110 km region. The 626 vibrational temperatures differ by no more than 1 K at any altitude, and the minor-isotope differences are even less.

The relative importance of the different excitation and deexcitation mechanisms—radiative processes, V-T processes involving N_2 and O_2, and V-T processes involving O—is given in Figures 8-10. Figure 8 shows the fractional excitation rates for 01101 for the 626 isotope and emphasizes the fact that each excitation mechanism is dominant, or at least the most important process, in a certain altitude range. Figures 9a-9c give the absolute excitation rates for the 626, 636, and 628 isotopes, and Figures 10a-10c give the deexcitation rates.
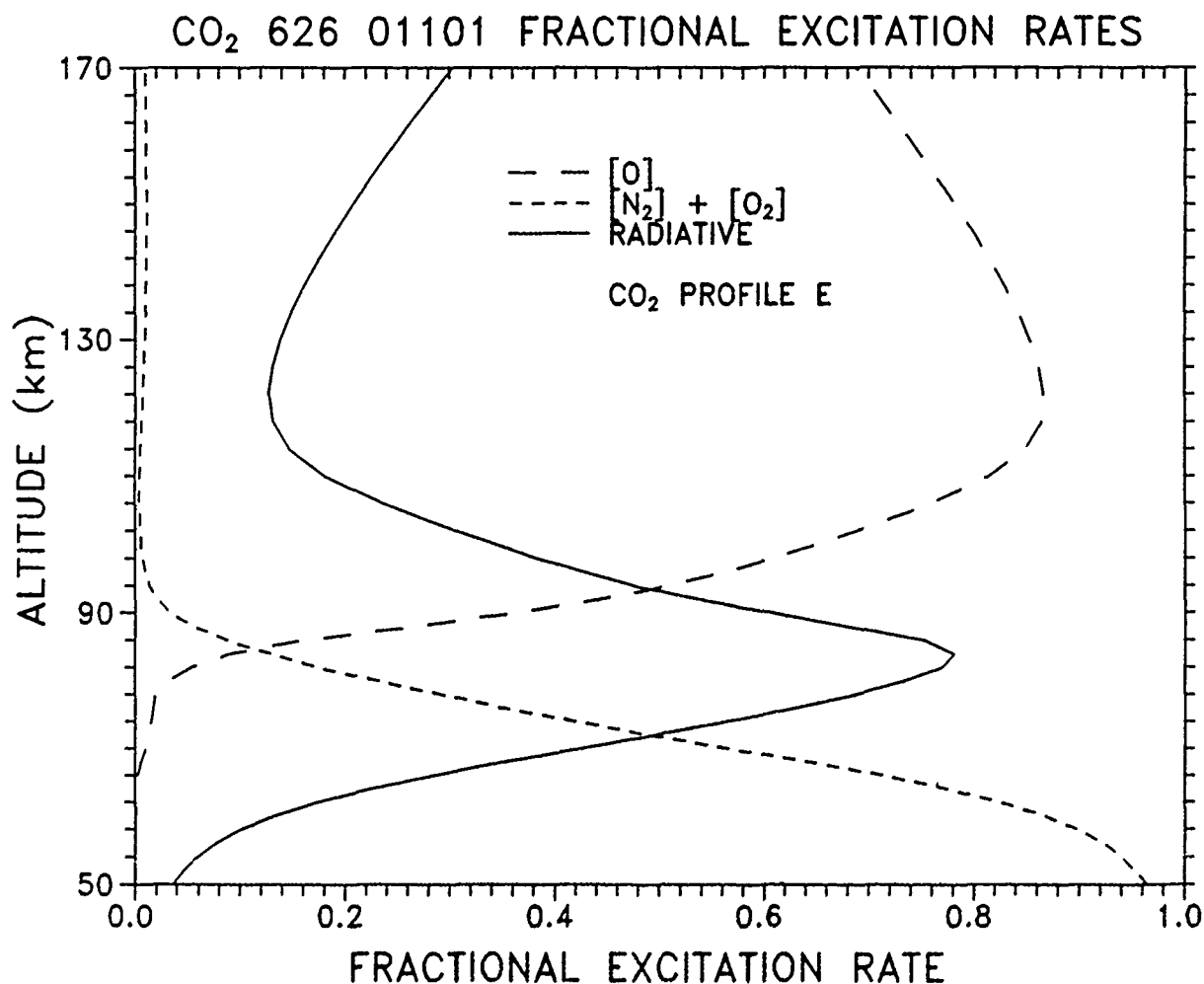
Figure 8. Excitation rates for the 626 01101 state, normalized to unity to emphasize their relative importance over a wide range of altitudes.

CO$_2$ 626 01101 EXCITATION RATES
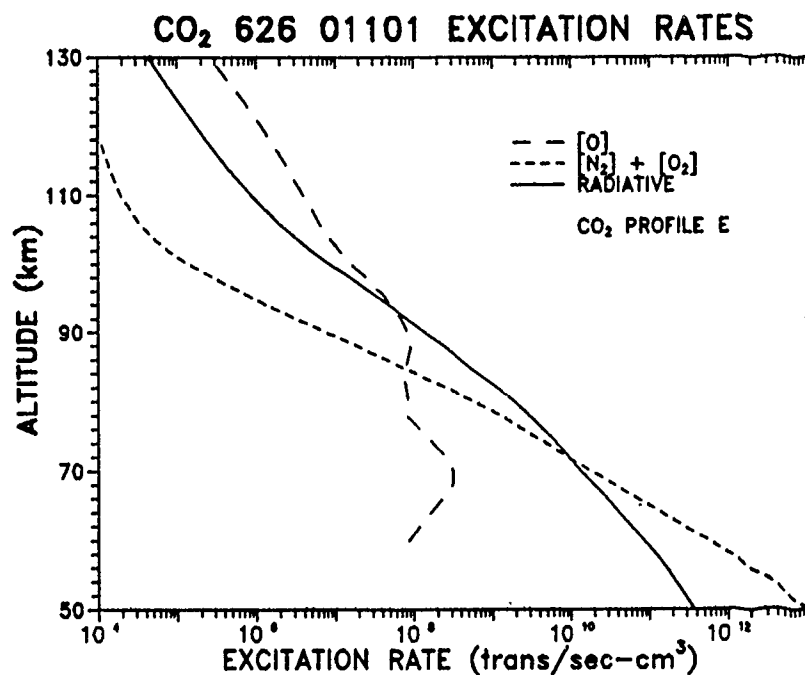
Figure 9a. Absolute excitation rates for the 626 01101 state due to three separate processes.

CO$_2$ 636 01101 EXCITATION RATES
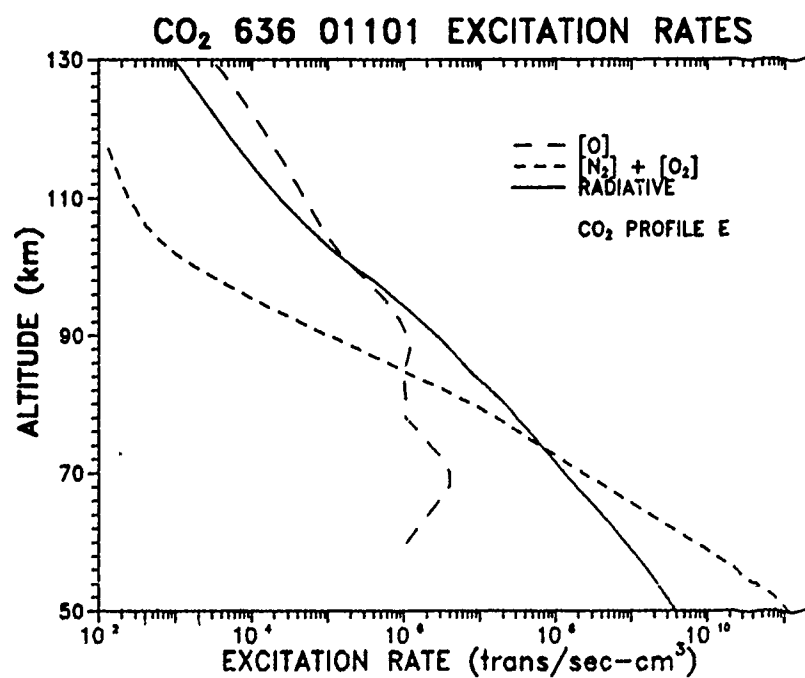
Figure 9b. Absolute excitation rates for the 636 01101 state due to three separate processes.

28

CO₂ 628 01101 EXCITATION RATES
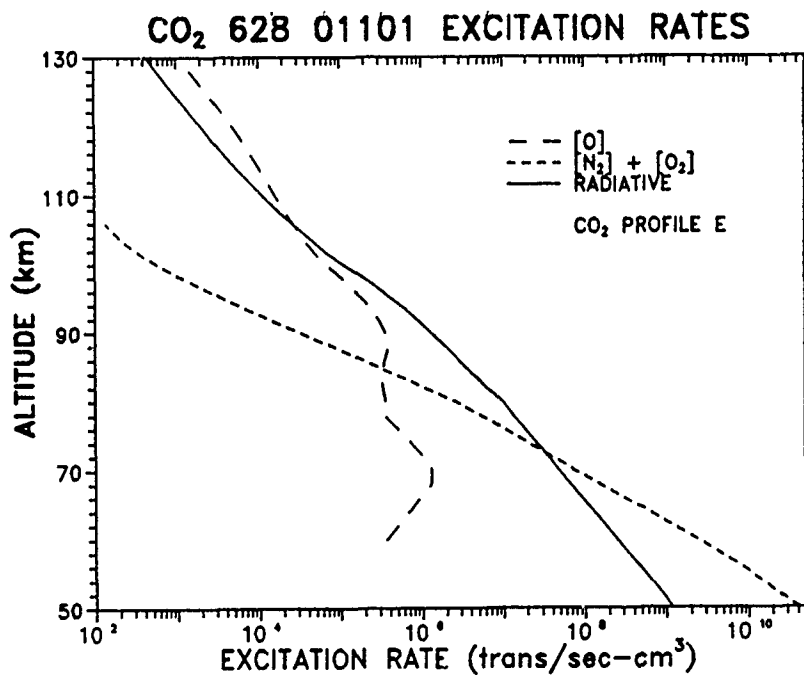
Figure 9c. Absolute excitation rates for the 628 01101 state due to three separate processes.

CO₂ 626 01101 DE-EXCITATION RATES
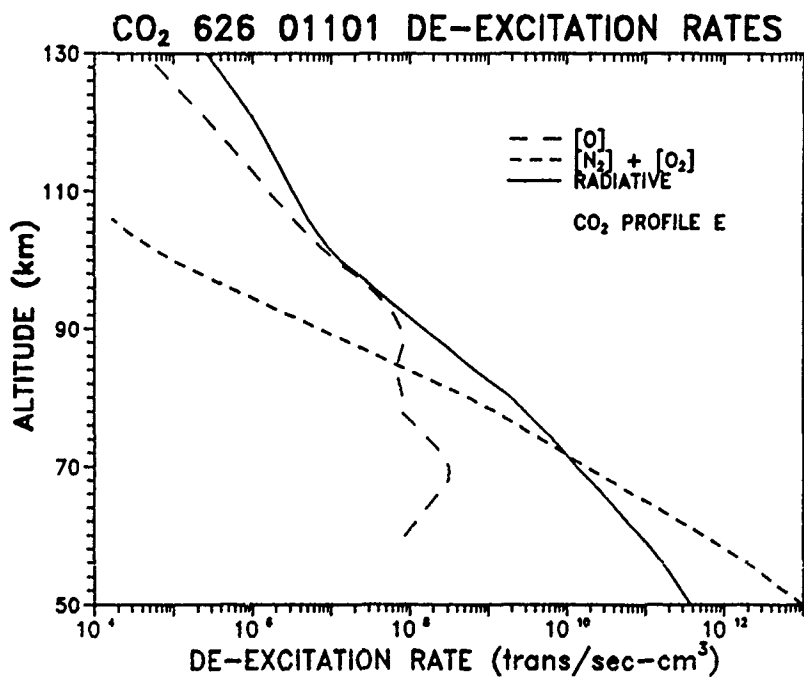
Figure 10a. Absolute deexcitation rates for the 626 01101 state due to three separate processes.

CO₂ 636 01101 DE-EXCITATION RATES

Figure 10b. Absolute deexcitation rates for the 636 01101 state due to three separate processes.

CO₂ 628 01101 DE-EXCITATION RATES

Figure 10c. Absolute deexcitation rates for the 628 01101 state due to three separate processes.

30

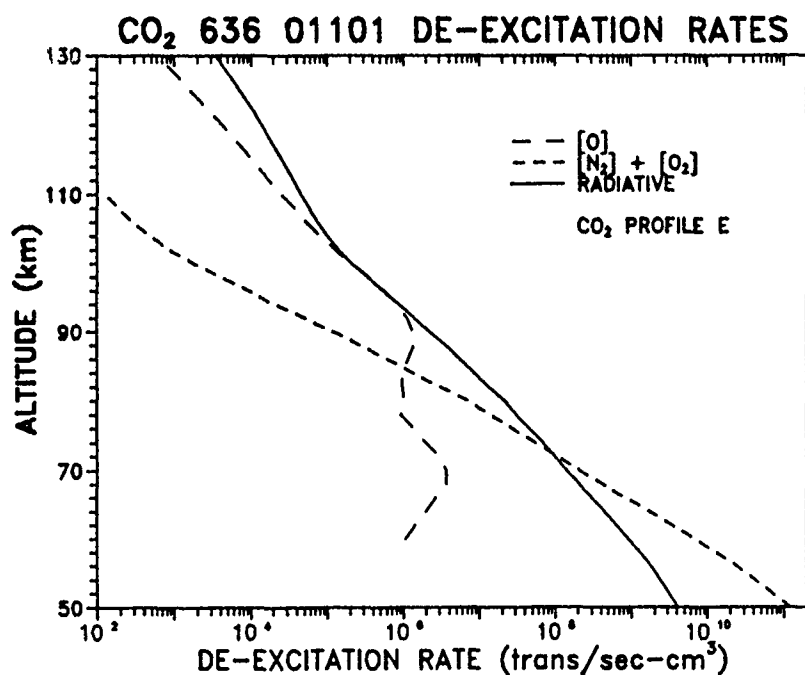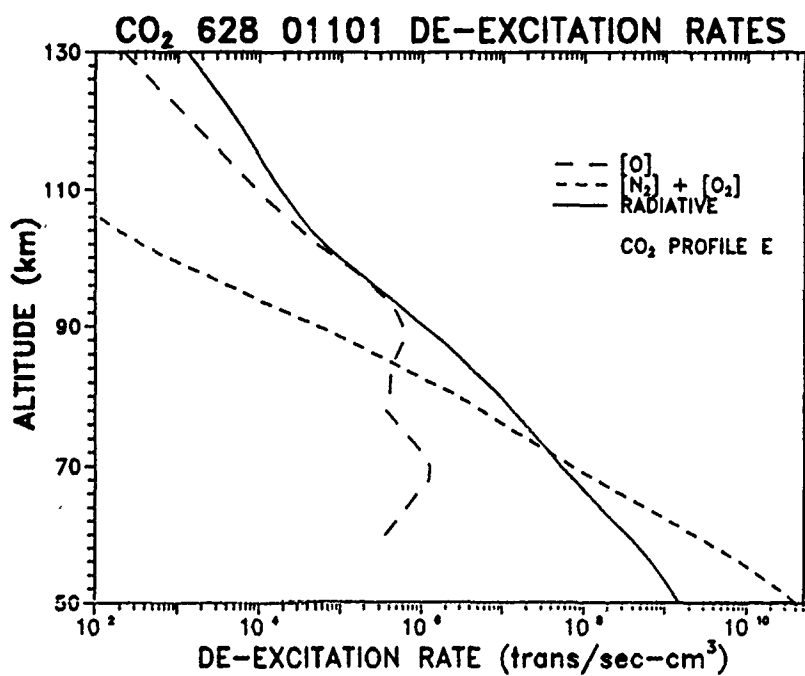Below about 72 km the $\dot{N}_2/O_2$ process is the most important for the major isotope. Standing alone, this process would produce a thermal distribution by definition, so whatever deviations from LTE there may be can only result from a local imbalance in the rates of emission and absorption of radiation. The deviations from LTE for 01101 are small because the collisional transition rates are so much higher than the radiative transition rates that even large differences in emission and absorption, if they existed, would be masked. However it is also true that radiative emission and absorption nearly balance each other, having relative differences of 0.005 or less up to 70 km. It makes sense that these rates balance each other, because at these altitudes attenuation of radiation is severe and the average mean free path of photons in the band is small compared to the distances over which there are substantial temperature differences. Therefore the intensity of radiation that is available to be absorbed at any location (and hence the absorption rate per molecule) is determined primarily by the emission rate in local regions which are at nearly the same temperature. Such imbalance as does exist is the result of transmission in the wings of the strong lines and in the centers of the weakest lines, and it results in net transport of energy from warmer regions where emission rates are higher to cooler regions where they are lower (or, in the limiting case, to space). It is very important to note, however, that even though the difference is small in relative terms, it is large enough in absolute terms to represent a significant loss of energy, especially from the warmer regions, and thereby constitute a cooling mechanism for the stratopause region. That is, the difference between the emission and absorption rates is small compared to the rates themselves, and so small compared to the total transition rates that the vibrational state in question is very close to being in LTE; nevertheless it still has to be compensated by a difference in the collisional excitation and deexcitation rates, and it thereby constitutes a drain on the thermal reservoir that turns out to be significant to the energy balance of the atmosphere.

In the intermediate region depicted in Figure 8, the 01101 excitation is dominated by the absorption of radiation. In this altitude range, which includes the mesopause, thermal processes proceed more slowly due to low temperatures and fewer collision partners, so radiative absorption is relatively more important. The major-isotope vibrational temperature is lower than the kinetic temperature because in the lower part of this region the atmosphere is still quite opaque while in the upper part it is not. As a result, many of the photons emitted in the warmer and more dense region below, potentially a rich source of excitation, never reach the mesopause. Meanwhile, photons emitted at the mesopause escape more easily into the rarified thermosphere and to space. As at lower altitudes, the net effect is that the emission rate exceeds the

absorption rate, but here the difference is great enough in comparison to V-T rates to depress the vibrational temperature more substantially. The absolute difference in the transition rates is less than at the stratopause due to the much lower number densities, however, so the cooling rate is less.

In the third region of Figure 8, above 100 km, O-atom collisions dominate the total excitation of 01101. This occurs because of the rapid rise with altitude in both the O-atom mixing ratio and the kinetic temperature, and it results in the increase of the 01101 vibrational temperature in the 100-130 km region.

The differences between the 01101 vibrational temperature profiles of the major and minor isotopes can be entirely accounted for by the differences in the attenuation of radiation. For the minor isotopes, the deviations from LTE in the lower mesosphere result from the freer migration of photons away from this relatively warm region. The most striking feature of the minor-isotope vibrational-temperature profiles, the elevated temperatures at the mesopause, also result from the larger mean free paths for upwelling photons. The net loss of photons from the warm lower mesosphere leads to a net gain in the mesopause region, and the less radiation trapping there is the larger is the net gain. In contrast to the major isotope, loss to higher altitudes is more than overcome by the absorption of upwelling radiation. The vibrational temperature is therefore higher than the kinetic temperature and there is net heating.

Comparing Figures 9a, 9b, and 9c, one sees that the main difference is that for the minor isotopes, radiative excitation is relatively more important due to the lesser opacity of the mesosphere. For example, for the 628 isotope radiative pumping is the strongest excitation mechanism between 72 and 108 km, and is at least comparable to the O-atom excitation throughout the lower thermosphere.

In Figures 11a and 11b we give the vibrational temperatures of some higher-lying states and, for comparison, the kinetic temperature and the 626 01101 vibrational temperature. Again, there is very little difference in the results for the high and low CO_2 profiles. As with the minor-isotope fundamentals, the differences in these profiles are largely attributable to differences in attenuation of radiation through the mesosphere. The excitation and deexcitation rates of the 02201 level, shown in Figures 12 and 13, are similar to those of Figures 9 and 10. However the radiative component is more prominent and deexcitation due to intermolecular V-V transfer (labeled "CO_2" in the figure) is a significant process.

Although the vibrational temperatures are very insensitive to the CO_2 concentrations at the mesopause and above, they are very strongly influenced by other properties

32

CO₂ VIBRATIONAL TEMPERATURES

Figure 11a. Vibrational temperature profiles for the second excited CO_2 vibrational state, 02201, for the 626 and 636 isotopes, and also the 626 03301 vibrational temperature. The 626 01101 vibrational temperature and the kinetic temperature are shown for comparison. Model D was used for the CO_2 profile.

of the atmosphere. For example, the 626 01101 vibrational temperature at the mesopause is mainly determined by the kinetic temperature there (even though radiative processes dominate; the photon mean free path is relatively small). Even for conditions typical of the summer polar region, where the mesopause temperature may be as low as 130 K, the vibrational temperature is only a few degrees different from the kinetic—although it is warmer rather than colder. The minor-isotope mesopause vibrational temperatures and those of the higher-lying states are also influenced by the stratopause kinetic temperatures; differences of 10 K near 50 km will alter these profiles by a degree or more, other factors being equal. Finally, the O-atom concentration has a very significant effect on the vibrational temperatures above the mesopause.
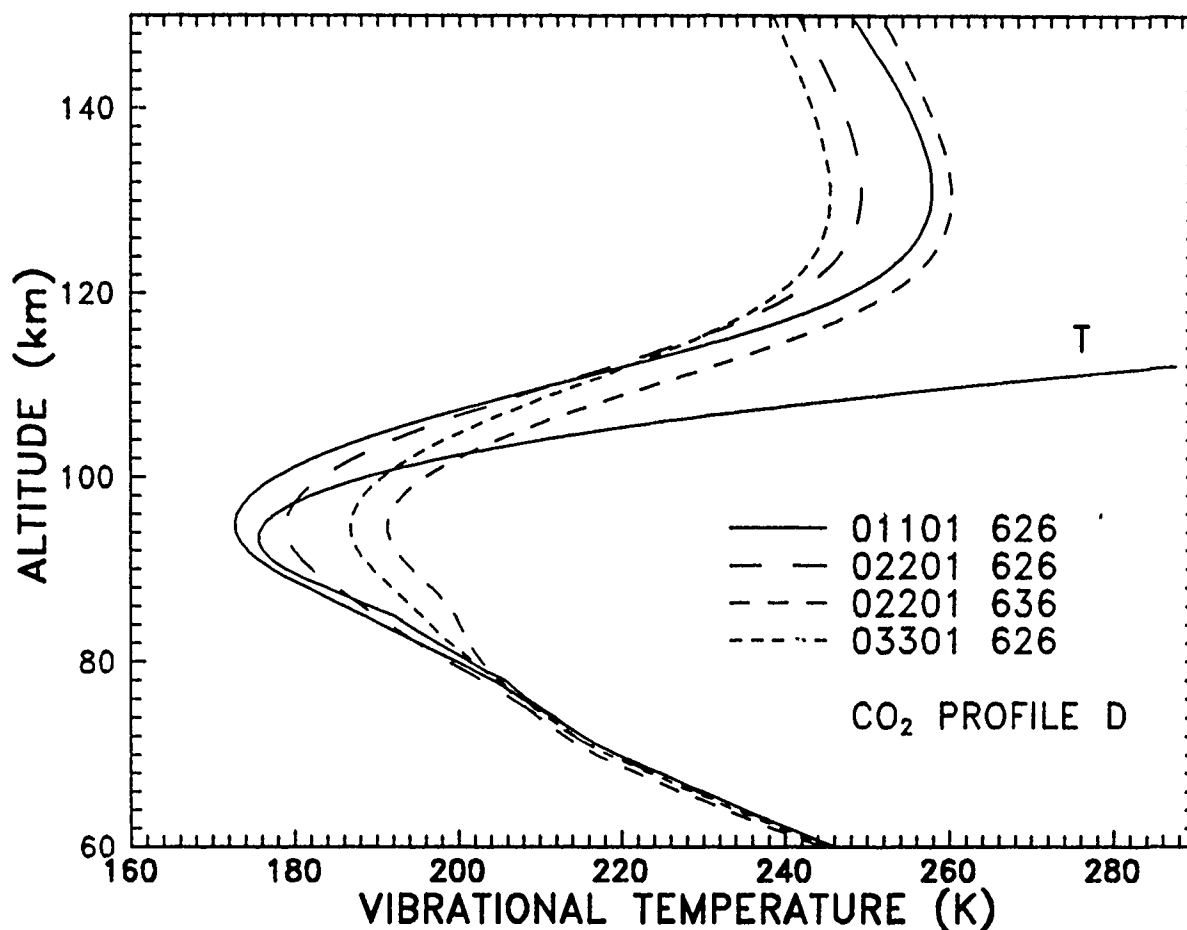
CO₂ VIBRATIONAL TEMPERATURES
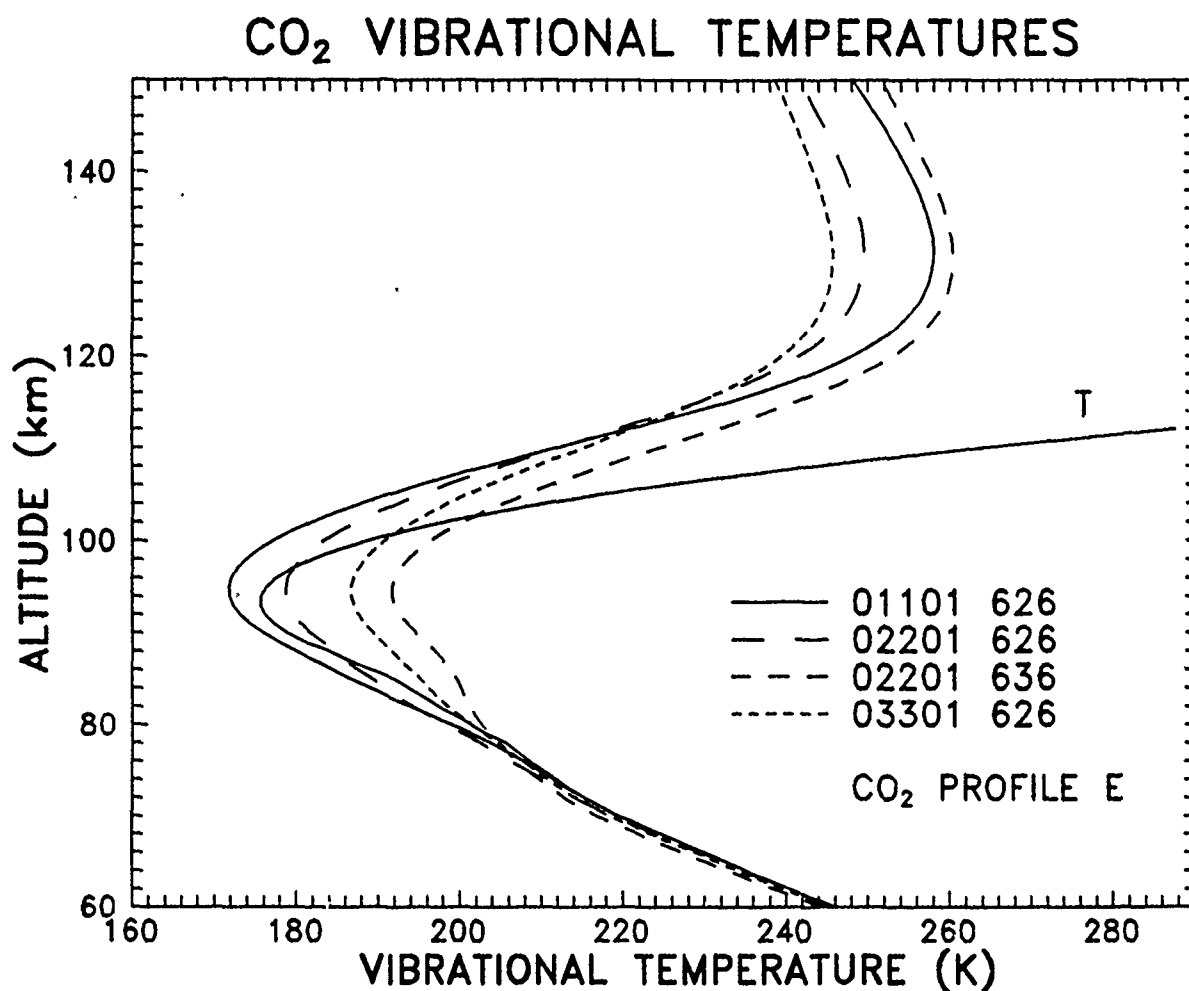
Figure 11b. Vibrational temperature profiles for the second excited CO_2 vibrational state, 02201, for the 626 and 636 isotopes, and also the 626 03301 vibrational temperature. The 626 01101 vibrational temperature and the kinetic temperature are shown for comparison. Model E was used for the CO_2 profile.

A closer look at the radiative excitation at different observation points can be instructive. Figure 14 is a plot of the relative contributions, from different layers in the model, to the radiative excitation in the 626 00001-01101 band at four observation points. For lower altitudes, such as the 70-km observation point, virtually all the pumping comes from the two adjacent layers. Even at 90 km the opacity of the atmosphere restricts the contributions to a few nearby layers. For the higher observation points shown, however, significant contributions come from much lower altitudes, altitudes that are well into regions generally regarded as completely opaque. The explanation for this curious result lies in the altitude dependence of the emission and absorption lineshape. Low-altitude emission from the Voigt wings of the stronger

34

CO$_2$ 626 02201 EXCITATION RATES

Figure 12. Absolute excitation rates for the 626 02201 state due to four separate processes.

CO$_2$ 626 02201 DE-EXCITATION RATES

Figure 13. Absolute deexcitation rates for the 626 02201 state due to four separate processes.

lines is unhindered in its passage through the mesosphere because the pressure and temperature are lower, resulting in narrower absorption li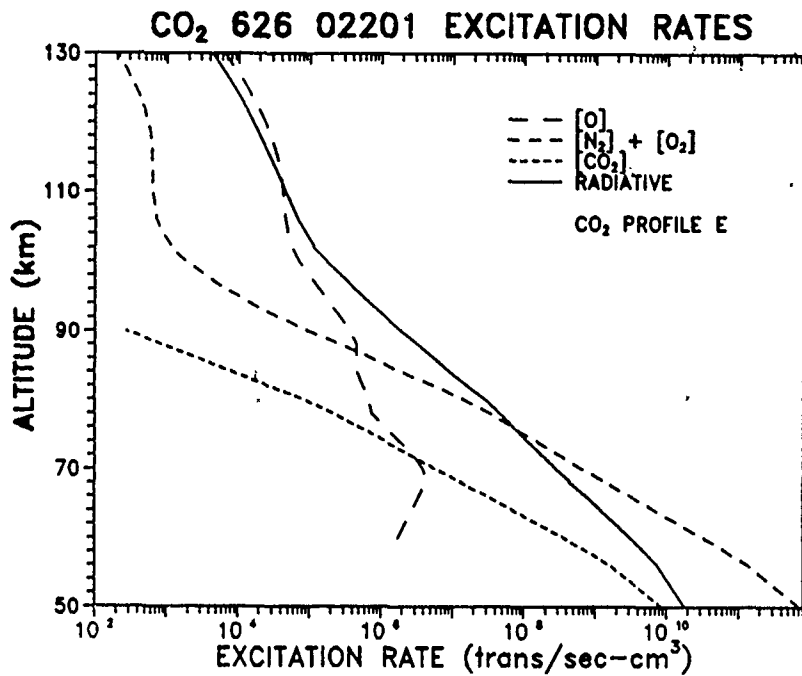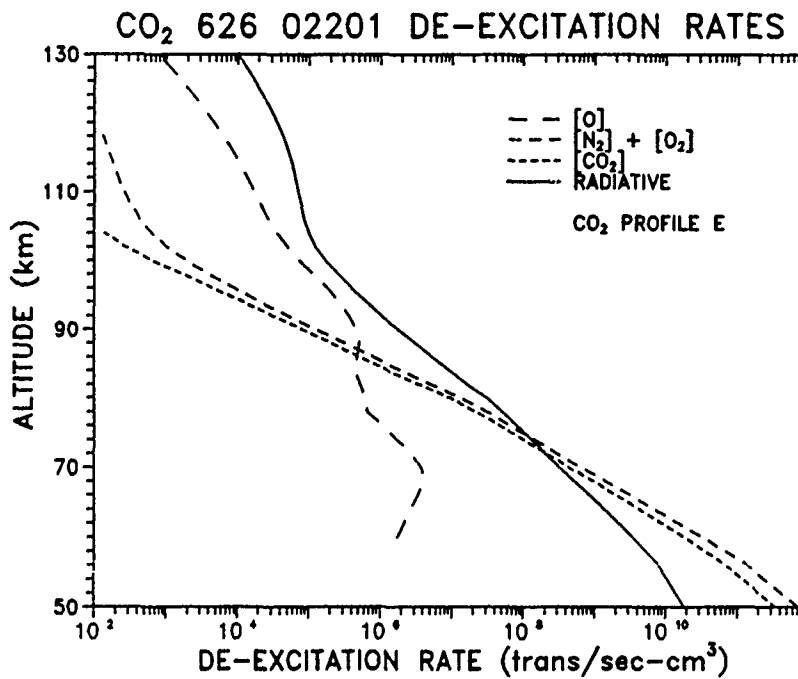nes. In the thermosphere, however, the elevated temperature Doppler-broadens the lines, resulting in absorption relatively far from the line centers. In fact, one can infer from the shape of the 150-km curve in Figure 14 that only a small fraction of the photons absorbed at that altitude comes from the line centers.

Another factor contributing to the absorption, in the thermosphere, of photons emitted at much lower altitudes is that the elevated temperature there broadens the distribution of absorbing rotational states. This greatly increases the probability of absorbing upwelling photons in the lower-opacity higher-J transitions.

In Figure 14, the solid bar overprinting the contribution of the 40-km layer is the contribution of the lower boundary to the pumping at 150 km. The size of this contribution, which approximates the pumping due to emitters in the space below 40 km, is nearly 5% of the total. This shows that it is important to include boundary effects even for very thick bands such as this one. The other observation points in Figure 14 have negligible boundary contributions, however.

Figures 15 and 16 give the layer contributions to the pumping in the 636 and 628 00001-01101 bands for other observation points. Comparison with Figure 14 shows that, compared to the thicker band, the source distributions are less local, and also that the lower-altitude and lower-boundary emission play an even more significant role in the absorption at the highest altitudes. Figure 17 gives similar information for the 626 01101-02201 band.

2. Limb Radiance

Using the vibrational temperatures generated by our model and the bands listed in Table 1, we calculated the limb radiances with our LBL code, NLTE *(Wintersteiner and Sharma, 1985)* and compared the results with the SPIRE data set. This code calculates the integrated radiance in each nonoverlapping Voigt line, and then determines the spectral radiance by degrading each line profile according to the spectrometer response function and summing over the lines.

a. SPIRE Data Set

The Spectral Infrared Rocket Experiment (SPIRE) observed the earthlimb in the 1.4-16.5 μm spectral region. There were twelve spatial scans, each comprising a number of spectral limb scans with tangent heights ranging from 0 to 200 km. Seven spatial

PHOTON ABSORPTION RATE--LAYER CONTRIBUTIONS

Figure 14. Fractional layer contributions to the total radiative excitation in the 626 00001-01101 band calculated for observation points at 70, 90, 110, and 150 km. The contributions are normalized to unity. The lower boundary contribution for the 150 km observation point is represented by the solid bar at 40 km.

PHOTON ABSORPTION RATE--LAYER CONTRIBUTIONS
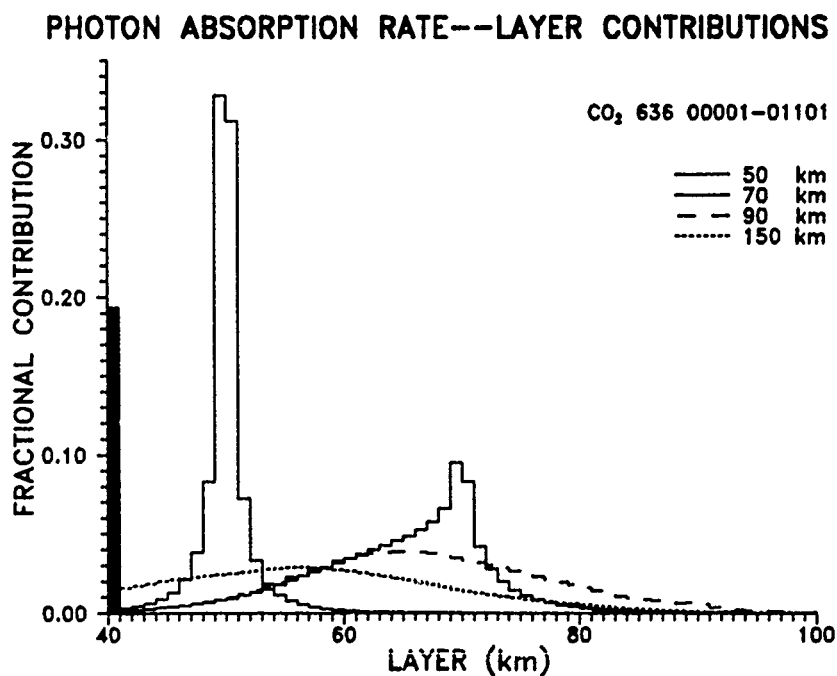
Figure 15. Fractional layer contributions to the total radiative excitation in the 636 00001-01101 band calculated for observation points at 50, 70, 90, and 150 km. The contributions are normalized to unity. The lower boundary contribution for the 90- and 150- km observation points are represented by the solid and hatched bars at 40 km, respectively.

37
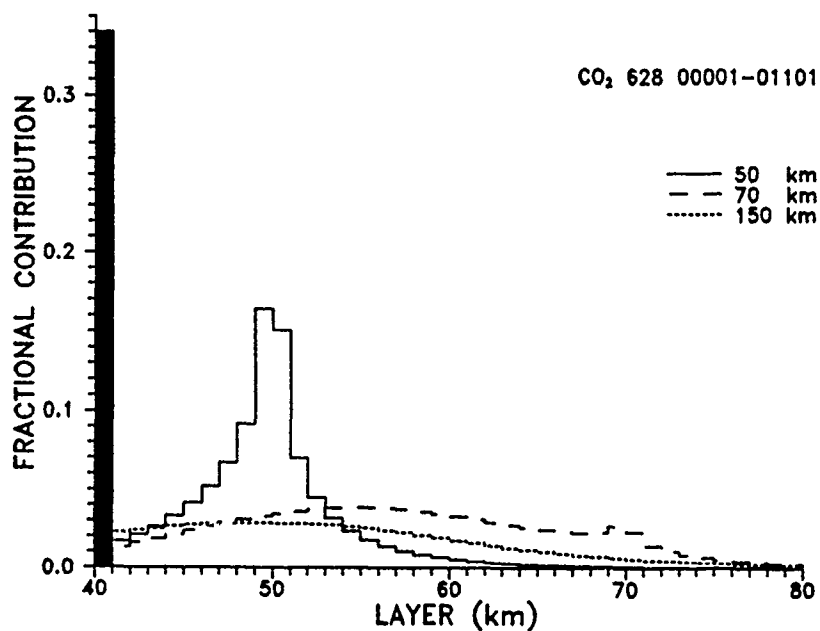
Figure 16. Fractional layer contributions to the total radiative excitation in the 628 00001-01101 band calculated for observation points at 50, 70, and 150 km. The contributions are normalized to unity. The lower boundary contribution for the 150 km observation point is represented by the solid bar at 40 km.

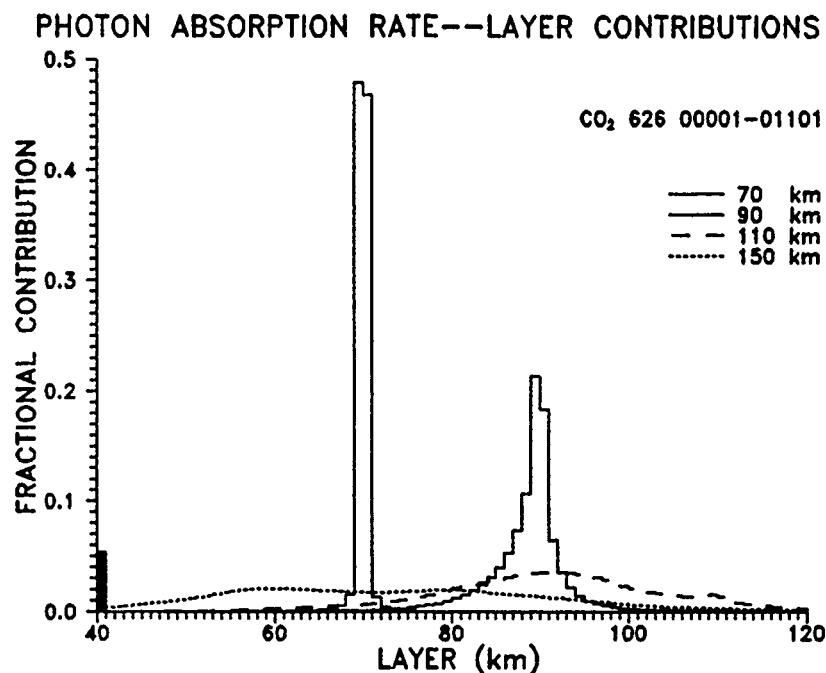## PHOTON ABSORPTION RATE--LAYER CONTRIBUTIONS
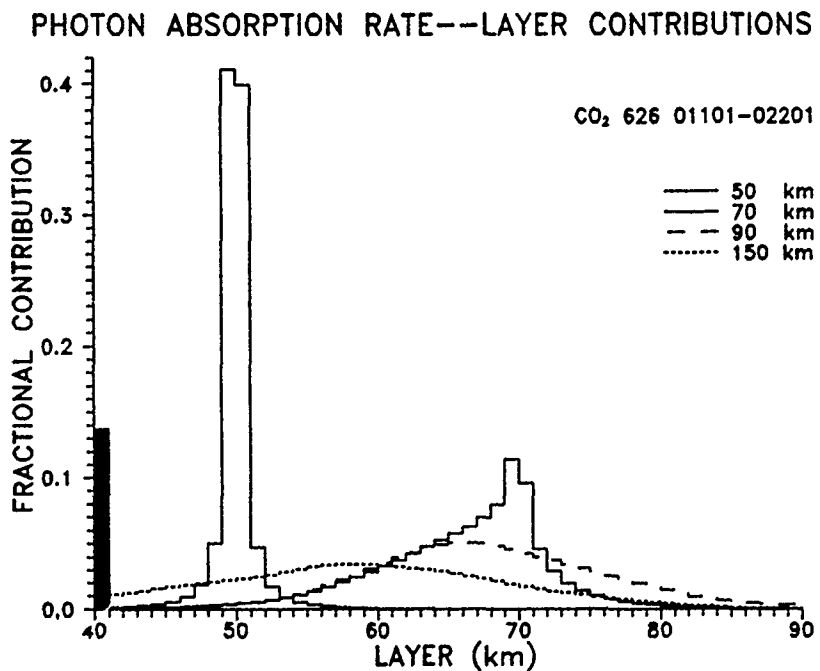
Figure 17. Fractional layer contributions to the total radiative excitation in the 626 01101-02201 band calculated for observation points at 50, 70, 90, and 150 km. The contributions are normalized to unity. The lower boundary contribution for the 150 km observation point is represented by the solid bar at 40 km.

scans looked across the dawn terminator, the eighth looked almost entirely at darkened regions, and for the other four spatial scans the lines-of-sight were entirely sunlit. The principal results were summarized by *Stair et al (1985)*.

We evaluated all the spectral scans containing useful data at wavelengths greater than 13 μm, eliminating only those scans with tangent heights below 50 km because of detector saturation at 15 μm, those with tangent heights above 160 km because of poor signal-to-noise ratios, and those from spatial scan 12 that were contaminated by scattered light as the viewing path approached the Sun too closely. Figure 18 shows the band radiance data, obtained by numerically integrating the spectral radiance data after subtracting background noise equivalent to 8×10^{-10} watt/(cm^2-ster-μm).

SPIRE BAND RADIANCE, 13-16.5 μm
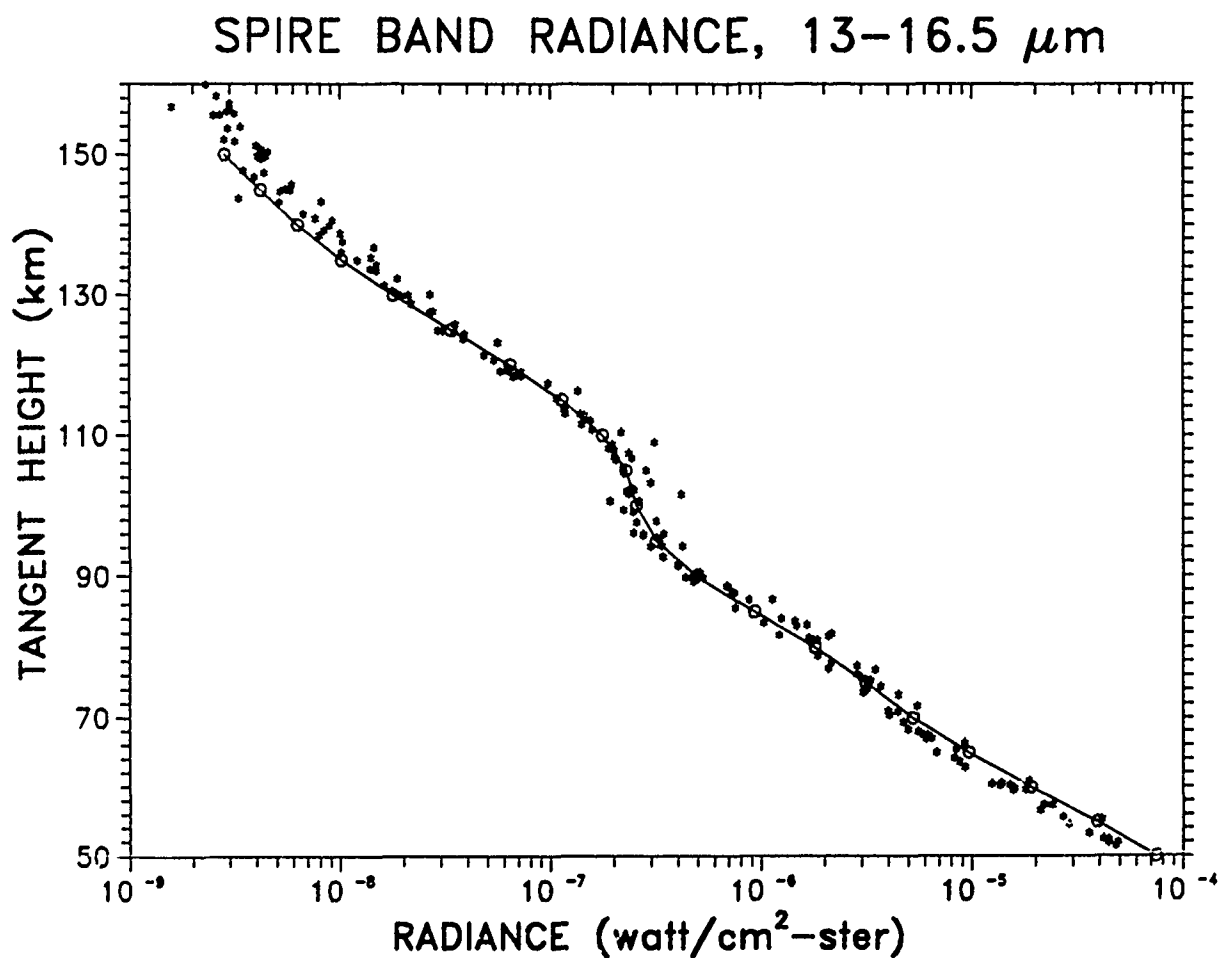
Figure 18. SPIRE limb radiance, in the band 13.0-16.5 μm, as a function of tangent height. The model prediction, using CO$_2$ profile E, is shown by the solid line.

Two features of these data are noteworthy. First of all, the band radiance is nearly the same for paths with tangent points between about 94 and 110 km. This is exactly the altitude region where [O] reaches a peak and k_O increases as the temperature increases rapidly with altitude. The efficiency with which oxygen atoms excite the bending mode is responsible for this feature: a roughly constant excited-state number density is maintained even as total CO_2 drops precipitously. Secondly, except for scan 8 paths with tangent heights above 95 km, there are no systematic differences between the limb radiances for the different scans. In other words the 15 μm emission, early in the morning, is not greatly affected by the extent to which the lines-of-sight are sunlit, or by other differences in ambient conditions along the viewing paths.

SPIRE BAND RADIANCE, 13−16.5 μm

●	MODEL TOTAL	
○	01101−00001	626 only
□	01101−00001	636 628 627
△	02201−01101	626 636
◇	1000x−01101	626
▽	03301−02201	626

Figure 19. Contributions of different bands to the total limb radiance for tangent paths between 50 and 110 km, according to the model using CO_2 profile E. Above 110 km the 626 01101-00001 band is almost entirely responsible for the observed radiance.

b. Limb Radiance Calculation

The solid curve in Figure 18 is the model prediction, using the O-atom rate constant given in Table 2 and CO_2 profile E. In Figure 19, we break down the radiance contributions according to bands or sets of bands for the lower altitudes. The minor isotopes and hot bands contribute a very significant portion of the total radiance on the 70- to 90-km paths, compared to the strongest 626 band. This is because they have somewhat higher vibrational temperatures and considerably less opaque optical paths. These distinctions are lost for viewing paths that lie primarily below 70 km, however, where the stronger minor bands also become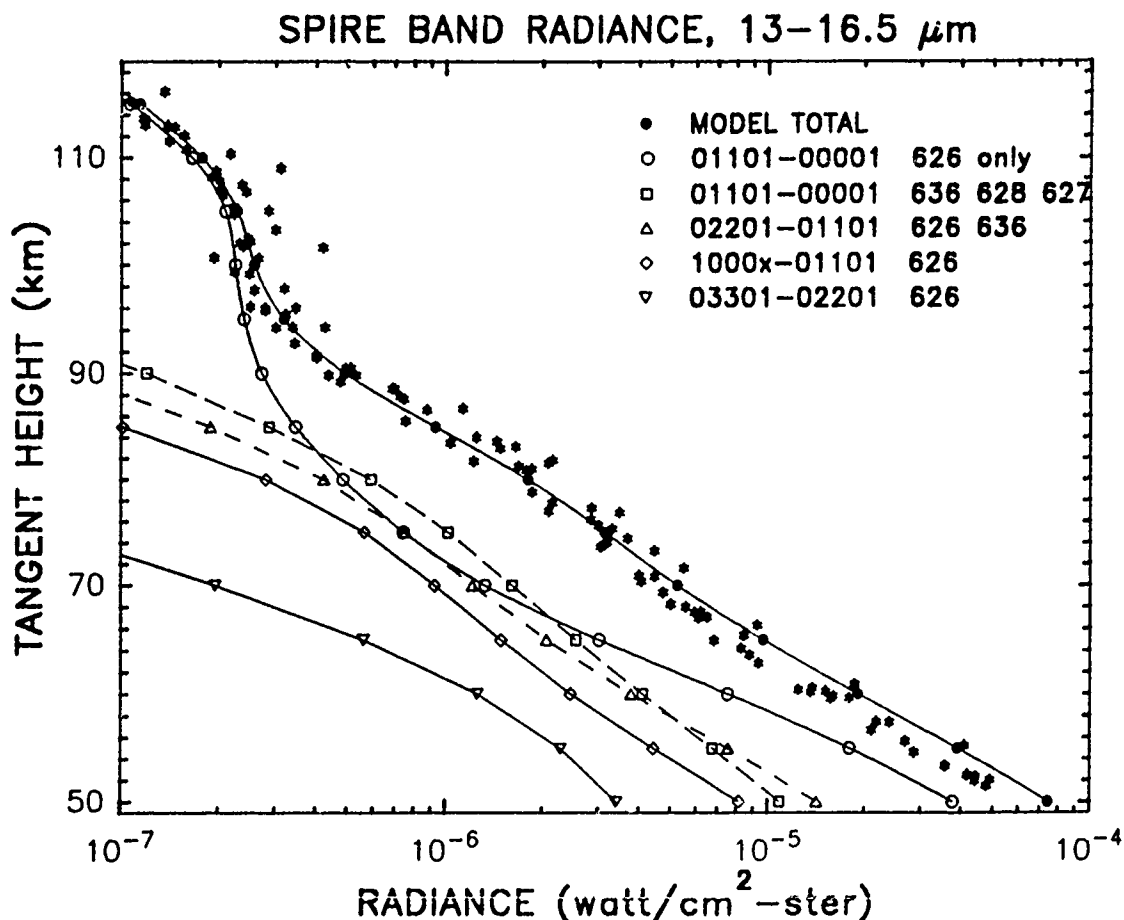 strongly self-absorbed. The fact that the 626 01101-00001 contribution dominates for these low tangent paths shows that a large fraction of the observed radiance comes either from weak high-J lines or from the wings of stronger lines. In fact, for a 50-km tangent path, transitions involving rotational states with $J \geq 30$ contribute about 25% of the total observed radiance; for $J \geq 40$ the contribution is only about 10%. In contrast, nearly half of the observed radiance originates in the lowest layer, between 50 and 51 km in altitude. It follows that the bulk of the observed radiance comes from the line wings for such low-lying tangent paths, rather than from high-J lines.

Figure 20, giving the spectral radiance for a limb scan at 75 km, demonstrates the quality of the data that were integrated to get the band radiances. (The wavelength mismatch, which appears in many scans, results from a slight miscalibration of the instrument and was ignored.) The subsidiary peak at 15.4 μm is mostly due to the strongest 636 band. The 626 hot band Q branches at 13.9 and 16.2 μm, due to the 10001-01101 and 10002-01101 transitions, are readily identifiable. For lower tangent heights the 13.5 μm band (11101-02201) is also visible.

c. Determination of k_O

Because of the fact that no experimental measurements of k_O exist for temperatures below 2000 K, different parameterizations have been adopted for use in atmospheric models. They range from the low estimate of 2.4×10^{-14} cm^3/mol-s at 300 K by *Taylor (1974)* to the constant value of 2×10^{-13} cm^3/mol-s used by *Dickinson (1984)* and others. *Gordiets et al (1982)*, who modeled the thermospheric heat budget by including all the significant known energy sources and sinks, determined that the 15 μm cooling rates had to be higher than predictions based on accepted values and suggested a new parameterization for the rate constant that we still find to be low by a considerable amount.

SPIRE SCAN 1650-1651
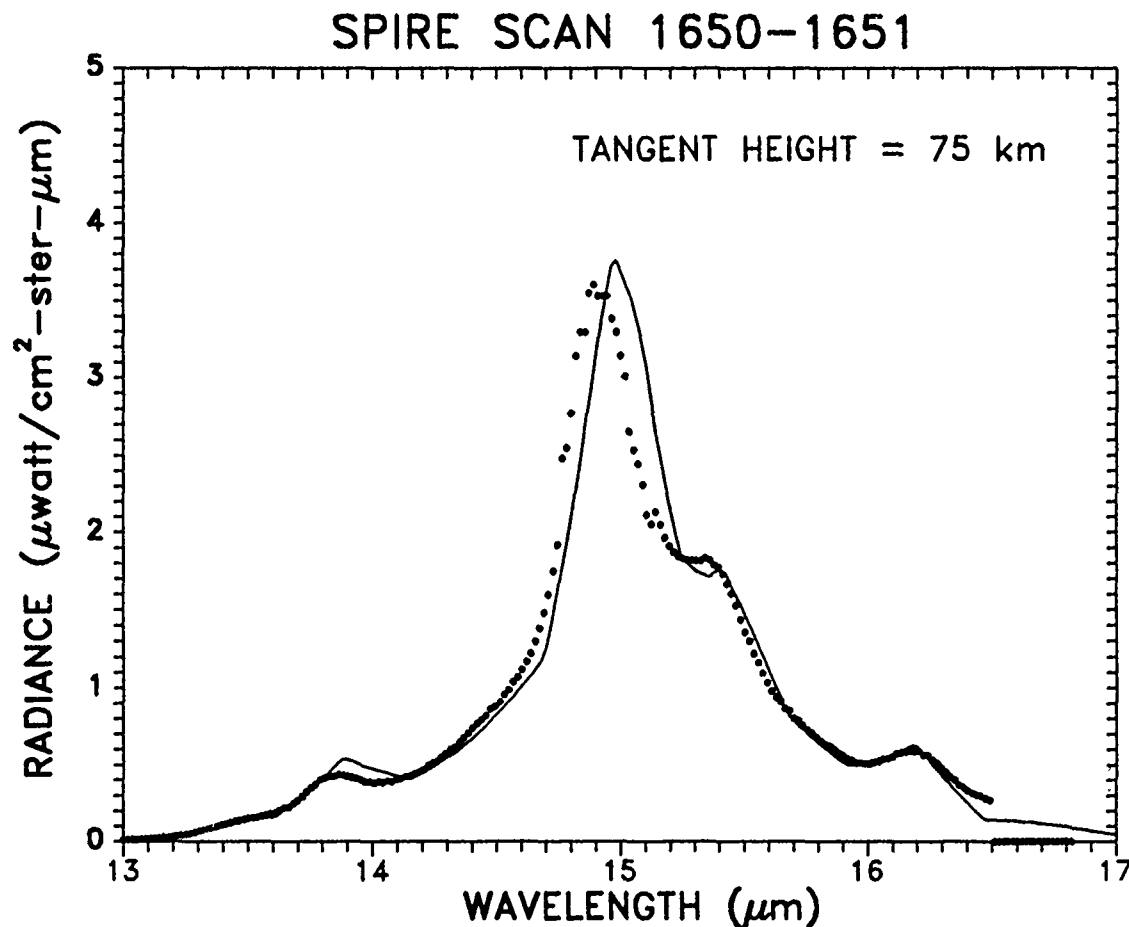
Figure 20. 15 μm SPIRE radiance data for a single spectral scan having a limb path centered at 75 km. The model prediction is given by the solid line.

Acceptance of the fact that commonly used values of k_o were too small at lower-thermosphere temperatures came about primarily because of the failure of models to reproduce the 94-110 km feature of the SPIRE band radiance. *Sharma and Nadile (1981)*, using an approximate treatment for radiative transport, showed that O-atom excitation of the bending mode explained this anomaly if a sufficiently large value were chosen for k_o. With the development of our more complete radiance model, we were able to let the rate constant be a free parameter according Eq.(26) and, by varying it, determine its low-temperature value more accurately *(Sharma and Wintersteiner, 1990)*.

Figure 21 compares the band-radiance data for limb paths above 90 km with three radiance profiles, each calculated using CO_2 profile E but with different values for the constant A_o in the O-atom rate constant. Figure 22 makes a similar comparison using the higher CO_2 mixing ratio profile, D. The results using profile D suggest a slightly smaller optimal value of A_o than those using profile E. The best overall description of the observations is obtained with a value of $A_o \sim 3.5$.

In Figure 22, the lowest-lying calculated curve illustrates the difficulty that arises when one tries to explain the 94-110 km "anomaly" without adequately accounting for O-atom excitation of the bending mode. In this case, there is no hint of a plateau in the
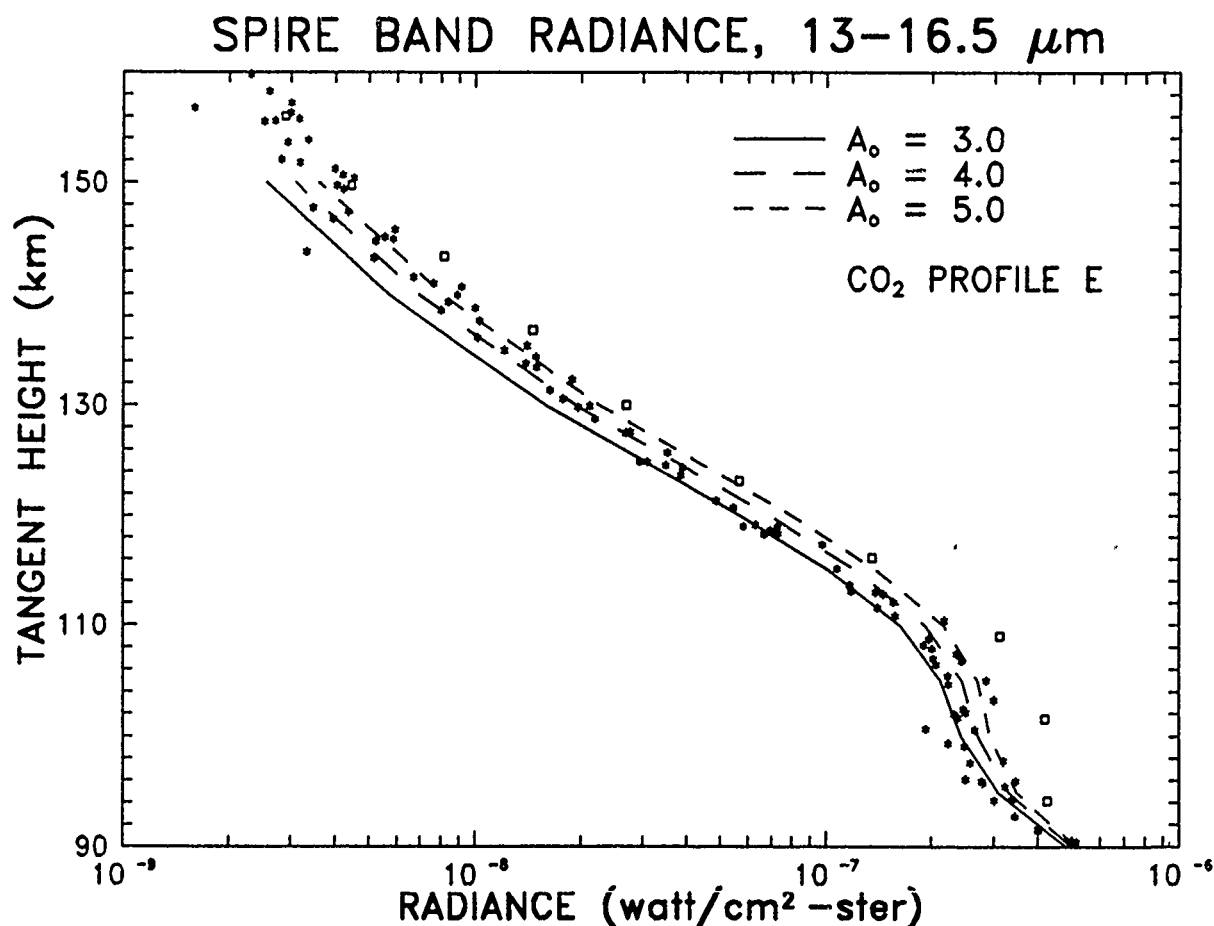
Figure 21. SPIRE limb radiance, 13 to 16.5 μm, for tangent heights above 90 km, in comparison with three separate calculations using CO_2 profile E. The three calculations assume that k_o has the form given in Eq. (26), and the values used for A_o are indicated.

SPIRE BAND RADIANCE, 13-16.5 μm
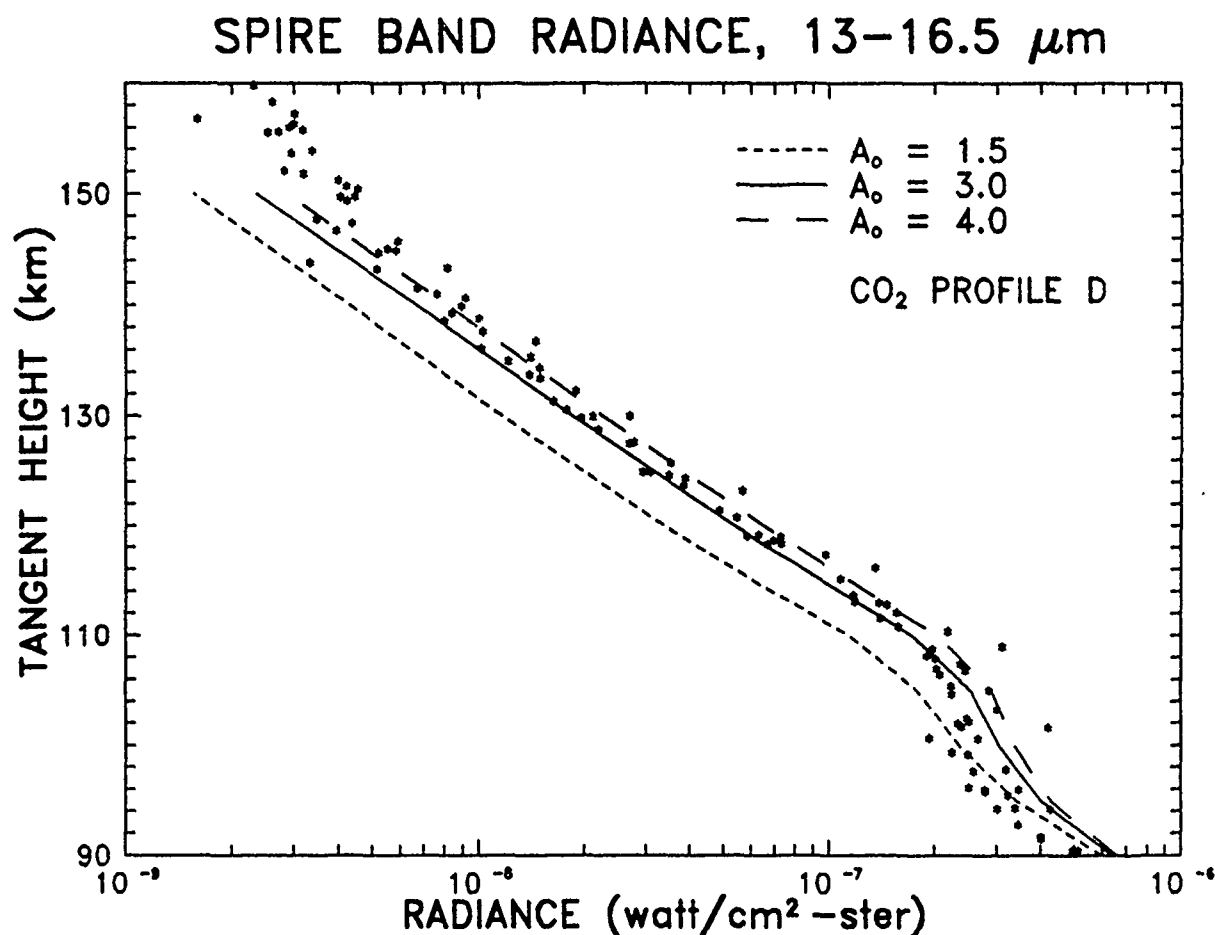
Figure 22. Same as Figure 21, but the radiances were calculated using CO_2 profile D.

model radiance, and its value is a factor of 2 or 3 too low for paths with tangent points above 110 km.

The principal sources of uncertainty in the value we have deduced for k_o are the CO_2 and O profiles. It is also possible that the kinetic temperature profile could be somewhat in error, resulting in some error in the prediction of the radiance. The radiative-excitation calculation itself contributes, by comparison, a negligible error. The N_2 and O_2 collision rate constants are well known, and we believe that the simplifications in the coupling scheme cannot affect the limb radiance calculation in a significant way.

44

The CO_2 concentration affects the retrieved value for k_o because the limb radiance prediction depends so strongly on it. For limb paths above 110 km the 15 μm bands are thin, so the radiance is proportional to the column density. At these altitudes, the measured CO_2 mixing ratios have a standard deviation of about 25% about the mean, and the MSIS total density has a standard deviation of about 15% with respect to the various data sets upon which it is based *(Hedin, 1988)*. Together, these lead to an error of about 30% in the CO_2 density that we use. We have shown in turn that with the fitting parameter A_o in the range 2.5 to 4.5, 30% across-the-board changes in $[CO_2]$ translate into approximately a 43% change in the retrieved value of k_o.

For lower altitudes, the "high" and "low" mixing ratio profiles are quite different, and the uncertainty in $[CO_2]$ is therefore greater. However the 626 fundamental is no longer thin, and the limb radiance is less sensitive to the assumed density. For tangent heights near 100 km, profile D results in a predicted radiance that is only about 25% greater than that for profile E. Since we believe that, for the 90-100 km range, models D and E are close to the upper and lower bounds on the mixing ratios that are likely to exist, the effect of uncertainties in $[CO_2]$ on the retrieved value of k_o is probably less than the 43% figure that we determined from the optically-thin regime.

Uncertainties in oxygen atom densities also affect the value we get for k_o. In our model k_o and $[O]$ appear only as a product, so when we vary k_o to ascertain its best value, we cannot distinguish the variation from a simple scaling of the $[O]$ profile. Therefore, the estimate of k_o automatically inherits the uncertainty of the oxygen-atom profile. *Hedin (1988)* reports that standard deviations between data and the MSIS-86 model for $[O]$ range from 15% to over 30%. The data sets that were used to produce MSIS are relatively sparse in the lowest part of the thermosphere, so in the region of interest to us we take 30% as an estimate of the uncertainty in $[O]$, and hence in the contribution of this factor to the error in k_o.

The limb radiance in the thermosphere is also sensitive to the temperature profile, particularly to the mesopause temperature. Therefore we ran our model with two FASCODE atmospheres *(Anderson et al, 1986)* having higher and lower mesopause temperatures, in order to assess the effect that a possible error in our nominal profile from MSIS would have on the value of k_o that we have deduced. Radiance results obtained using the midsummer profile, with a cold mesopause, are consistent with the SPIRE data when k_o assumes the value given in Table 2. However, the results obtained with the midwinter profile, with a warmer mesopause, exceed the experimental data and cannot be reconciled with them by adjusting k_o downward. This indicates that the

45

mesopause temperature is at least approximately correct and that k_o cannot be greatly in error on this account.

Taking into consideration the possible errors in $[CO_2]$, $[O]$, and temperature, we arrive at an uncertainty of about 55% in k_o in the temperature range accessible to us. In other words, we find that the optimal value of the fitting constant is

$$A_o \sim 3.5 \pm 1.9 \qquad (27)$$

Another source of uncertainty is our particular way of parameterizing the rate constant. Because of the aeronomical importance of this quantity, it certainly would be valuable to have reliable laboratory measurements of its temperature dependence. Whatever more detailed information may be forthcoming, however, the important point at this time is the confirmation that this rate constant has a value near $5\text{-}6 \times 10^{-12}$ $cm^3/mol\text{-}s$ in the lower thermosphere, which is much larger than has been recognized in the past.

d. The SPIRE "Nighttime" Scan

The SPIRE "nighttime" scan, scan 8, viewed a region that was geographically distinct from those seen by the terminator and daytime spatial scans. In Figure 21, the data points from this scan are denoted by squares. One can see that the scan-8 band radiance is consistently larger than the mean radiance of the other scans above 95 km, with enhancements ranging from 70% on the 102 km limb path to 30% on paths above 120 km. Below 90 km, no such pattern exists. This is peculiar because one would generally expect the nighttime CO_2 vibrational temperatures to be slightly lower than the daytime temperatures, leading to somewhat lower emission (all other things being equal) rather than what is observed. It also happens that the NO radiance in the 5.3 μm band shows very similar behavior between 95 and 120 km, with the scan-8 radiances as much as twice the mean values *(Stair et al, 1985)*.

We know of no explanation for this coincidence, except the possibility of an enhanced density of oxygen atoms along these particular lines of sight. Alternative explanations *(Stair et al, 1985; Caledonia et al, 1985)* involve local constituent variations resulting from diurnal or auroral effects. In the case of CO_2 variations, one might expect photodissociation to lead to depleted concentrations in the daytime. However, the response time of $[CO_2]$ to insolation is much too long *(Trinks and Fricke, 1978)* to account for differences in density large enough to explain the enhanced nighttime emission.

An auroral explanation for the scan-8 results is equally unlikely. First, the SPIRE experiment took place at a quiet time with no observed auroral activity. If auroral electron precipitation were occurring, one would expect an enhanced 4.3 μm CO_2 signature *(Kumer, 1977b; Stair et al, 1985; Picard et al, 1987)*, which does not appear. In addition, it can be shown that auroral electrons excite bend-stretch states too weakly to enhance their populations. Finally, enhanced species concentrations due to auroral activity can also be ruled out. Recent auroral activity would be a sufficient explanation for the a factor of two increase in [NO], but there is no reason for it to be accompanied by a large enhancement of the CO_2 column density. Finally, atmospheric heave resulting from Joule heating which often accompanies auroral activity is also ruled out because a heaved atmosphere would be richer in CO_2 while being depleted in NO. Moreover, there is no sign of geomagnetically active conditions required for significant Joule heating; Ap values were modest in the range 16-22.

The nitric oxide fundamental is excited by the same mechanisms as the carbon dioxide bending mode. The rate constant for deactivation of the v = 1 level by collisions with oxygen atoms is very large—6.5×10^{-11} cm^3/mol-s at 300 K *(Fernando and Smith, 1979)*. Radiative excitation is important, but excitation by O-atom collisions dominates above 110 km and is important as low as 100 km *(Caledonia and Kennealy, 1982)*. Model results *(Winick et al, 1987)* show that doubling [O] enhances the limb radiance consistently by about 70% for paths with tangent points between 90 and 120 km. For the case of CO_2 15 μm emission, we find that an [O] profile augmented by 150% near 100 km and 50% above 120 km produces a satisfactory enhancement of the limb radiance. Such a profile could also be responsible for 5.3 μm enhancements of the size that are observed, and we hereby suggest that elevated levels of atomic oxygen were probably responsible for the anomalously high radiance data. The enhanced peak model density of about 7×10^{11} atoms/cm^3 is well within the range of measured values and is slightly higher than the theoretical maximum of 5.5×10^{11} given by *Sharp (1985)*. The only difficulty is that there is no experimental indication of higher-than-normal NO emission above 130 km, as there is for CO_2. One expects [NO] to be quite variable, however, certainly much more so than CO_2, so a slightly diminished NO density along the higher scan-8 lines-of-sight is possible and could account for the observations.

47

This page intentionally blank.

III. CO_2 4.3 μm EMISSION

We have incorporated the RAD algorithm in a model for predicting CO_2 emission in the 4.3 μm bands for quiescent conditions. All vibrational states having one or more quanta of asymmetric stretch, ν_3, emit at this wavelength, and with Einstein A coefficients on the order of 400 trans/mol-s, these bands are among the strongest and most important sources of infrared radiation in the atmosphere.

The lowest-lying 4.3 μm transition is the ν_3 fundamental, 00011-00001. As with the ν_2 transitions at 15 μm, it is necessary to consider the contributions of minor isotopes in these bands. The lowest-lying hot band, 01111-01101, is also important because of the significant probability that the lower state is occupied. Other 4.3 μm bands which are important aeronomically originate in higher-lying states having both ν_1 and ν_3 excitations, or in states that are closely coupled to them. These bands are energetically accessible because of the absorption of shorter-wave solar photons in ground-state connected transitions *(James and Kumer, 1973)*. In other words, absorption at 2.7 and 2.0 μm is followed, with high probability, by emission at 4.3 μm, and any simulation of daytime conditions must properly account for these fluorescent processes. For example, absorption in the 00001-10011 and 00001-10012 bands at 2.7 μm is followed by emission at 4.3 μm in all the bands connecting 10011, 10012, and 02211 (which is coupled to 10011 and 10012) with the lower states 10001, 10002, and 02201. Figure 1 provides some reference for this discussion, and Table 3 lists the bands we have considered. In the past, the populations of these states have been modeled in different ways by many authors, including *James and Kumer (1973)*, *Kumer and James (1974)*, *Kumer (1977a)*, *Shved et al (1978)*, *Sharma and Wintersteiner (1985)*, and *Lopez-Puertas et al (1986b)*.

The work reported in this section was performed in close cooperation with Dr. Henry Nebel of Alfred University. Dr. Nebel, a fellow in the USAF-UES Summer Faculty Research Program sponsored by Air Force Office of Scientific Research, worked at the Geophysics Lab at Hanscom Air Force Base during the periods of collaboration with us.

A. Outline of the Model

A common thread that connects all CO_2 states having ν_3 excitations is the near-resonant intermolecular V-V process whereby N_2 vibration is exchanged with quanta of asymmetric stretch:

$$CO_2(\nu_1\nu_2\nu_3) + N_2(v=0) \rightleftharpoons CO_2(\nu_1\nu_2\nu_3\text{-}1) + N_2(v=1) \qquad (28)$$

49
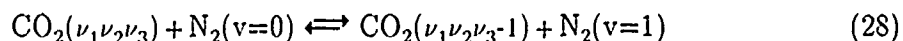
TABLE 3. CO_2 bands included in the model for emission at 4.3 μm.

Isotope	Upper State	Lower State	Transition Energy (cm^{-1})	Transition Wavelength (μm)	A (s^{-1})
626	00011	00001	2349.14	4.26	436.0
	01111	01101	2336.63	4.28	444.2
	10012	10002	2327.43	4.30	448.9
	02211	02201	2324.14	4.30	453.9
	10011	10001	2326.60	4.30	452.2
	11112	11102	2315.24	4.32	456.3
	03311	03301	2311.67	4.33	460.6
	11111	11101	2313.77	4.32	460.0
	20013	20003	2305.26	4.34	459.3
	20012	20002	2306.69	4.34	459.9
	20011	20001	2302.52	4.34	466.4
636	00011	00001	2283.49	4.38	371.5
	01111	01101	2271.76	4.40	366.4
	10012	10002	2261.91	4.42	363.2
	02211	02201	2260.05	4.42	360.0
	10011	10001	2262.85	4.42	365.5
628	00011	00001	2332.11	4.29	388.2
627	00011	00001	2340.01	4.27	395.7

Any isotope of CO_2 may be involved. The rate constant for this process has been measured for the 626 isotope *(Rosser et al, 1969; Gueguen et al, 1975; Inoue and Tsuchiya, 1975)* and we assume that it is not much different for the other isotopes. Its value, which is about $5\text{-}6 \times 10^{-13}$ cm^3/mol-s at mesospheric and lower thermospheric temperatures, is great enough that the process is a determining factor for the vibrational populations of <u>both</u> CO_2 and N_2, which therefore cannot be calculated independently *(Kumer and James, 1974)*.

While it is true that all CO_2 states with ν_3 excitation, including all isotopes, are coupled to N_2 vibration, it is not necessary to use all of them in a simultaneous calculation. We do explicitly couple $N_2(v=1)$ with $CO_2(00011)$ for the isotopes 626, 636, 628, and 627. We then solve a set of simultaneous equations, patterned after Eq.(24) in Section I, at each altitude for these five states; line-by-line radiative transfer in the four ν_3 fundamental bands is included, as well as other processes that are listed in Table 4. For daytime conditions, direct solar pumping at 4.3 μm is accounted for by use of solar-flux absorption coefficients from our line-by-line code, SABS *(Wintersteiner and Joseph, 1986)*. Populations of CO_2 bend-stretch states are regarded as known quantities, based upon the model discussed in Section II. This is sufficient to determine the N_2 vibrational temperature quite accurately (as well as the $^iCO_2(00011)$ vibrational temperatures, where the superscript refers to the isotopic variant). Using the N_2 vibrational temperature as a known quantity, separate calculations can then be performed for higher-lying states. For example, the 01111 populations are found in an independent calculation that assumes that the $N_2(v=1)$ and CO_2 bend-stretch populations are known, and calculates the radiative transfer in the 01101-01111 band using the RAD algorithm.

The method that we use to calculate the populations of the $\nu_1 + \nu_3$ states, and associated states, above 3500 cm^{-1} has been described *(Sharma and Wintersteiner, 1985; Wintersteiner and Joseph, 1986)*. Although the codes have been rewritten and the N_2 vibrational temperature determined by the coupled calculation is now used, the basic method is the same and we do not elaborate on it except to make the following comments. These calculations do <u>not</u> involve transfer of atmospheric radiation because the pumping of these high-lying states (see Figure 1) by volume emission within the atmosphere is negligible compared to other excitation mechanisms. In particular, in daytime the intense solar flux at 2.7 and 2.0 μm populates these states effectively. Relatively little of the energy is reemitted at these wavelengths because of the strong competition from the 4.3 μm emission, so the overall short-wave flux is almost entirely solar in origin. The 4.3 μm photons of course can be absorbed in the atmosphere, but in

51

TABLE 4 a. Reactions included in the model for the ${}^{i}CO_2(00011)$ and $N_2(v=1)$ populations, and in the model for ${}^{i}CO_2(01111)$ populations. The superscript i refers to each of the isotopic indices 626, 636, 628, and 627. In reactions 2 and 8, M refers to N_2 and O_2. The exothermicity given is for reactions involving the major isotopes only.

Reaction	Type	Rate Constant	Exo-thermicity (cm^{-1})
${}^{i}CO_2(00011) + N_2(v=0) \rightleftharpoons {}^{i}CO_2(00001) + N_2(v=1)$	V-V	k_1	19.2
${}^{i}CO_2(00011) + M \rightleftharpoons {}^{i}CO_2(03301) + M$	V-V	k_2	345.9
${}^{i}CO_2(00011) + O_2(v=0) \rightleftharpoons {}^{i}CO_2(01101) + O_2(v=1)$	V-V	k_3	125.4
${}^{i}CO_2(00011) + O \rightleftharpoons {}^{i}CO_2(03301) + O$	V-V	k_4	345.9
$N_2(v=1) + O_2(v=0) \rightleftharpoons N_2(v=0) + O_2(v=1)$	V-V	k_5	773.5
$N_2(v=1) + O \rightleftharpoons N_2(v=0) + O$	V-T	k_6	2329.3
${}^{i}CO_2(01111) + N_2(v=0) \rightleftharpoons {}^{i}CO_2(01101) + N_2(v=1)$	V-V	k_7	6.7
${}^{i}CO_2(01111) + M \rightleftharpoons {}^{i}CO_2(04401) + M$	V-V	k_8	332.3
${}^{i}CO_2(01111) + O_2(v=0) \rightleftharpoons {}^{i}CO_2(02201) + O_2(v=1)$	V-V	k_9	112.5
${}^{i}CO_2(01111) + O \rightleftharpoons {}^{i}CO_2(04401) + O$	V-V	k_{10}	332.3

TABLE 4 b. Rate constants describing the reactions, in the forward direction. Units are cm^3/mol-s.

Symbol	Parameterization	Value at 300 K (cm^3/mol-s)
k_1	$8.66 \times 10^{-12} T^{-0.5}$	5.0×10^{-13}
k_2	$2.22 \times 10^{-15} + 1.22 \times 10^{-10} \exp(-76.75/T^{0.33})$	3.5×10^{-15}
k_3	$-9.6 \times 10^{-15} + 6.0 \times 10^{-17} T$	8.4×10^{-15}
k_4	$1.155 \times 10^{-14}\sqrt{T}$	2.0×10^{-13}
k_5	$3.464 \times 10^{-19}\sqrt{T}$	6.0×10^{-18}
k_6	$1.161 \times 10^{-21} T^{2.6}$	3.2×10^{-15}
k_7	same as k_1	5.0×10^{-13}
k_8	same as k_2	3.5×10^{-15}
k_9	same as k_3	8.4×10^{-15}
k_{10}	same as k_4	2.0×10^{-13}

the non-LTE regions most of these bands are thin and as a result the spatial redistribution is not a prominent factor in the determination of the upper-level populations. At night, there is no effective mechanism for populating these levels at all, except the intermolecular V-V process, Eq.(27), which of course runs in reverse as well. As a result, the vibrational temperatures of these states are either close to the kinetic temperature at all altitudes above the stratopause, or else fall well below it. Because of the large state energies, these populations are therefore very small and the number of photons emitted is negligible in comparison to the numbers emitted in other 4.3 μm bands. We did try a rudimentary radiative-transfer calculation assuming that the 2.7 μm bands were thin and that the average emissivity of the atmosphere was that of a blackbody at the stratopause temperature. This modification did not enhance the vibrational temperatures very much, however, confirming the earlier conclusion that at night these states do not emit sufficiently strongly to compete with the more prominent bands.

In order to simulate the SPIRE data set, we used the model atmosphere described in Section II.A.2. All of the calculations reported below used Model D for [CO_2].

B. Results for the SPIRE Simulation

We ran our model in order to simulate the conditions of the SPIRE experiment *(Stair et al, 1985)*. This was a more complicated exercise than the effort with which we calculated the long-wave radiance (Section II), because of the varying role played by the solar pumping of the states in question and the need to distinguish the scans according to the apparent position of the Sun.

1. SPIRE Data Set

The experimental 4.3 μm radiance, integrated between 4.12 and 4.49 μm, is shown in Figure 23. Data from the terminator scans are distinguished from that from the daylit scans. The great disparity between these two sets illustrates the role that solar pumping plays in exciting the CO_2 states that emit at 4.3 μm.

Of the twelve spatial scans for which data were accumulated, the last four, scans 9 through 12, looked roughly toward the east and had lines-of-sight that were illuminated by the Sun over their full extent. The solar zenith angle varied along each viewing path and also was different for paths of different spatial scans. Nevertheless the conditions were generally "low Sun" conditions. For those spectral scans with tangent points near 90 km, the solar zenith angle at the tangent point was between 78° and 84° for these
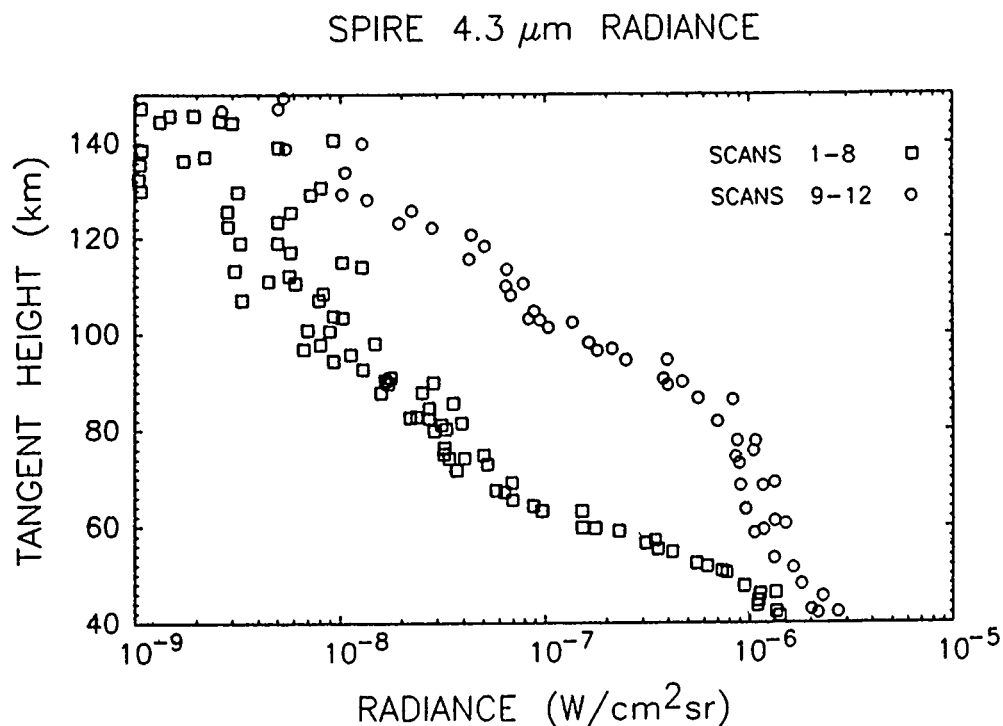
SPIRE 4.3 μm RADIANCE

Figure 23. SPIRE limb radiance, in the band 4.12-4.49 μm, as a function of tangent height. Terminator scans (1-8) are distinguished from daylight scans (9-12).

four spatial scans *(W.F. Grieder and C.I. Foley, private communication)*. We modeled these "daytime" scans with a solar zenith angle of 78°, but the results are not greatly different for 84°.

Scans 1 through 8 present different problems, because in each case the views were across the dawn terminator, to the northwest or west. There were great differences. from scan to scan, in the portions of the viewing paths that were sunlit. The rocket was in the sunlight above 200 km, so for all scans the path segment nearest the sensor was also sunlit. For some of the spatial scans (especially scan 8) the terminator was relatively close to the rocket. The sunlit portions of the spectral scans' viewing paths were therefore short and at high altitudes where few emitters are found, and the bulk of the line-of-sight paths with most of the CO_2, being more distant, was in the dark. For others, however, the visible terminator was relatively near the tangent points, or even beyond them. In such cases, portions of the paths with significant numbers of emitters. or even the majority of emitters, were sunlit.

These geometrical considerations would seem to suggest that, because of the great importance of solar pumping in the excitation of the states that emit at 4.3 μm, the data should show great differences in limb radiance for the different spatial scans when one compares spectral scans with similar tangent heights. In fact, except for paths with tangent points above 110 km where the signal to noise ratio is poor, there is remarkably little overall scatter among the results for the eight terminator scans. This can be seen in Figure 23. Moreover, there are no systematic differences among the spatial scans. This is partly attributable to the fact that the Sun is so low that the solar flux at 4.3, 2.7, and 2.0 μm is severely attenuated as it passes through lower portions of the atmosphere. (For a solar zenith angle of 95^0, solar photons arriving at an observer at an altitude of 84 km would pass through atmospheric layers below 60 km. For some parts of some SPIRE viewing paths, the solar zenith angle is greater than 105^0.) Therefore, the effective "infrared terminator"—although not precisely determined because the attenuation is continuously variable along the path to the Sun and depends on wavelength, rather than being cut off sharply as at hard earth—is much higher than the visible terminator at any given location. Thus for the SPIRE lines-of-sight, the solar infrared-illuminated portions are not as long or important as the visible-illuminated portions. The overall effect of this is that the viewing paths mostly traverse regions where conditions are quite similar to nighttime conditions as far as the excitation mechanisms for the states emitting at 4.3 μm are concerned, or at least are more similar to nighttime conditions than to "low Sun" daytime conditions.

2. Vibrational Temperatures

Figure 24 gives the vibrational temperatures of the CO_2(00011) state for the four isotopes we studied, using the SPIRE model atmosphere and assuming no solar excitation. The great extent by which the isotopic vibrational temperatures differ is very important for radiance studies, because it implies that the populations of the 00011 state of the minor isotopes are not very much smaller than that of the 626 isotope at certain altitudes. Together with the fact that the atmosphere is much less opaque to emission from these states, this means that much if not most of the radiance observed on limb paths through the upper mesosphere and lower thermosphere originates in the minor isotopic states rather than that of the 626 isotope.

The reasons for such great differences in the vibrational temperature are basically similar to those responsible for the similar behavior shown in Figures 7 and 8 for the lowest-lying ν_2 state, 01101. That is, for the minor isotopes' bands the atmosphere is
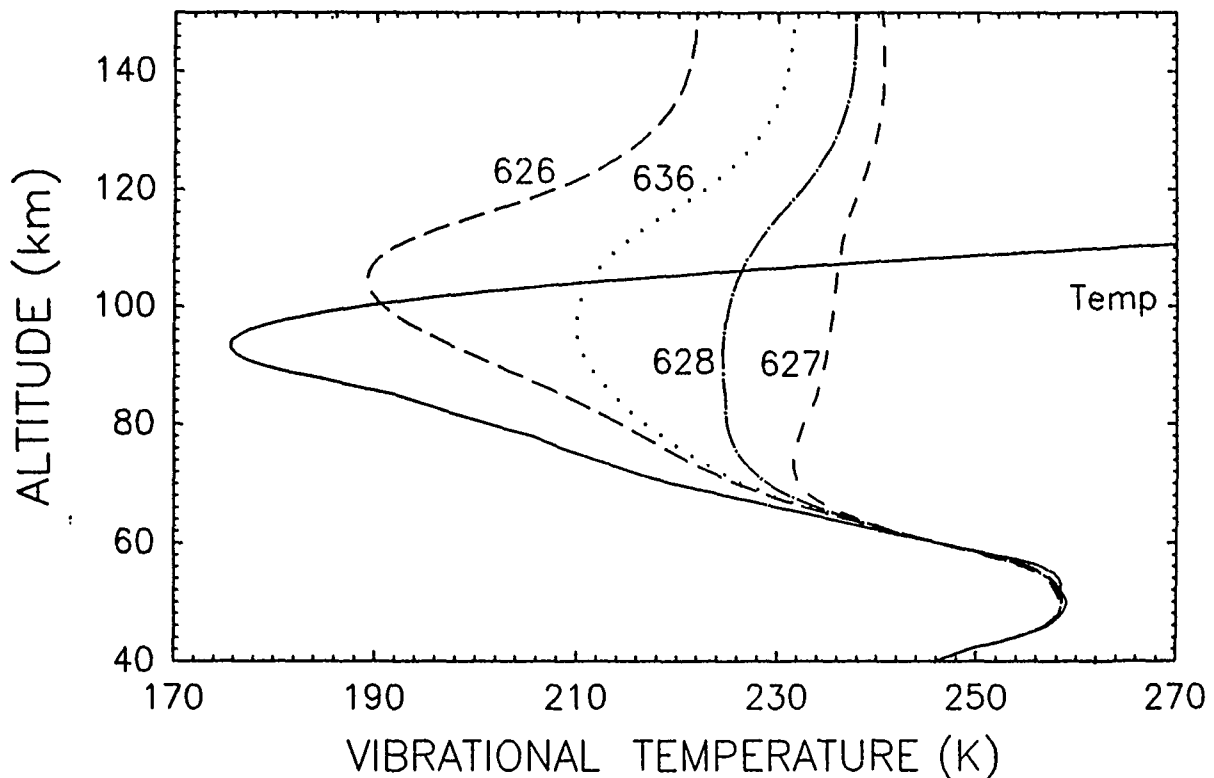
55

00011 STATE NIGHTTIME

Figure 24. Vibrational temperatures for the 00011 state for four CO_2 isotopes, for night-time conditions. The kinetic temperature is shown for purposes of comparison.

less opaque, and photons from the warm stratopause region migrate more freely into the mesosphere, where they can be absorbed and can contribute to the enhanced populations. This migration is also partly responsible for the fact that the 626 vibrational temperature is greater than the kinetic temperature in the mesosphere, but in that case the mean free path for photons is much shorter and the effect is much less pronounced.

Another consideration is that the 626 lines are so strongly self-absorbed, even as high as the mesopause, that photon escape is improbable; this also contributes to the 626 vibrational temperature being higher than the kinetic temperature. In contrast, the 01101 vibrational temperature is slightly below the kinetic temperature at the meso-pause primarily because, in the weaker ν_2 fundamental, photons can more easily escape.

Figure 25 gives the same information for the daytime "low Sun" calculation, using a solar zenith angle of 78°. Solar flux absorption in the 4.3 μm bands is responsible for the enormous differences between these results and the nighttime results shown in Figure 24. In fact, it is responsible for most features of these profiles above 60 km. The dropoff

00011 STATE DAYTIME
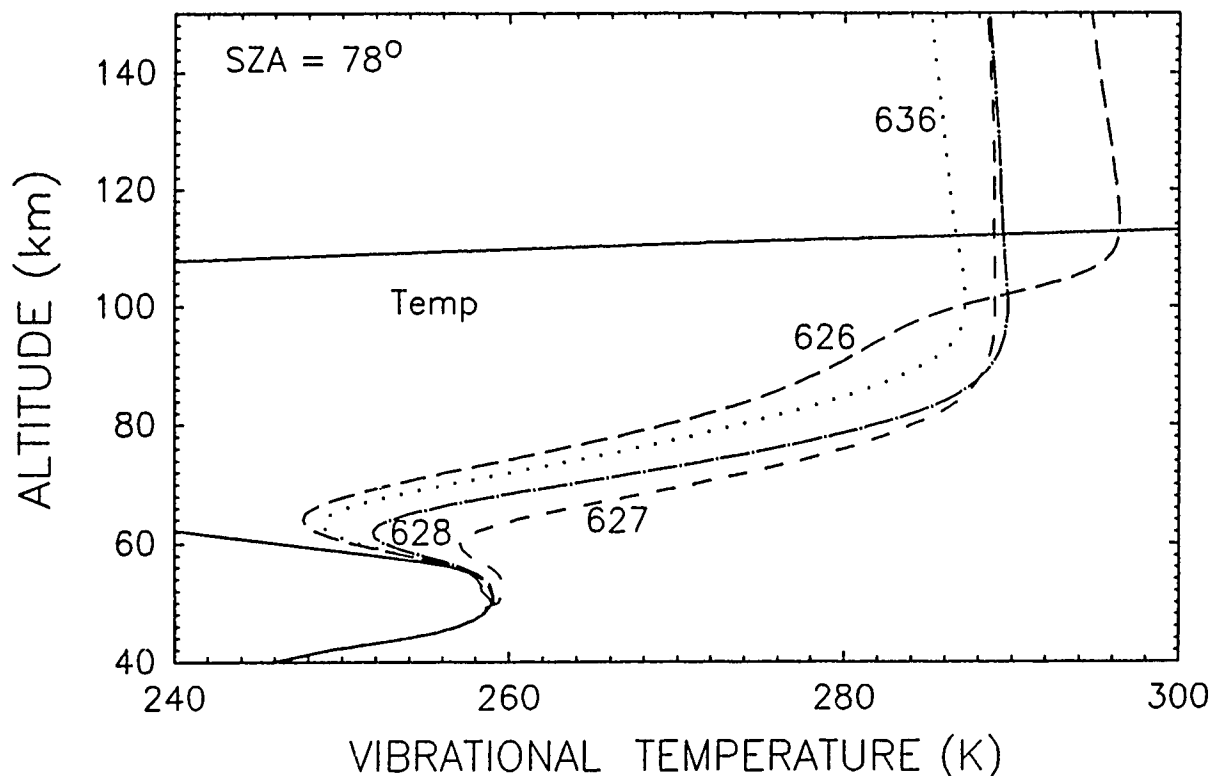
Figure 25. Vibrational temperatures for the 00011 state for four CO_2 isotopes, for daytime conditions with a solar zenith angle of 78°.

in the vibrational temperatures below 100 km occurs as the solar flux is bleached out. In the mesosphere the differences between the isotopic vibrational temperatures are largely due to the fact that the solar flux penetrates to lower altitudes in the minor-isotope bands. At high altitudes the vibrational temperatures are nearly independent of solar zenith angle (at least, for angles less than 90°) because of the absence of attenuation, but below 100 km the 00011 vibrational temperatures can be much higher than are shown in Figure 25 if the solar zenith angle is smaller. In fact, for solar zenith angles of about 45°, which occur near noon in the summer at subarctic latitudes, 00011 vibrational temperatures may exceed 300 K near the mesopause.

In the thermosphere where the lines are thin the 636 vibrational temperature in Figure 25 is lower than the other vibrational temperatures because the 636 ν_3 fundamental is a somewhat weaker band (see the Einstein coefficients in Table 3) and there is a lower probability per molecule for absorption of solar flux.

Figure 26 gives the N_2 vibrational temperatures from the same calculations that produced Figures 24 and 25, and also, for the purposes of comparison, the 626 $CO_2(00011)$ vibrational temperatures. One can see that at the lower altitudes the N_2

N_2 AND CO_2 (00011) VIBRATIONAL TEMPERATURES
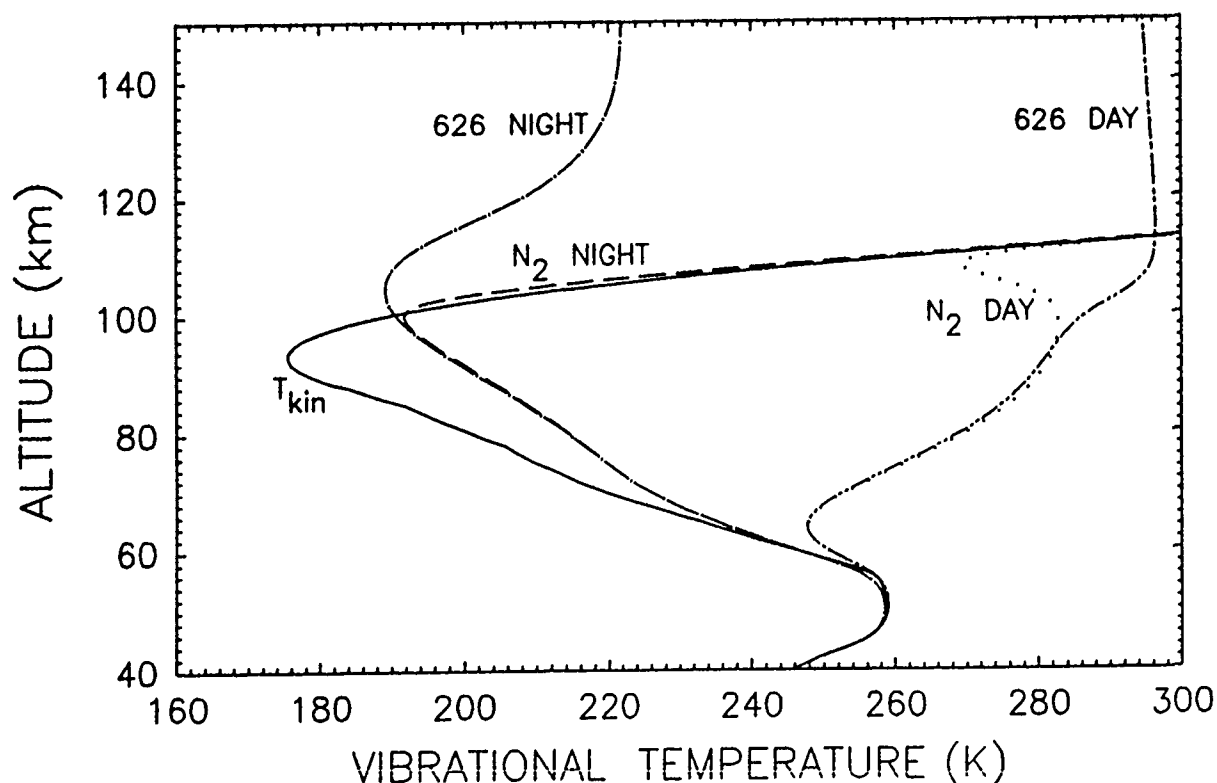
Figure 26. N_2 vibrational temperatures for nighttime conditions, and for daytime conditions with a solar zenith angle of 78^0. The kinetic temperature is shown for purposes of comparison, as are the night and day $CO_2(00011)$ vibrational temperatures of the 626 isotope.

and CO_2 states are very closely coupled for both day and night conditions. This results from the predominance of the intermolecular V-V process, Eq.(28), and it allows the radiative transfer in the CO_2 bands to manipulate the N_2 vibrational populations as well as the CO_2 populations. At the higher altitudes the N_2 vibrational temperatures are practically the same as the kinetic temperature. This in turn reflects the importance of

00011 STATE DAYTIME
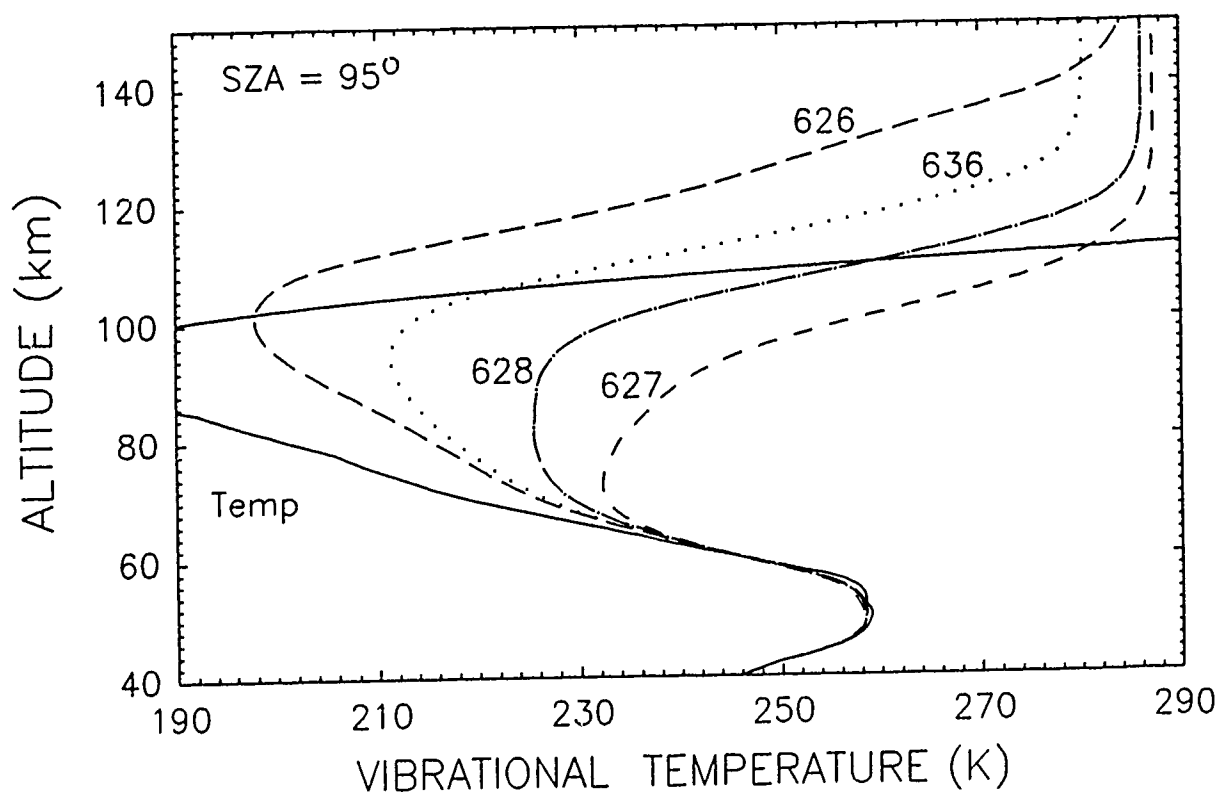
Figure 27. Vibrational temperatures for the 00011 state for four CO_2 isotopes, using a solar zenith angle of 95°.

the thermal process whereby oxygen atoms directly excite N_2 vibration. It results from the increases in [O] and the kinetic temperature and the coincident decrease in [CO_2], with increasing altitude, above the mesopause. (Note that the strength of the V-T process has a strong positive temperature dependence, while that of the V-V mechanism is weakly negative.)

Figure 27 gives the 00011 vibrational temperatures for a solar zenith angle of 95^0. For cases like this, the significance of solar flux passing through the lower altitude regions is illustrated by the fact that below 100 km these curves more nearly resemble the nighttime curves of Figure 24 than the daytime curves of Figure 25, and also by the fact that even at an altitude of 150 km the 626 vibrational temperature is still increasing.

Figure 28 shows the vibrational temperatures for the $CO_2(01111)$ state for the 626 and 636 isotopes, for daytime conditions with a solar zenith angle of 78^0. The general shape of the curves, which is similar to that of $N_2(v=1)$ in the mesosphere, reveals the influence of the V-V transfer; the difference between the 626 and 636 curves shows that the solar pumping is also a significant factor.

Figures 29 and 30 show the vibrational temperatures of some of the important states lying near 3600 cm^{-1} and 5000 cm^{-1}, respectively. These vibrational temperatures were calculated using the procedures outlined earlier by *Sharma and Wintersteiner (1985)*.

It is necessary to make the observation that for low Sun conditions, and particularly for conditions with the solar zenith angle greater than 90^0, lateral variations in the solar flux absorption caused by variations in the solar zenith angle are greater than for "high Sun" cases. A one-dimensional model such as we have implemented cannot account for these variations, so the effect of net horizontal radiative transport, which one might expect across the terminator, cannot be evaluated explicitly. We think that the vibrational temperatures calculated for any one specific location—that is, a vertical profile corresponding to a single solar zenith angle—will not be greatly in error on this account, because throughout the mesosphere the mean free path of 4.3 μm photons is much less than the horizontal distances along which significant changes in solar elevation occur. However, the variations that occur along the horizontal extent of the viewing paths could result in profiles that would be different for different locations. We have not engaged in the laborious task of calculating different profiles for different elements of all the viewing paths, however, in our simulation of the SPIRE limb radiance.

01111 STATE DAYTIME
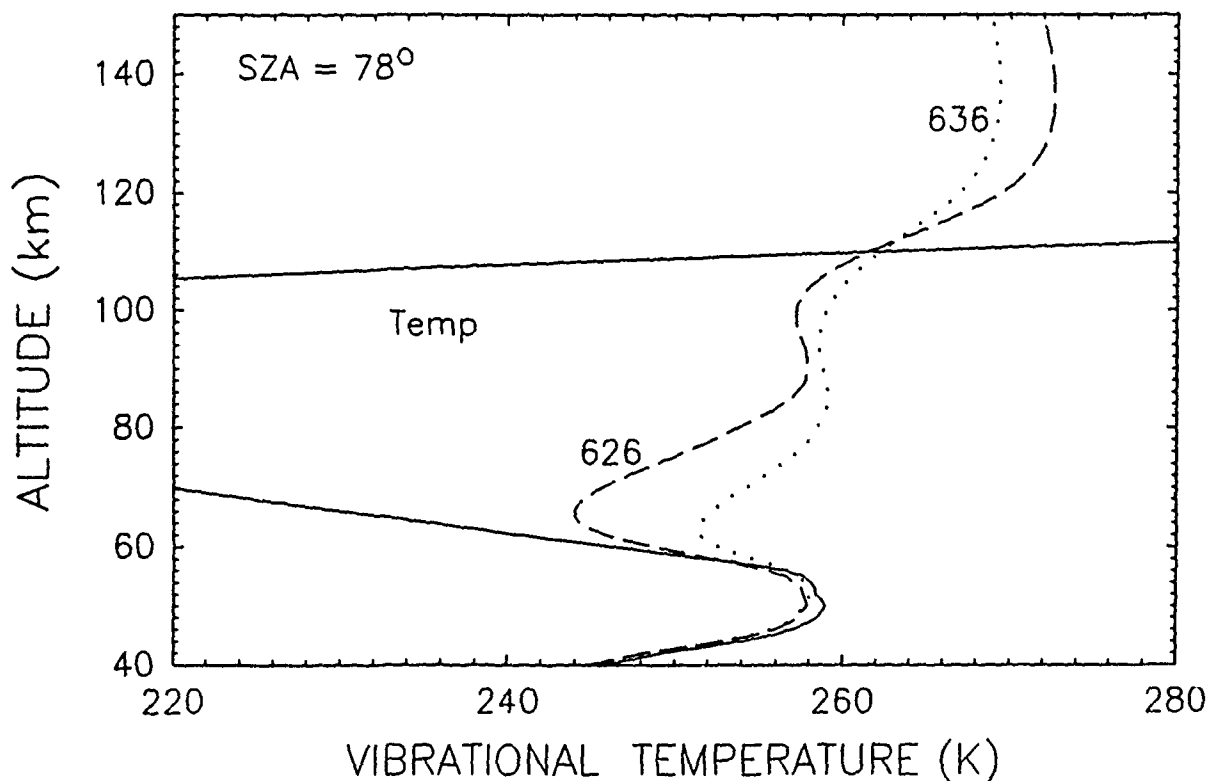
Figure 28. $CO_2(01111)$ vibrational temperatures for daytime conditions with a solar zenith angle of 78^0. The kinetic temperature is shown for purposes of comparison.

3. Limb Radiance

a. Daytime Scans

We modeled the daytime scans by using a single set of vibrational temperature profiles, calculated for a 78^0 solar zenith angle, as input to our line-by-line radiance code, NLTE *(Wintersteiner and Sharma, 1985)*. The results, using all the bands listed in Table 3, are given in Figure 31. They show good agreement with the data at all

GROUP I   (626)
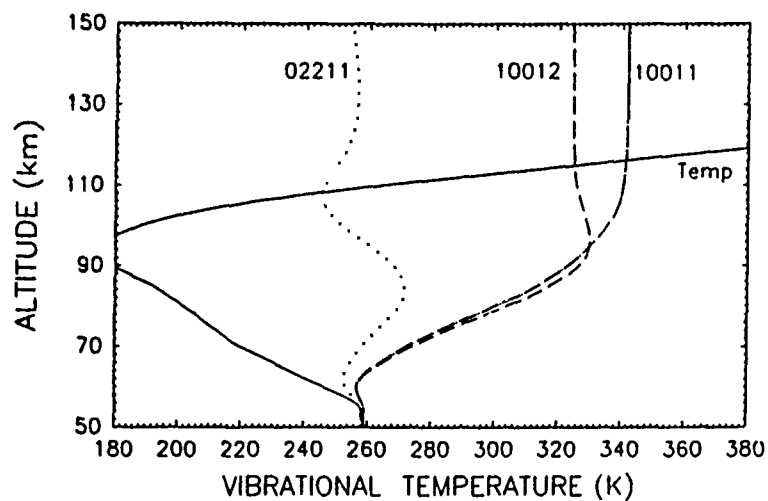
Figure 29. Vibrational temperatures of the states 10011, 10012, and 02211 for daytime conditions with a solar zenith angle of 78°. The kinetic temperature is shown for purposes of comparison.

GROUP III   (626)
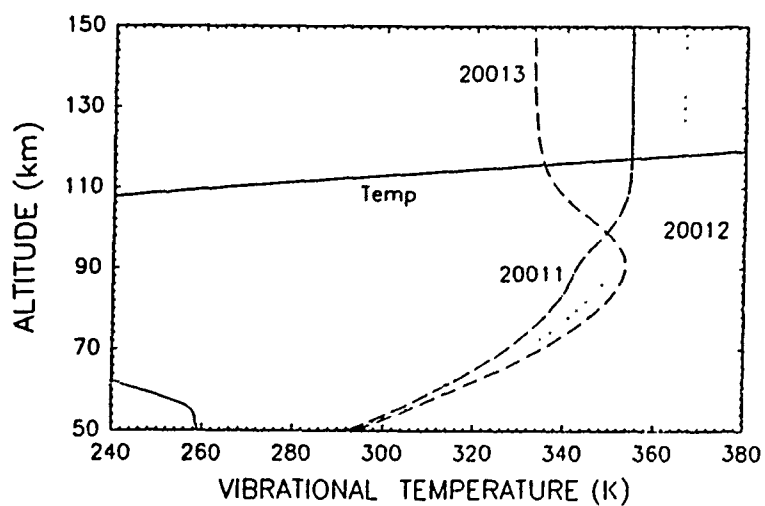
Figure 30. Vibrational temperatures of the states 20011, 20012, and 20013 for daytime conditions with a solar zenith angle of 78°.

DAYTIME CO$_2$ 4.3 μm SPIRE RADIANCE
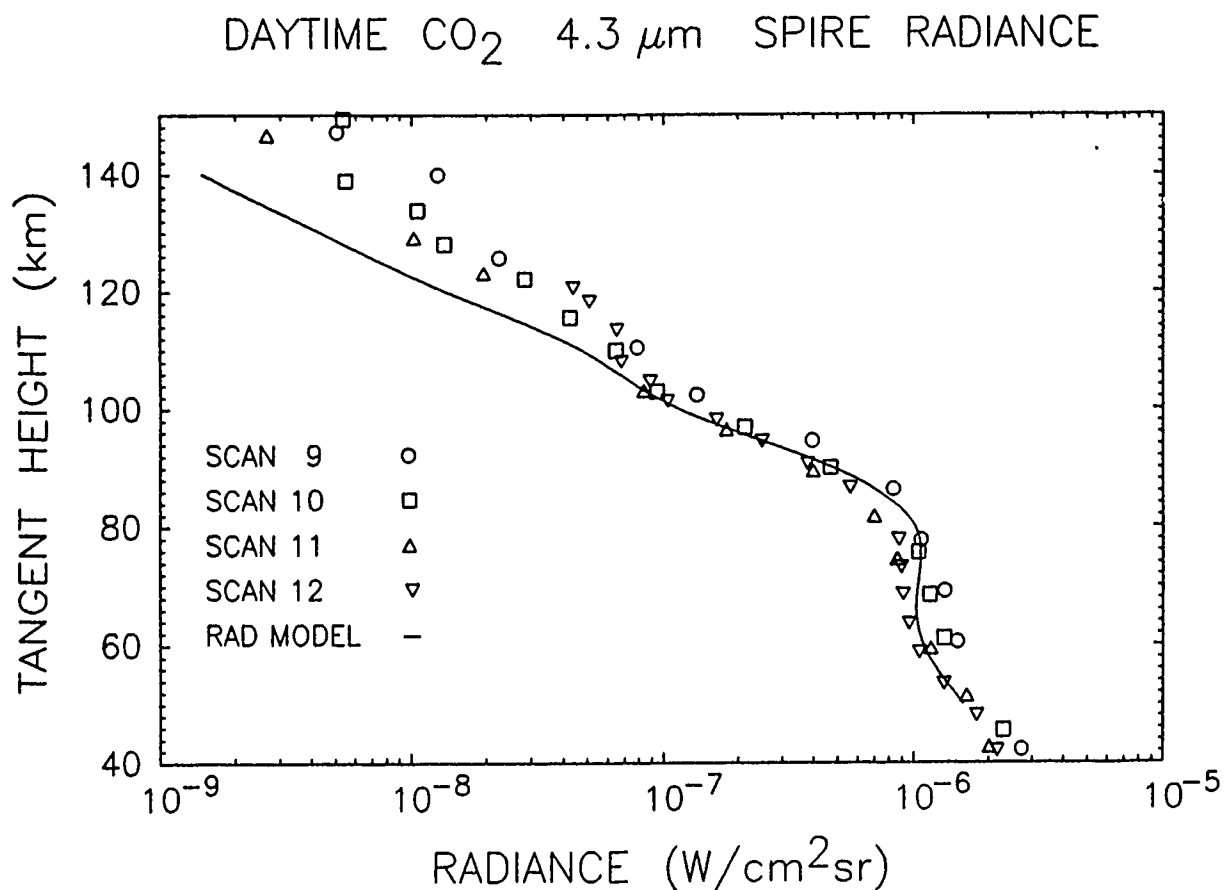
Figure 31. Comparison of the SPIRE limb radiance in the band 4.12-4.49 μm with the daytime model calculation. Data from scans 9-12 only are plotted.

altitudes up to about 110 km, at which point the model begins to underpredict the experimental results slightly. We regard this general agreement as confirmation that our model properly accounts for the processes that are important for exciting $CO_2(\nu_3)$ states in the daytime.

Figure 32 gives the breakdown of the daytime model radiance into contributions from individual bands or groups of bands. The most striking features of this breakdown are (1) the relatively unimportant role played by the major isotope ν_3 fundamental for

DAYTIME CO$_2$ 4.3 μm SPIRE RADIANCE
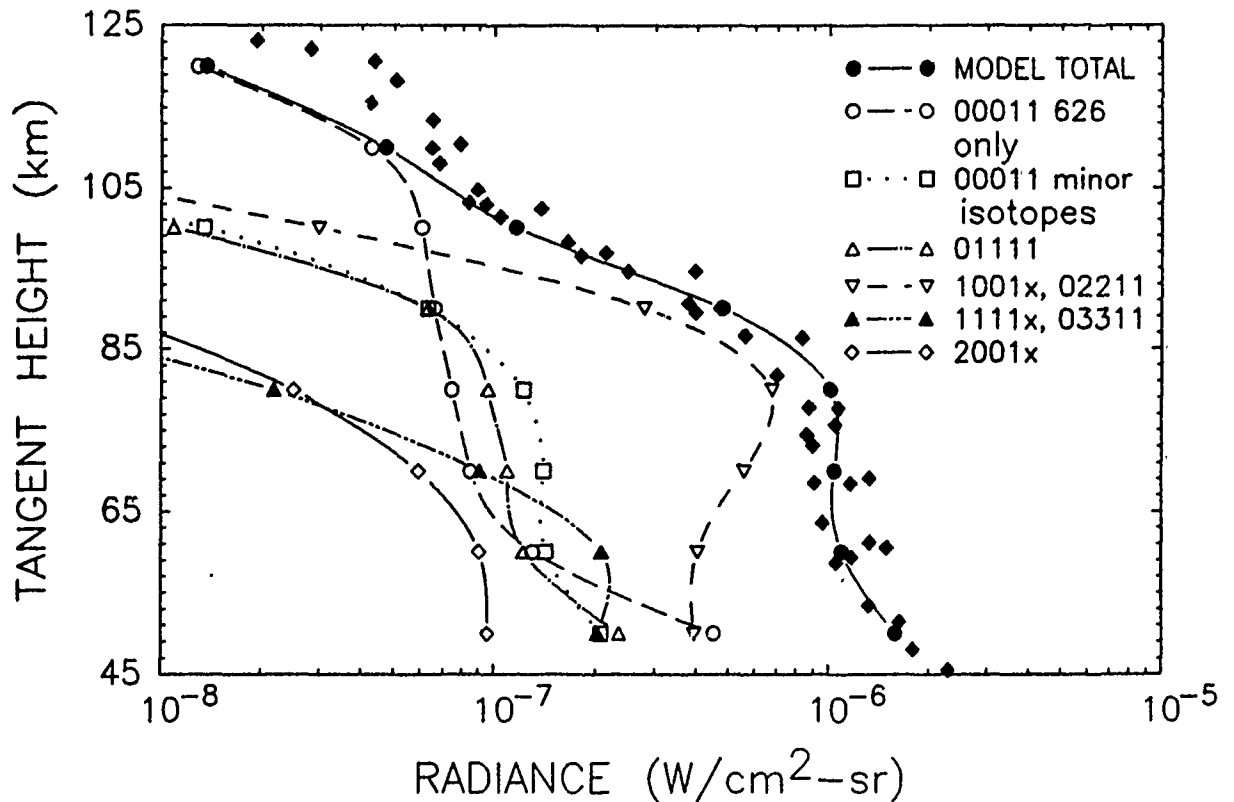
Figure 32. Breakdown of the model radiance into contributions from individual bands, or groups of bands, for the daytime calculation. The bands' contributions are labeled by the upper state of the transition. (See Table 3.)

limb paths through the mesosphere; and (2) the large contribution of the bands originating in the states lying near 3500 cm^{-1}, specifically the 10011-10001 and 10012-10002 bands which for the 80-km tangent path account for 60% of the observed limb radiance. The explanation for this contrast of course lies in the opacity of the atmosphere in these bands, for in terms of absolute numbers of emitters on these paths the ν_3 fundamental is favored by several orders of magnitude. Also, Figure 32 shows that for the lower tangent paths the contributions from all these groups of bands are roughly comparable.

The discrepancy that does appear above 110 km is on the same order of magnitude as the nominal instrumental noise *(W.F. Grieder and C.I. Foley, private communication)*, which would be about 4×10^{-9} watt/cm²-sr in this band, and which was not subtracted from the integrated spectral data as perhaps it should have been. There are other possible explanations, however, including the uncertainty in the CO_2 density at high altitudes.

b. Terminator Scans

We simulated the terminator data using a procedure that was more complicated than that applied to the daylit data, but that is still not capable of completely addressing the problems discussed at the end of Section III.B.1, namely the lateral variations in the conditions characterizing the spectral scans' viewing paths. The basic approach was to model the vibrational temperatures for the dark and sunlit portions of the viewing paths separately. To get the limb radiance we then used a modified version of NLTE that has the capability of dividing the viewing path into segments characterized by either of two separate vibrational temperature profiles. This code, NLTEA, which was designed to model auroral radiance signatures by assuming elevated vibrational temperature profiles for the dosing region and normal profiles for the ambient background, was set up to use solar-pumped profiles for the portion of the viewing path nearest the sensor and nighttime profiles for the portions that were beyond the effective infrared terminator. To do this, we had to choose some condition that best characterized the sunlit portion of all the scans. We decided that a solar zenith angle of 95^0 was as good a representation of the sunlit portion of many of the viewing paths as we could find, and we calculated the vibrational temperature profiles accordingly. Thus, NLTEA was run using profiles such as are shown in Figure 27 for one portion of the viewing path and profiles like those of Figure 24 for the other. For the calculation discussed below, we chose the location of the terminator to simulate the spectral scans of spatial scan 5, because it represents a middle ground between the extremes of scan 8, where the terminator was farthest from the sensor, and scan 1, where it was closest.

The comparison of the data and the model results is shown in Figure 33. The model underpredicts the data by significant amounts for lines-of-sight with tangent points higher than 60 km. For example, the model is low by a factor of nearly three for 80-km tangent paths. We do not have a satisfactory explanation for this discrepancy, which is well outside the range that could be accounted for by uncertainties in $[CO_2]$.

## 4.3 μm SPIRE RADIANCE, TERMINATOR SCANS
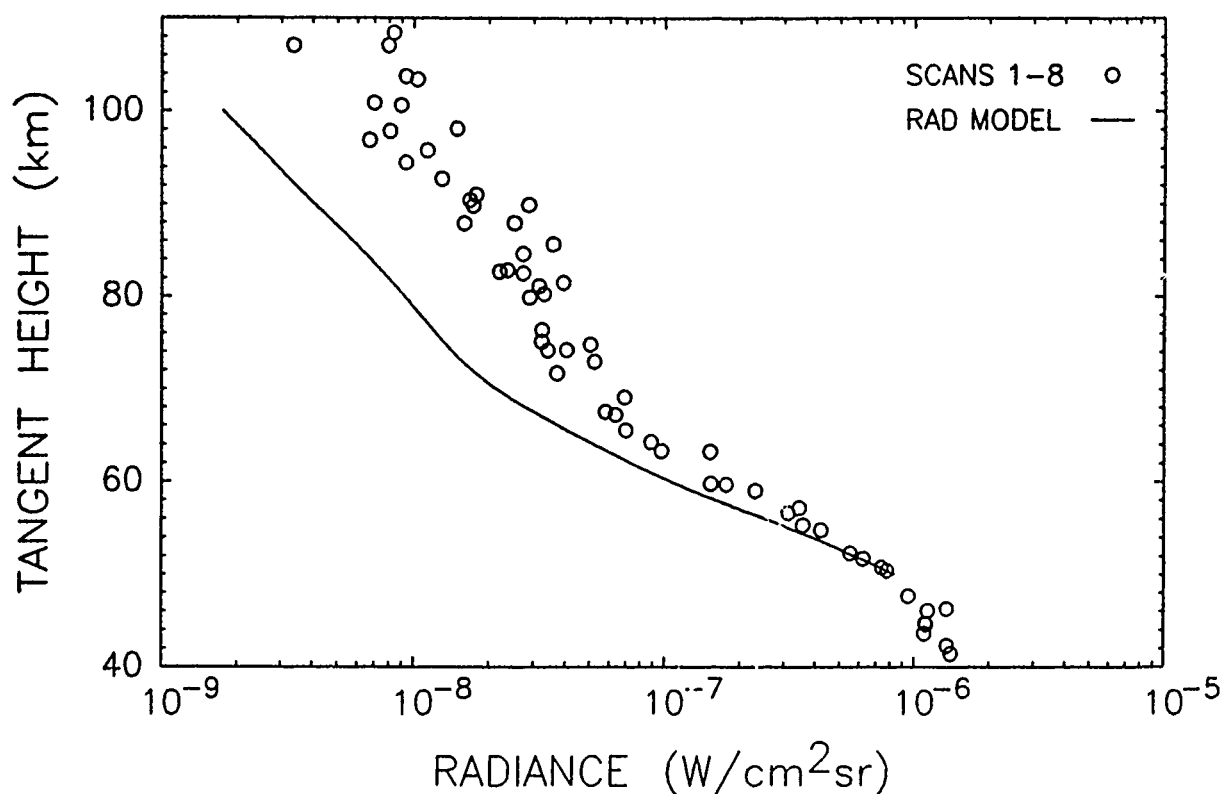
Figure 33. Comparison of the SPIRE limb radiance in the band 4.12-4.49 μm with the terminator model calculation. Data from scans 1-8 only are plotted.

We considered two excitation mechanisms for $CO_2(\nu_3)$ states that were not included in the basic model as possible explanations for this discrepancy. The first of these (*Kumer et al, 1978*) relies on a sequence of reactions beginning with the chemical production of vibrationally-excited OH ($v \leq 9$) from ozone and atomic hydrogen. According to this proposal, OH-N_2 collisions then transfer the vibrational excitation to N_2 molecules, which in turn transfer it to CO_2 according to Eq.(27), raising the CO_2 vibrational

66

temperature and the 4.3 μm emission rates. OH is concentrated in a narrow layer near the mesopause, but radiative transfer in the CO_2 bands would distribute the additional energy throughout a considerable range of altitudes, as would be required to resolve the present difficulty. Inclusion of this mechanism in the calculations does give an increased band radiance along the paths through the mesosphere, but the enhancement is quite small compared to the basic model prediction.

The other possibility we considered involves the quenching of excited $O(^1D)$ atoms by N_2, resulting in increased N_2 vibration and, ultimately, increased CO_2 vibration as well *(Harris and Adams, 1983)*. As with the OH mechanism, the predicted increase in CO_2 excited state populations is too small to resolve the discrepancy appearing in Figure 33.

We have already discussed the problems inherent in simulating the terminator scans with a one-dimensional model. The assumption that the sunlit portion of the lines-of-sight can be adequately approximated by a single vibrational temperature profile appeared to be satisfactory on the basis of some tests that we ran, but more exhaustive analysis might uncover unforeseen problems. We cannot say with certainty that a more detailed radiative-transfer calculation—one that could properly accommodate the lateral variations in solar pumping, for example—would result in enhanced CO_2 populations at just the right places along the lines-of-sight to make up the apparent deficiency in the model, although that remains a possibility. As an alternative, it would be necessary to discover a new excitation mechanism for the $CO_2(\nu_3)$ states, or else justify an increase in the effectiveness of one or more known mechanisms, to properly explain the SPIRE terminator data. It is noteworthy, however, that while such an enhancement would represent a major change in the nighttime calculation, it would be only a minor perturbation in our daytime model, which appears to be successful as it presently stands.

This page intentionally blank.

IV. CO 4.8 μm EMISSION

In addition to the carbon dioxide models, we incorporated the RAD algorithm in a model for predicting 4.8 μm radiance from carbon monoxide. This emission, which derives almost entirely from the (v=1)→(v=0) transition of the major 26 isotope, is interesting for many reasons, including the large seasonal and latitudinal variations that are found throughout the middle atmosphere *(Anderson et al, 1986)*, and also the large day/night differences. Moreover, CO emission is a particularly good subject for line-by-line radiative transfer studies because, compared to other molecules like CO_2, radiative excitation is much more important relative to thermal processes for determining its vibrational populations. That is, with a radiative transition that is not severely self-absorbed except at very low altitudes, and with lines that are so widely spaced that line overlap within the band is of no concern whatsoever, it is possible (and indeed necessary) to extend the radiative-transfer calculation nearly to the Earth's surface, to regions where the richest source of infrared radiation is found. Also, the fact that the vibrational state in question, at 2143 cm^{-1}, is relatively energetic diminishes the effectiveness of thermal processes. This means that the population of the (v=1) state is determined to a great extent by the absorption of upwelling photons, and therefore that the non-LTE region for CO extends to much lower altitudes than for most infrared emitters.

Our main contribution to the CO model was to provide the source code for the vibrational population calculation. We also generated input profiles for the vibrational temperatures of $CO_2(00011)$ and $N_2(v=1)$, which are coupled to CO(v=1), by running the models described in Sections II and III. Dr. Jeremy Winick of the Geophysics Lab evaluated the parameters that were used in the module that solves the steady-state rate equations. He also ran the code to obtain results for a great variety of conditions. These results have been presented in preliminary form *(Winick et al, 1990)* and a detailed publication is in preparation. Since we were not directly responsible for generating these results, however, we do not present them here. Rather, we give a brief outline of the physical processes that have been incorporated in the model.

As we stated earlier, radiative processes are very important throughout the entire altitude range we studied—that is, from the troposphere to the lower thermosphere. They dominate production and loss terms in the steady-state rate equations for [CO(v=1)] everywhere above the stratopause. In addition, daytime calculations are strongly influenced by the absorption of solar flux, which reaches much farther down into the atmosphere in the CO band than in the CO_2 bands discussed in Section III.

Several collision processes are included in the CO model. These are listed in Table 5. Direct thermal excitation of CO vibration by N_2, O_2, and O turns out to be relatively unimportant; due to the large exothermicity the V-T processes are slow *(Taylor, 1974)*. Intermolecular V-V processes, involving the exchange of vibrational quanta with N_2 and CO_2 asymmetric stretch, are quite important at the lower altitudes. These processes are analogous to the near-resonant V-V intermolecular exchange that so strongly couples $CO_2(00011)$ and $N_2(v=1)$ states. However the energy mismatch, only 18 cm^{-1} for N_2-CO_2, is an order of magnitude greater for CO-N_2 and CO-CO_2. The CO-N_2 reaction has a rate constant on the order of $5\text{-}6 \times 10^{-15}$ cm^3/mol-s in the forward direction *(Allen and Simpson, 1980; Mastrocinque et al, 1976)* while CO-CO_2 is about 30 times faster *(Taylor, 1974)*. Because of the number of collisions involved, however, the N_2 exchange is much more effective in populating CO(v=1), and in fact at altitudes below the stratopause this reaction effectively couples CO vibration to N_2 and therefore brings it close to LTE. The values of the rate constants involved, which are somewhat uncertain, therefore do have some effect on the calculations in the stratosphere. However, the dependence is fairly weak and the overall results are more strongly influenced by differences in other conditions, such as the degree of solar pumping and the stratopause temperatures, than by the likely uncertainties in the rates at which the V-V processes proceed.

The radiative transfer calculations in the CO model provided a means of validating the RAD algorithm in ways that had not been possible previously. The algorithm was originally used and tested as part of the CO_2 models, but these were not extended to the ground because of the predominance of thermal processes in the stratosphere, the opacity of the atmosphere to most of the CO_2 transitions, and the problem of dealing with line overlap. However, the calculation in the CO band worked very well all the way down into the troposphere, even though the extreme pressure-broadened emission and absorption lineshapes, for example, represented a large variation from the parameters for which the routines had been tested.

Implementing the CO daytime model forced us to modify our solar-flux absorption program, SABS *(Sharma and Wintersteiner, 1985; Wintersteiner and Joseph, 1986)* to account for variations in the exoatmospheric solar flux. Throughout the infrared, the insolation at the top of the atmosphere is a very slowly-varying function of wavelength, a near-blackbody function characterized by a brightness temperature somewhat less than 6000 K. However, a high-resolution study of the solar spectrum, conducted as a part of the ATMOS experiment *(Farmer and Norton, 1989)*, demonstrates that molecular absorption lines coinciding with rovibrational transitions of many infrared active species are superposed on the background emission. In the middle of the CO lines.

TABLE 5 a. Reactions included in the CO model. In the third reaction, M stands for N_2 and O_2.

Reaction		Type	Rate Constant	Exo-thermicity (cm^{-1})
$CO(v=0) + N_2(v=1)$	$\rightleftharpoons CO(v=1) + N_2(v=0)$	V-V	k_{11}	186.6
$CO(v=0) + CO_2(00011)$	$\rightleftharpoons CO(v=1) + CO_2(00001)$	V-V	k_{12}	206.9
$CO(v=1) + M$	$\rightleftharpoons CO(v=0) + M$	V-T	k_{13}	2143.3
$CO(v=1) + O$	$\rightleftharpoons CO(v=0) + O$	V-V	k_{14}	2143.3

TABLE 5 b. Rate constants describing the reactions, in the forward direction. Units are $cm^3/mol\text{-}s$.

Symbol	Parameterization	Value at 300 K $(cm^3/mol\text{-}s)$
k_{11}	$8.42 \times 10^{-12} \exp(-48.47/T^{0.33})$	6.0×10^{-15}
k_{12}	$1.56 \times 10^{-11} \exp(-30.12/T^{0.33})$	1.7×10^{-13}
k_{13}	$6.67 \times 10^{-8} \exp(-208.3/T^{0.33})$	2.0×10^{-21}
k_{14}	$9.90 \times 10^{-8} \exp(-118.1/T^{0.33})$	2.2×10^{-15}

which are especially prominent in these spectra, the solar flux can be diminished by as much as 35% compared to its nominal (background) value. The absorption is different for different lines, as well. Since solar pumping is such an important part of the CO model, this could not be ignored.

The modification to SABS was quite simple. Using the ATMOS atlas, we supplemented the normal HITRAN linefile for CO *(Rothman et al, 1987)* by adding a factor representing the coronal transmission of solar radiation in the center of each line, and scaled the exoatmospheric flux accordingly when calculating the absorption for each line. The solar-flux absorption coefficients for each altitude were thus calculated starting with a reduced solar exoatmospheric flux that was different for each line but was

independent of frequency within each line. Having this quantity a constant for each line simplified matters considerably, since it obviated the need for a specific (solar) absorption lineshape to get the impinging irradiance accurately. The reason that this works is that the solar absorption lines are Doppler-broadened to widths that are much greater than the widths of the terrestrial absorption lines. As a result, all the photons exciting CO vibration, even those absorbed in the wings of the Voigt lines, come from very near the center of the solar absorption lines.

V. AURORAL EMISSIONS

Here we discuss two complementary methods that we have developed for the analysis of infrared NO, CO_2, and CO emissions from an aurorally dosed thermospheric region. The first method involves the development and use of a first principles model to predict observed spectral emissions given the conditions of the thermosphere. The model used is the Auroral Atmospheric Radiance Code (AARC), which is able to predict nighttime infrared emissions from $NO(\Delta v=1)$, $NO(\Delta v=2)$, $NO^+(\Delta v=1)$, $NO^+(\Delta v=2)$, and $CO_2(\nu_3)$ initiated by auroral excitation (*Winick et al., 1987*). Comparing these predictions to experimental results provides the opportunity to validate such assumptions of the model as rate constants and molecular densities. Differences between prediction and experimental data provide the opportunity to investigate unexpected phenomena. In the present case, examination of data from a rocket based spectrometer led to the detection and analysis of rotationally hot NO band head emissions.

A second approach taken in data analysis is to dissect the experimental data, separating the emissions into the various components. The individual band intensities in turn may be used to infer densities, excitation rates and contributions from different processes. We have developed a series of well-behaved codes which we used to examine infrared emissions in the range 1700 cm^{-1} to 2100 cm^{-1}, decomposing these emissions into components originating from the $NO(\Delta v=1, v'=1 - 8)$ bands. From this analysis we have been able to determine the column emission rate from each band and the rotational temperature, which allows us to determine the altitude where the emission originated. These methods were also used to examine CO emissions in the range 2050 cm^{-1} to 2225 cm^{-1}.

In Section A, we discuss the AARC model and the physical processes included in the model for the calculation of NO and CO_2 emissions. In Section B, we describe our method of spectral decomposition, with emphasis placed on the generation of the spectral line positions and strengths used in the fitting routines. In Section C, we describe results from application of the two methods of analysis described in Sections A and B to experimental data observed by the rocket-borne Field Widened Interferometer (FWI).

A. AARC Model.

AARC is a series of codes which enable the user to calculate aurorally produced emissions from $NO(\Delta v=1, 2)$, $NO^+(\Delta v=1, 2)$, and $CO_2(\nu_3)$ given the auroral energy parameters at the top of the atmosphere. Through continual maintenance and modification, these codes have reached a high degree of accuracy and flexibility, along with a high degree of user-friendliness.

A detailed description of AARC routines as they existed at the time of their initial release to the scientific community is given by *Winick et al. (1987)*. Briefly, AARC is a first principles model using the latest available laboratory and field measurements and theoretical results to predict night-time auroral infrared emission in the spectral range from 1400 cm^{-1} to 5000 cm^{-1}. The codes model the atmosphere from 90 to 160 km, the altitude range where most of the auroral electron energy deposition occurs. Some of the improvements to the model, and enhancements of its capabilities, are described as part of the discussion of the emission processes.

1. Modeling NO $\Delta v=1, 2$ Emissions.

The AARC model begins with a calculation of the electron energy deposition profile using a semi-empirical method due to *Rees (1964)*. The geometry of the observing path is then characterized and divided into small segments. The NO and NO^+ volume emission rates are calculated for each segment and summed over the line-of-sight.

In the quiescent atmosphere, NO is excited vibrationally by collisions with atomic oxygen (*Caledonia and Kennealy, 1982*),

$$NO(v) + O \rightleftarrows NO(v-1) + O, \qquad (29)$$
$$k_{29} = 6.5 \times 10^{-11} \ cm^3 \ sec^{-1}$$
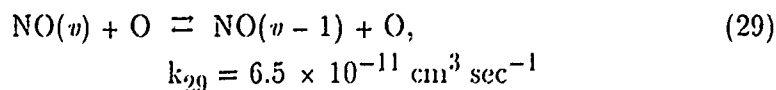
and to a smaller degree by collisions with molecular oxygen,

$$NO(v) + O_2 \rightleftarrows NO(v-1) + O_2, \qquad (30)$$
$$k_{30} = 3 \times 10^{-14} \ cm^3 \ sec^{-1}.$$
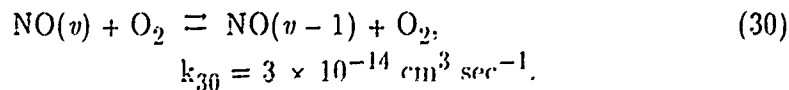
In addition, $NO(v=1)$ is excited by earthshine at a rate of $1.06 \times 10^{-4} \ sec^{-1}$. This rate is independent of altitude, but does vary with season and latitude. In AARC, we follow Caledonia and Kennealy and take a number at the high end of the range.

74

In an auroral region, additional processes lead to NO emissions through the production of $N(^2D)$. $N(^2D)$ then reacts with O_2 to produce NO in vibrational states up to $v \simeq 14$,

$$N(^2D) + O_2 \rightarrow NO(v) + O(^1D, {}^3P), \qquad (31)$$
$$k_{31} = 7.4 \times 10^{-12} (T/300)^{0.5} \text{ cm}^3 \text{ sec}^{-1}.$$

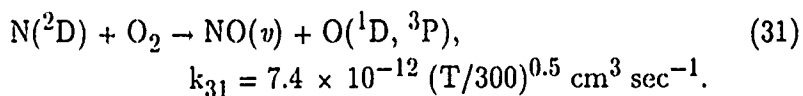Table 6 lists the NO Δv=1, 2 bands included in the AARC model along with their Einstein emission coefficients.

Figure 34 shows background excitation, auroral excitation, and electron-ion pair production rates as a function of altitude. The auroral excitation shown is the sum of all bands excited by a moderate aurora with Gaussian electron energy distribution at the top of the atmosphere,

$$\frac{dF}{dE} = \frac{\Phi}{f} E \ exp\left[-\left(\frac{E - E_o}{\Delta E}\right)^2 \right], \qquad (32)$$

where dF/dE is the electron energy flux per unit of energy, Φ is the total energy flux, f is a normalization factor, E is energy, E_o is the characteristic energy, and ΔE is the energy distribution width. In the case shown in Figure 34, Φ is 15.0 ergs/cm^2-sec, E_o is 11.0 keV, and ΔE is 5.0 keV.

The same program module that calculates NO and NO$^+$ emissions also calculates the rate of $N_2(v=1)$ excitation for the given auroral conditions. This information is stored in a file and used later in the $CO_2(\nu_3)$ calculation.

2. Modeling $CO_2(\nu_3)$ Emissions.

$CO_2(\nu_3)$ (asymmetric stretch) emissions at 4.3 μm present an interesting system because of several complicating factors. These complicating factors include, among other things, time dependence and the presence of significant radiative transfer. The best way to fully treat problems of radiative transfer is by application of the RAD codes described earlier, but in order to account for the time dependence and also in the interest of expediency we treat the radiative excitation and loss processes by a band-model method, following closely the treatment described by *Kumer and James (1974)* and *Kumer (1977b)*. The line-of-sight radiance is, however, calculated by a line-by-line method (*Wintersteiner and Sharma, 1985*).

75

TABLE 6. Einstein emission coefficients for NO bands modeled by AARC.

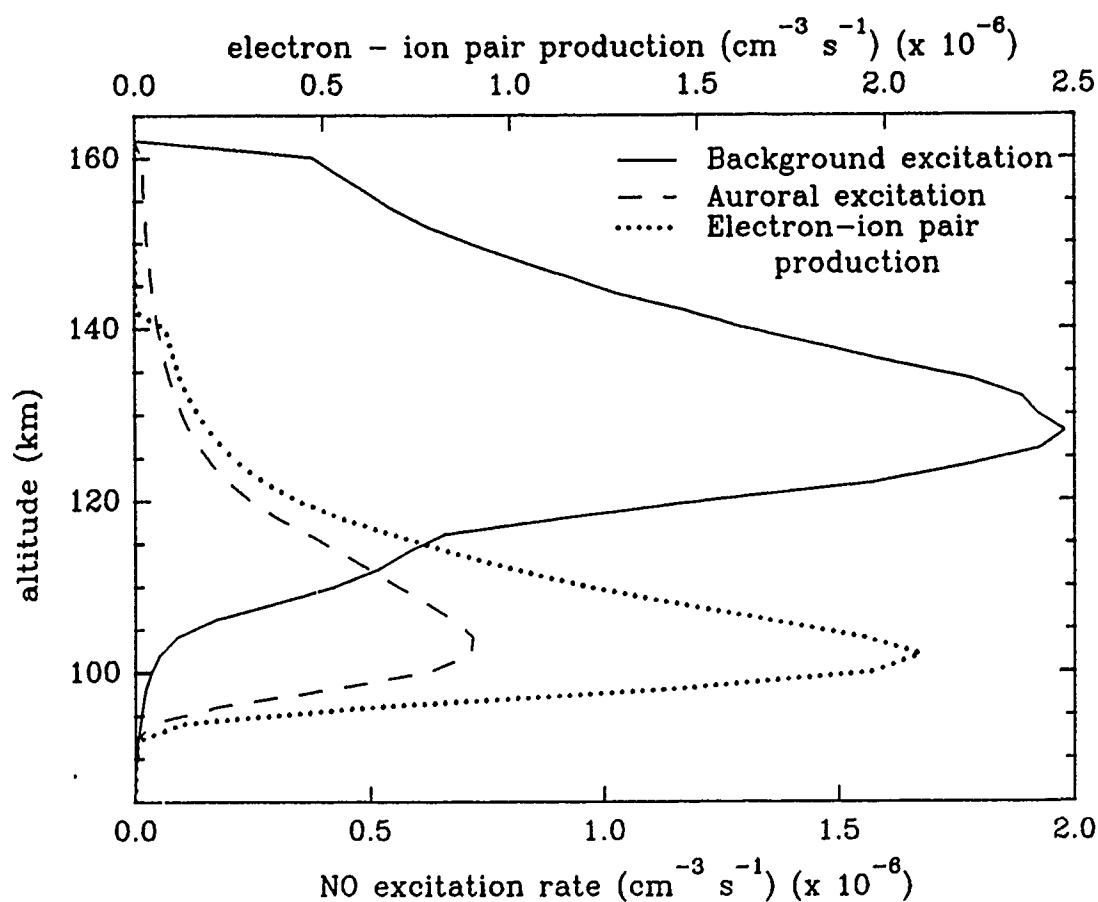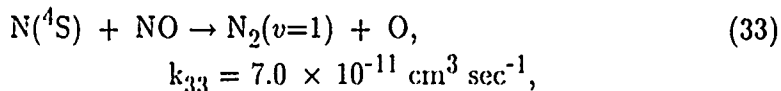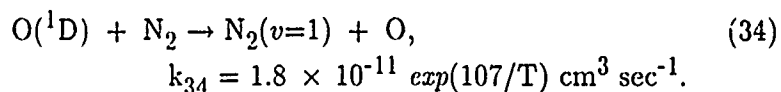|	$\Delta v=1$		$\Delta v=2$	
	Band origin	$A_{v',v'-1}$	Band origin	$A_{v',v'-2}$
v'	(cm^{-1})	(sec^{-1})	(cm^{-1})	(sec^{-1})
1	1875.95	13.16	----	----
2	1847.80	24.92	3723.75	0.46
3	1819.76	35.52	3667.56	1.51
4	1791.78	44.51	3611.54	3.78
5	1763.86	52.37	3555.63	5.98
6	1735.88	59.22	3499.74	8.89
7	1708.00	65.32	3443.89	11.75
8	1680.10	70.13	3388.11	15.25
9	1652.06	73.87	3332.16	19.13
10	1624.07	76.58	3276.12	23.35
11	1596.02	78.26	3220.08	27.99
12	1567.73	78.82	3163.75	33.12

Figure 34. NO excitation rates as a function of altitude. The auroral electron dosing used has a Gaussian energy distribution with $\Phi = 15.0$ erg/cm^2-sec, $E_o = 11.0$ keV and $\Delta E = 5.0$ kev.
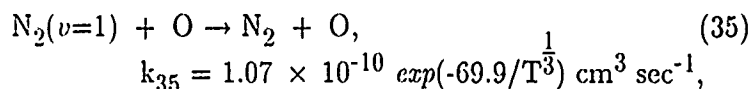
The processes leading up to $CO_2(\nu_3)$ emission begin with production of vibrationally excited $N_2(v=1)$ by collision with low-energy electrons and by the chemical reactions (*Slanger and Black, 1974*)

$$N(^4S) + NO \rightarrow N_2(v=1) + O, \qquad (33)$$
$$k_{33} = 7.0 \times 10^{-11} \text{ cm}^3 \text{ sec}^{-1},$$

and

$$O(^1D) + N_2 \rightarrow N_2(v=1) + O, \qquad (34)$$
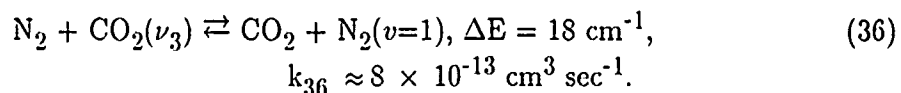$$k_{34} = 1.8 \times 10^{-11} \; exp(107/T) \text{ cm}^3 \text{ sec}^{-1}.$$

N_2 relaxation through radiation is impeded by the lack of dipole moment. The predominant processes for de-excitation are collision with atomic oxygen,

$$N_2(v=1) + O \rightarrow N_2 + O, \qquad (35)$$
$$k_{35} = 1.07 \times 10^{-10} \; exp(-69.9/T^{\frac{1}{3}}) \text{ cm}^3 \text{ sec}^{-1},$$

and the near resonant transfer to $CO_2(\nu_3)$,

$$N_2 + CO_2(\nu_3) \rightleftarrows CO_2 + N_2(v=1), \Delta E = 18 \text{ cm}^{-1}, \qquad (36)$$
$$k_{36} \approx 8 \times 10^{-13} \text{ cm}^3 \text{ sec}^{-1}.$$

Because these processes are relatively slow at auroral altitudes, $N_2(v=1)$ can have lifetimes exceeding 10^3 sec. For this reason, $N_2(v=1)$ densities and $CO_2(\nu_3)$ emissions increase under conditions of steady auroral dosing and persist after auroral dosing has ended. Figure 35 shows the CO_2 volume emission rates as calculated by the AARC model continuing to increase after 900 seconds of steady state auroral dosing. Any calculation of $CO_2(\nu_3)$ emissions necessarily must be time-dependent, and take into account auroral dosing history.

Further complications arise because $CO_2(\nu_3)$ emission lines are optically thick at altitudes well up into the auroral region, causing significant radiative transfer to occur from one region to another. In our model, we use the procedure of *Kumer and James (1974)* which involves using the escape approximation to account for radiative transfer. In essence, the escape approximation represents the probability of photon escape to space. Also, because $CO_2(\nu_3)$ emissions are optically thick, integration of the volume
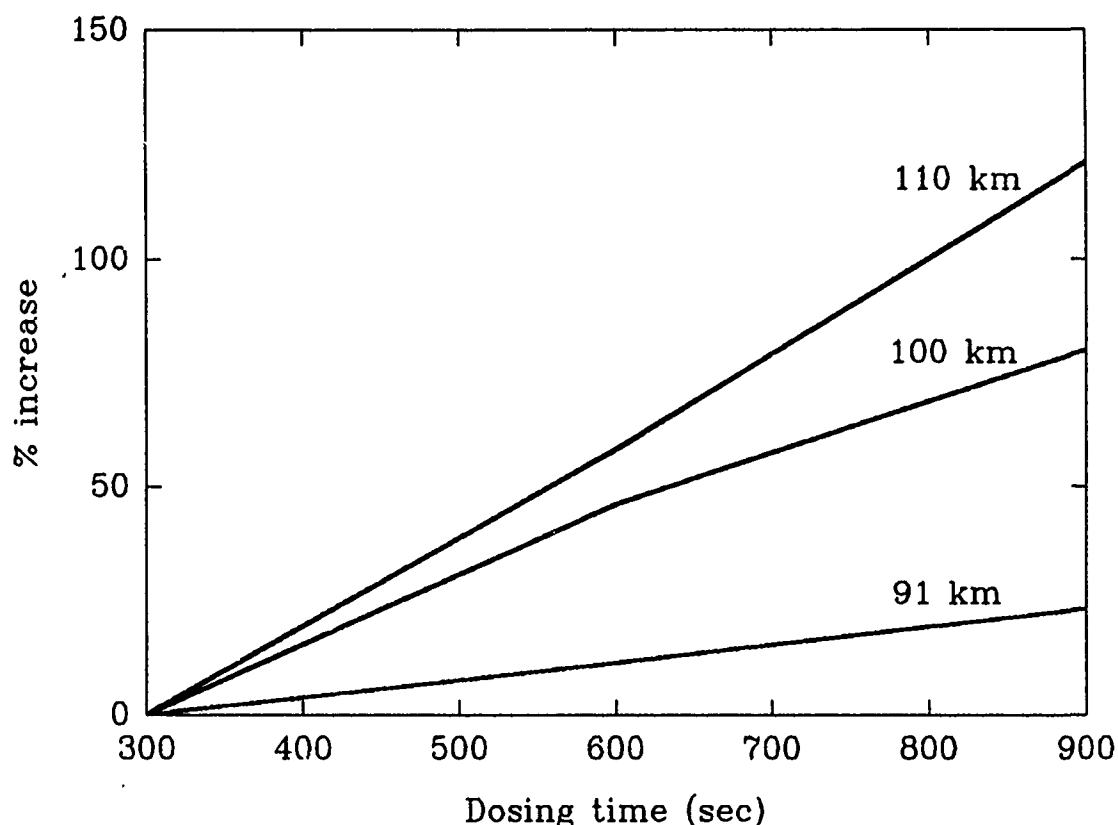
Figure 35. CO_2 volume emissions as a function of time for three altitudes. Each plot shows the percent increase over the level at 300 seconds for that particular altitude.

emission rate over the line-of-sight requires that absorption be included. For that reason, the calculated CO_2 vibrational densities are passed to the NLTE algorithm (*Wintersteiner and Sharma, 1985*) which performs a line-by-line calculation of the 4.3 μm spectrum.

Considerations concerning time-dependence of CO_2 chemistry become more acute in situations where the auroral dosing is fluctuating rapidly. Older versions of the AARC routines modeled auroral dosing with a single time step at one steady-state dosing level. Modifications have been made allowing the AARC model to deal with multiple time steps. Figure 36 shows a fluctuating aurora approximated by a series of step functions. An energy deposition profile is calculated for each step, and the CO_2 calculation is iterated in a consistent manner.
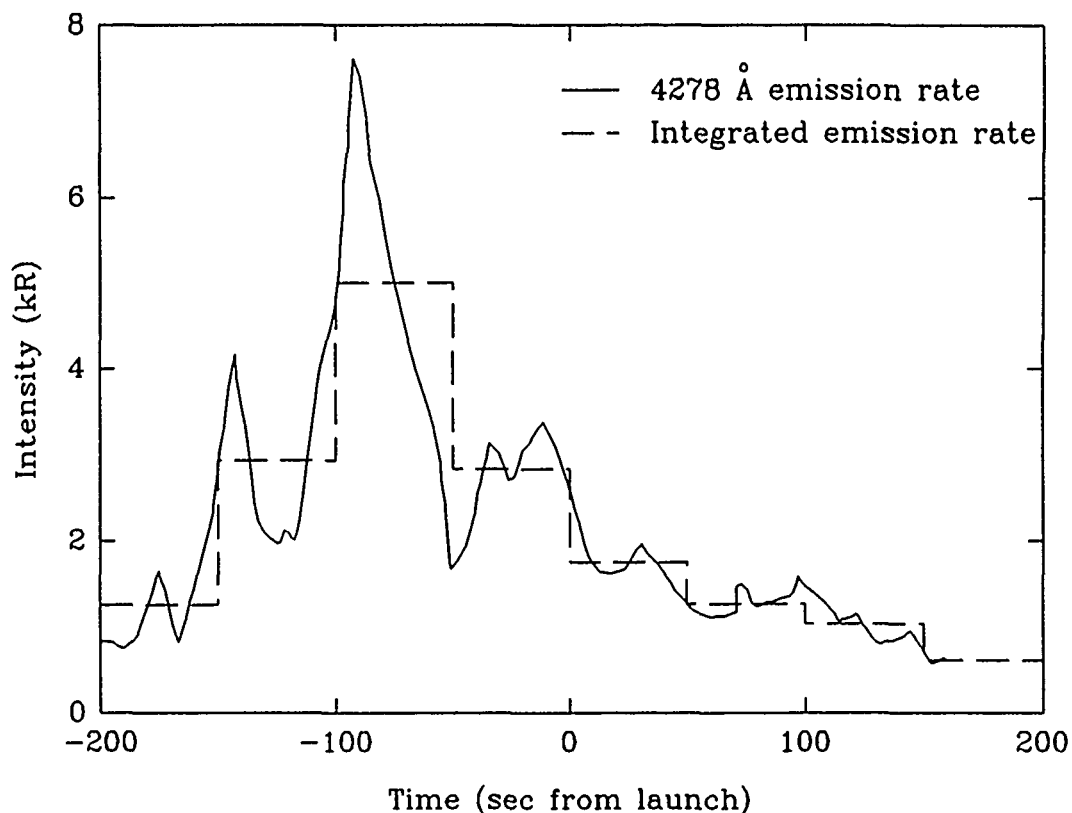
Figure 36. Fluctuating auroral strength as seen by a ground-based 4278 Å photometer during the Field Widened Interferometer launch (*Espy et al., 1988*). The aurora was approximated by the series of step functions shown by the dashed lines.

3. Other AARC Modifications

The next modification to the AARC model involves the characterization of the line-of-sight. The original intent of the AARC routines was to model satellite based limb-look observations, with the observer outside the atmosphere and the line-of-sight passing through with some finite tangent point. The case of FWI rocketborne observations involves essentially zenith-look line-of-sight, with the observer looking up through the atmosphere. To model this situation, the AARC routines had to be modified to include the possibility of upward looking geometry.

The need for an additional modification became apparent during the analysis of nitric oxide spectra observed by the Field Widened Interferometer. As discussed later, using AARC to model this situ on led to results which underestimated the experimental results. The source of this disagreement was found to be the atomic oxygen density profile hard-wired into the code. The solution was to modify AARC,

allowing the code to read alternate density profiles as are produced by the MSIS model *(Hedin, 1987)*. With this modification, the user first runs the MSIS code, inputting the solar-geomagnetic conditions affecting the environment at the time of the observation. The resulting data file is then read and used by the AARC code.

B. Spectral Decomposition.

In this section we discuss our methods of spectral decomposition as applied to two regions of the infrared spectrum: the NO $\Delta v=1$ lines in the range 1700 cm^{-1} to 2050 cm^{-1} and the CO lines in the range 2050 cm^{-1} to 2225 cm^{-1}. We have employed an iterative nonlinear spectral fitting method to determine the strengths and rotational temperatures associated with the emission bands contributing to the observed FWI spectra.

The decomposition method applied here assumes that the emission strengths of the individual rotational lines obey a Maxwell-Boltzmann distribution pattern, i.e., a well defined rotational temperature exists. Though not essential to the analysis, we further assume that the rotational temperature is identical to the kinetic temperature. This is expected since establishment of rotational equilibrium is a fast process.

The method involves generating a series of synthetic spectra assuming a particular rotational temperature and an appropriate instrumental response function. These spectra are used as basis functions in linear least square fits to the observed spectrum. The process is iterated over rotational temperature until an optimum fit, based on the minimization of the squares of the residuals, is obtained.

The basis functions consist of a synthetic spectrum evaluated at the same intervals as the experimental data. The first step is the generation of a stick spectrum consisting of a series of delta functions with positions corresponding to the positions of the individual ro-vibrational lines and relative strengths proportional to the corresponding Einstein emission coefficient multiplied by the probability that the upper state of the transition is occupied,

$$S(J', v'; J'', v'') \propto A_{ul} P(J', v')$$

$$= N A_{ul} g_u \exp\left[-\frac{c_2}{T_R}(E_{v',J'} - E_{v',0})\right], \qquad (37)$$

where A_{ul} is the Einstein emission coefficient for the transition from the upper state. u

$= J'$, v', to the lower state, $l = J''$, v'', c_2 is the second radiation constant, T_R is the rotational temperature, g_u is the degeneracy of the upper state ($= 2J + 1$) and $E_{v,J}$ is the energy of state v, J. The normalization constant, N, is adjusted so that the sum over the entire band is unity.

At this point we have a spectrum, $I(\nu)$, consisting of a series of Dirac delta functions,

$$I(\nu) = \sum S_i \delta(\nu - \nu_i) , \qquad (38)$$

where $S_i = S(J', v'; J'', v' - 1)$, the index i enumerating all lines in a band, and ν_i is the position of that line. This is then convolved with an instrumental response function, $G(\nu)$, to obtain a synthetic spectrum.

$$I'(\nu) = G(\nu) \ast I(\nu) = \int_{-\infty}^{+\infty} d\nu' \, G(\nu - \nu') \, I(\nu'). \qquad (39)$$

Substitution of Eq. (38) into Eq. (39), yields

$$I'(\nu) = \sum_i S_i \, G(\nu - \nu_i). \qquad (40)$$

In the case of the Field Widened Interferometer, the instrumental response function used is a Hamming function,

$$G(\delta\nu) = \frac{1}{\sigma_s}\left\{ c_0 sinc\left(\frac{\delta\nu}{\sigma_s}\right) + c_1\left[sinc\left(\frac{\delta\nu - \sigma_s}{\sigma_s}\right) + sinc\left(\frac{\delta\nu + \sigma_s}{\sigma_s}\right) \right]\right\}, \qquad (41)$$

where $\delta\nu = \nu - \nu_o$, ν_o is the position of line center, σ_s is given by

$$\sigma_s = \frac{\pi\Delta}{2X_o} , \qquad (42)$$

where Δ is the Full-Width-at-Half-Maximum (FWHM), $X_o = 1.8955$ and the sinc function is defined as

$$sinc(x) = \frac{sin(\pi x)}{\pi x} . \qquad (43)$$

In Eq. (41), $c_0 = 0.290713$ and $c_1 = 0.053089$. The FWHM used in the analysis of the FWI NO data was 1.632 cm^{-1}. In the case of CO, two data sets were examined, a high

resolution set with FWHM equal to 1.65 cm^{-1} and a lower resolution set with FWHM equal to 13.21 cm^{-1}.

The basis functions generated by Eq. (40), along with other functions included to compensate for baseline shifts, are used in a linear fit to the experimental data. In the discussion of our linear fitting methods that follows, upper case characters indicate matrices, lower case Latin characters indicate vectors, and lower case Greek characters indicate scalars.

Given a set of spectral data consisting of m ordered pairs of data x_i, y_i where x_i is wavenumber in cm^{-1} and y_i is intensity of the infrared emissions in photons/(cm^2-sec-sr-cm^{-1}), we wish to fit these data with a series of n basis functions, $f_j(x_i)$. Standard linear least-squares analysis involves determining the vector a, such that

$$\|Dr\|_2 \equiv \|D(b - Aa)\|_2 = \min, \tag{44}$$

where b is a column vector of length m with b_i equal to the ith observation,

$$b_i = y_i, \tag{45}$$

D is an m × m nonsingular diagonal matrix given by

$$D_{ii} = \frac{1}{\delta_i}, \tag{46}$$

where δ_i is the standard deviation of the ith data point, and A is an m × n matrix given by

$$A_{ij} = f_j(x_i). \tag{47}$$

Here $\|v\|_2$ indicates the 2-norm of a vector,

$$\|v\|_2 \equiv \sqrt{\sum v_i^2}.$$

Without loss of generality, we can assume that the standard deviations, δ_i, are uniform, in which case Eq. (44) simplifies to

$$\|Aa - b\|_2 = \min. \tag{48}$$

The usual approach to solving Eq. (48) is to set the first derivative equal to zero.

82

Extreme care must be taken since this method will generate a matrix of the form A^TA, which is often nearly singular. (A^T is indicates the transpose of the matrix A.) By far the most stable approach involves Singular Value Decomposition (SVD) of the matrix A (*Press et al., 1986*).

SVD uses the fact (*e. g., Ortega, 1987*) that any matrix, such as A, can always be expressed as the product of three matrices,

$$A = U\Sigma V^T, \tag{49}$$

where U is an m × m matrix, V is an n × n matrix, and both U and V are orthogonal,

$$U^TU = I_m$$

and

$$V^TV = I_n.$$

where I_m and I_n are m and n dimensional unit matrices, respectively. Σ is an m × n matrix with elements given by

$$\Sigma_{ij} = \begin{cases} 0, & i \neq j \\ \sigma_i, & i = j \end{cases} \tag{50}$$

where the σ_i are the singular values of the matrix A with $\sigma_1 \geq ... \sigma_k \geq ... \geq \sigma_n$. Using Eq. (49), we can write (*Kahaner et al., 1989*)

$$\|Aa - b\|_2 = \|U\Sigma V^Ta - b\|_2$$

$$= \|U^T(U\Sigma V^Ta - b)\|_2$$

$$= \|\Sigma V^Ta - U^Tb\|_2 . \tag{51}$$

Setting $U^Tb = d$ and $V^Ta = z$,

$$\|Aa - b\|_2^2 = \|\Sigma z - d\|_2^2$$

$$= (\sigma_1 z_1 - d_1)^2 + ... + (\sigma_n z_n - d_n)^2$$

$$+ d_{n+1}^2 + ... + d_m^2 . \tag{52}$$

The solution to Eq. (48) is, therefore,

$$z_i = \frac{d_i}{\sigma_i},$$

(53)

with the residual,

$$\|Aa - b\|_2 = \sqrt{d_{n+1}^2 + \ldots + d_m^2}.$$

(54)

If any of the σ_i are zero, or nearly zero within the tolerance of the machine, then the problem is degenerate and the solution is not unique. The conventional approach is to set the corresponding z_i to zero. The fact that this algorithm is able to detect degeneracy and deal with it in a well-behaved fashion is one of the advantages of the SVD method.

The linear fitting process was repeated using different rotational temperatures until a best fit was found. Because the basis functions had been normalized to unity, the values of the band strengths were given directly as the values of the coefficients determined by the linear fitting process. Probable errors in the values of band strengths were determined by the linear fitting procedure. Probable errors in the value of temperature were determined by fitting the residuals as a function of trial rotational temperature to a quadratic to determine sensitivity.

1. NO Spectral Data.

The normal source for nitric oxide infrared line positions and strengths would be the HITRAN database *(Rothman et al., 1987)*. This is a comprehensive line file containing information on all species important to atmospheric infrared absorption processes. Because of the emphasis on absorption, the database is truncated at NO rotational levels with J = 35.5 since higher rotational states will be insufficiently populated to contribute to absorption. As will be seen later, high rotational lines play an important role in emission. The standard line file must therefore be augmented. The parameters of *Goldman and Schmidt (1975)* were used to generate the extended NO line file used in this analysis.

The $^2\Pi$ ground state of the NO molecule is intermediate between Hund's case (a), where the electronic motion is strongly coupled to the internuclear axis, and Hund's case (b), where the the electronic spin S is only very weakly coupled. This state is split

by spin-orbit interaction into $^2\Pi_{1/2}$ and $^2\Pi_{3/2}$ components separated by about 120 cm^{-1}. Each of these is in turn split by interaction with neighboring Σ states into pairs of Λ-doublets separated by 10^{-3} to 10^{-2} cm^{-1}. In our treatment, the Λ states have been combined since the splitting will not be visible at the resolution of the experimental data. We assume $\Delta\Omega = 0$, where $\Omega = {}^1/_2, {}^3/_2$ is the electronic angular momentum.

Energy levels are given by

$$T_i(J, v) = G(v) + F_{vi}(J) + T_i^e \tag{55}$$

where $i = 1, 2$ denotes the $^2\Pi_{1/2}$, $^2\Pi_{3/2}$ electronic states respectively, v is the vibrational quantum number, J is the total angular momentum quantum number, the vibrational term value is

$$G(v) = \omega_e(v + \tfrac{1}{2}) - \omega_e x_e(v + \tfrac{1}{2})^2 + \omega_e y_e(v + \tfrac{1}{2})^3 + \omega_e z_e(v + \tfrac{1}{2})^4, \tag{56}$$

the rotational term is

$$F_{vi}(J) = B_v[(J + \tfrac{1}{2})^2 - \Lambda^2] + B_v[L(L + 1) - \Lambda^2] + (-1)^i[B_v(J + \tfrac{1}{2})^2$$
$$+ \tfrac{1}{4}A_v(A_v - 4B_v)\Lambda^2]^{1/2} - D_v[(J + \tfrac{1}{2})^4 - (J + \tfrac{1}{2})^2 + 1], \tag{57}$$

and T_i^e is the electronic term energy. In the case of NO, the electronic orbital angular momentum, L, and the absolute value of the component of L along the internuclear axis, Λ, are equal to 1. The spin-orbit coupling constant, A_v, and the rotational constants B_v and D_v are given by

$$A_v = A_e - \chi_e(v + \tfrac{1}{2}), \tag{58}$$

$$B_v = B_e - \alpha_e(v + \tfrac{1}{2}), \tag{59}$$

and

$$D_v = D_e + \beta_e(v + \tfrac{1}{2}). \tag{60}$$

Table 7. Spectroscopic constants, in cm⁻¹, used to generate NO line positions. *(Goldman and Schmidt, 1975)*

ω_e	1903.937
$\omega_e x_e$	14.044
$\omega_e y_e$	−0.0037
$\omega_e z_e$	5.0×10^{-5}
A_e	123.28
B_e	1.70488
D_e	5.36×10^{-6}
χ_e	0.256
α_e	0.017554
β_e	2.4×10^{-8}

The constants ω_e, $\omega_e x_e$, $\omega_e y_e$, $\omega_e z_e$, A_e, B_e, D_e, χ_e, α_e, and β_e have been determined by Goldman and Schmidt and are given in Table 7.

The Einstein emission coefficient is given by

$$A_{ul} = \frac{8\pi c}{g_u} S(v', v'') \frac{v'}{\bar{v}} \nu^3 S(u \to l), \tag{61}$$

where $u(\Omega, J', v')$ is the upper state, $l(\Omega, J'', v'')$ is the lower state, c is the speed of light, $g_u = 2(2J' + 1)$ is the degeneracy of the upper state, $S(v', v'')$ is the experimental value of the total band intensity, $\bar{v}$ is the band center wavenumber, ν is the wavenumber of the transition and $S(u \to l)$ is the rotational transition probability given by

P Branch:

$$S(u \to l) =$$

$$\frac{1}{J''} \left[a(J', v') \, a(J'', v'') \, (J''^2 - \Omega^2)^{1/2} + b(J', v') \, b(J'', v'') \, (J''^2 - \Omega_l^2)^{1/2} \right]^2 \tag{62a}$$

86

Q Branch:

$$S(u - l) = \frac{2J'' + 1}{J''(J'' + 1)} \left[a(J', v') \, a(J'', v'') \, \Omega + b(J', v') \, b(J'', v'') \, \Omega_l \right]^2 \quad (62b)$$

R branch:

$$S(u - l) =$$

$$\frac{1}{J'} \left[a(J', v') \, a(J'', v'') \, (J'^2 - \Omega^2)^{1/2} + b(J', v') \, b(J'', v'') \, (J'^2 - \Omega_l^2)^{1/2} \right]^2, \quad (62c)$$

where $\Omega_l = \frac{3}{2}$ for the $\frac{1}{2}$ component and $\frac{1}{2}$ for the $\frac{3}{2}$ component. The a and b coefficients are

$$a(J, v) = \left[\frac{X_v - 2 + A_v/B_v}{2 \, X_v} \right]^{1/2} \quad (63a)$$

and

$$b(J, v) = \left[\frac{X_v + 2 - A_v/B_v}{2 \, X_v} \right]^{1/2} \quad (63b)$$

where A_v and B_v are given in Eqs. (58) and (59) and X_v is given by

$$X_v = \left[4(J + 1/2)^2 + (A_v/B_v)(A_v/B_v - 4) \right]. \quad (64)$$

The values of the band intensities are retrieved from the AFGL atmospheric absorption line compilation (*Rothman et al., 1987*) and are given in Table 8.

We have used the formalism of Goldman and Schmidt to generate a line file with an upper bound of $J'' = 120.5$. Our compilation is in absolute agreement with the AFGL database for the range in which the two databases overlap ($J'' \leq 35.5$). The legitimacy of this is at first suspect since for higher angular momentum states, the $^2\Pi$ state will move further toward Hund's case (b), where Σ is no longer a good quantum number. As will be shown later, however, there is good agreement between the generated high angular momentum line positions and the line positions from the FWI data. The Fortrat diagram for the NO(1-0) 1/2 − 1/2 transition, Figure 37, shows the R-branch band head. The Einstein coefficients as a function of wavenumber are shown in Figure 38.

Table 8. Band intensities used to generate NO line intensities. (Derived from AFGL line file.)

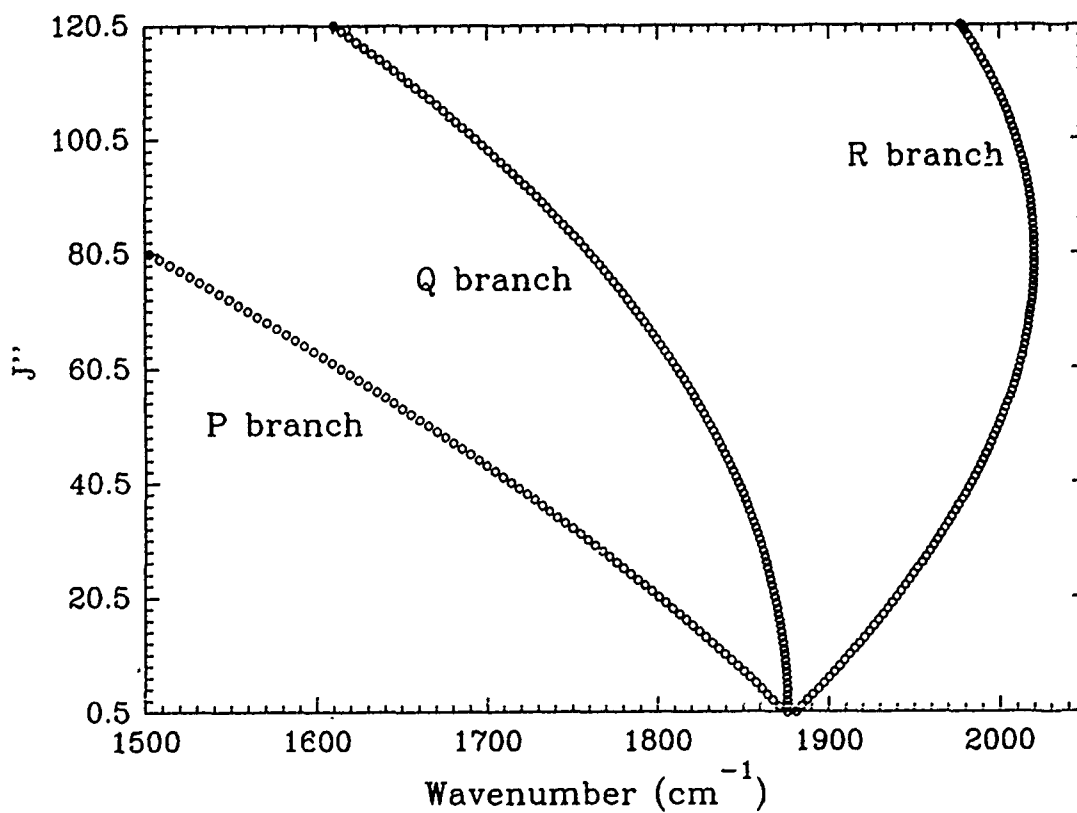| v'	$\frac{4\pi c v'}{\bar{v}} S(v', v' - 1)$
	cm^3/mol-sec
1	2.0077×10^{-9}
2	3.9793×10^{-9}
3	5.9386×10^{-9}
4	7.7976×10^{-9}
5	9.6202×10^{-9}
6	1.1416×10^{-8}
7	1.3223×10^{-8}
8	1.4920×10^{-8}
9	1.6533×10^{-8}
10	1.8045×10^{-8}
11	1.9431×10^{-8}
12	2.0644×10^{-8}

Figure 37. Fortrat diagram for the NO(1-0) $^1/_2 - {}^1/_2$ transition.
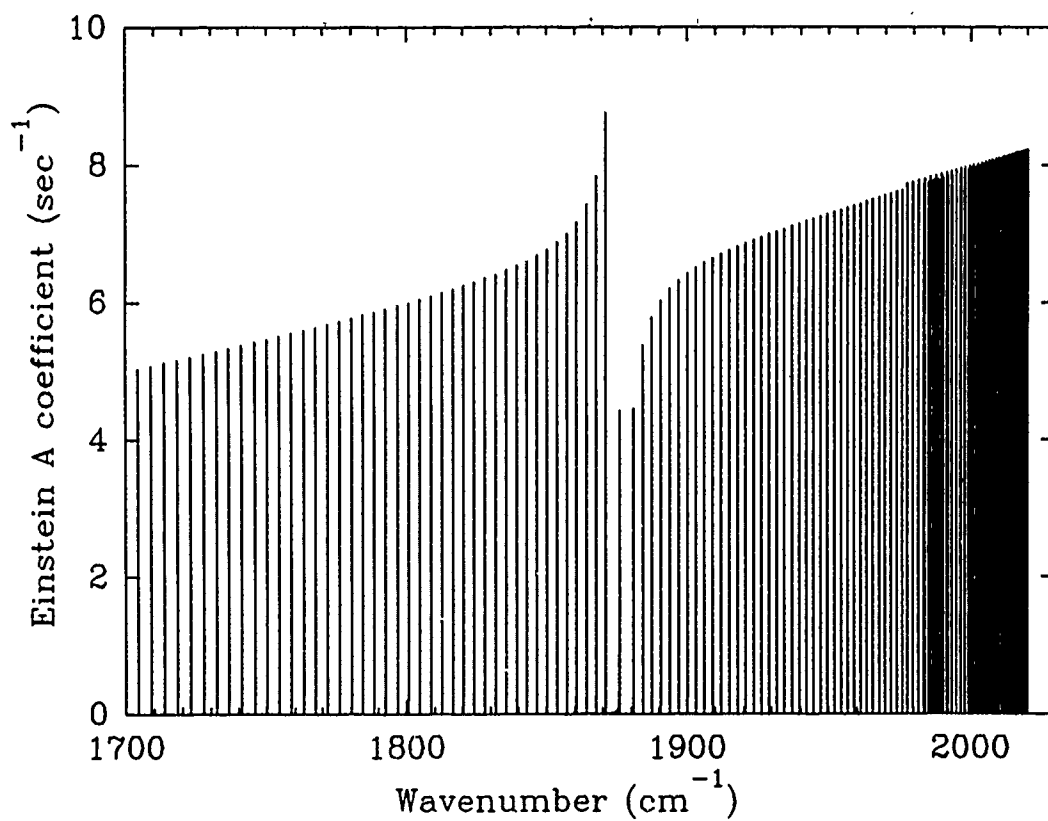
Figure 38. Einstein A coefficients for the NO(1-0) $^1/_2$ – $^1/_2$ transition.

2. CO Spectral Data. A similar method was used to generate the CO line file. The singlet ground state of CO, $^1\Sigma^+$, does, however, lead to simplification. We use the formalism and spectroscopic data of *Huber and Herzberg (1979)* in the calculation of the line positions and strengths.

The ro-vibrational energy levels of the CO molecule are given by (cf., Eq. (55)),

$$T(J. v) = G(v) + F_v(J) + T_e , \tag{65}$$

where the vibrational term $G(v)$ is given by Eq. (56). The rotational term reduces to

$$F_v(J) = B_v J(J + 1) - D_v J^2 (J + 1)^2 , \tag{66}$$

where B_v is given by Eq. (57) and D_v is approximated by

$$D_v \approx D_e . \tag{67}$$

The line radiance (W cm^{-2} sr^{-1}) is given by

$$I(u, l) = \left[\frac{E_{ul}}{hc\Delta G}\right]^4 (J' + J'' + 1) \frac{exp\left[-\left(\frac{hc}{kT}\right) F_{v'}(J')\right]}{Q_R(v')} I_B(v', v''), \tag{68}$$

where E_{ul} is the transition wavenumber, ΔG is the band origin transition wavenumber,

$$\Delta G = G(v') - G(v''), \tag{69}$$

$Q_R(v)$ is the rotational partition function,

$$Q_R(v) = \sum_J (2J + 1) \, exp\left[-\left(\frac{hc}{kT}\right) F_v(J)\right], \tag{70}$$

and I_B is the total band radiance. The spectroscopic constants are given in Table 9. The CO line file was generated with values of J up to J = 30.

The line radiances are convolved with an instrumental response function as discussed in the previous section.

Table 9. Spectroscopic constants, in cm^{-1}, used to generate CO line positions. *(Huber and Herzberg, 1979)*

ω_e	2169.814
$\omega_e x_e$	13.2883
$\omega_e y_e$	0.010151
$\omega_e z_e$	5.74×10^{-5}
B_e	1.93128
D_e	6.1214×10^{-6}
α_e	0.0175
β_e	0.04×10^{-6}

C. Analysis of the FWI Experiment.

In this section we discuss our analysis and modeling of data collected by a rocketborne instrument, the Field Widened Interferometer (FWI). We have analyzed the data collected by this experiment from two points of view. The AARC model was used to predict NO and CO_2 emissions, and our spectral decomposition methods were used to determine NO and CO radiances as seen by the instrument.

A Sergeant sounding rocket was launched from from the Poker Flat Research Range, Alaska (65.1°N, 147.5°W) on 13 April 1983 into an IBC II aurora (*Picard et al., 1987; Espy et al., 1988*). The rocket was equipped with a cryogenically cooled field-compensated Michelson interferometer (*Despain et al., 1971; Haycock and Baker, 1974*) with a spectral range of 1300-4000 cm^{-1}, an (apodized) resolution of 1.6 cm^{-1}, and a noise-equivalent spectral radiance (NESR) of 5.0 × 10^6 photons/cm^2-sr-cm^{-1}. The rocket was also equipped with a four-quadrant 3914 Å photometer and an electron scintillator. In addition, ground based support provided all-sky television monitoring and meridian photometry at 5577 Å, 4278 Å, 6300 Å, and 4861 Å. The instrument took the first interferogram at an altitude of 85 km and continued taking scans at intervals of 1.6 seconds through the apogee of 139 km and on the downward leg. Figure 39 shows the trajectory of the FWI rocket.

Our analysis of the FWI data involved partitioning the observed infrared spectra into three segments corresponding to three different molecular species, NO, CO_2, and CO. AARC was used to model $CO_2(\nu_3)$ emissions in the region 2275 cm^{-1} to 2400 cm^{-1} (*Joseph et al., 1986; Winick et al., 1988*) and NO(Δv=1) emissions in the region 1700 cm^{-1} to 2050 cm^{-1} (*Picard et al., 1987; Joseph et al., 1989*). In addition, spectral decomposition was used to analyze the NO emissions and also the CO emissions in the region 2050 cm^{-1} to 2225 cm^{-1}.

1. NO Δv=1 Emissions.

Of the 139 interferograms taken during the flight, we have been able to reliably analyze 38 for NO emissions (Figure 39, circles). Difficulties with the other scans were often due to very small (0.2 cm^{-1}) shifts in the wavenumber scale. Least squares methods are built upon the assumption that all errors are in the values of the observations, and that the independent variables are known with certainty.

Figure 40 shows the NO region of a typical scan taken at low altitude (88.56 km). The interferogram shows this region to be dominated by the NO(1-0) band with all
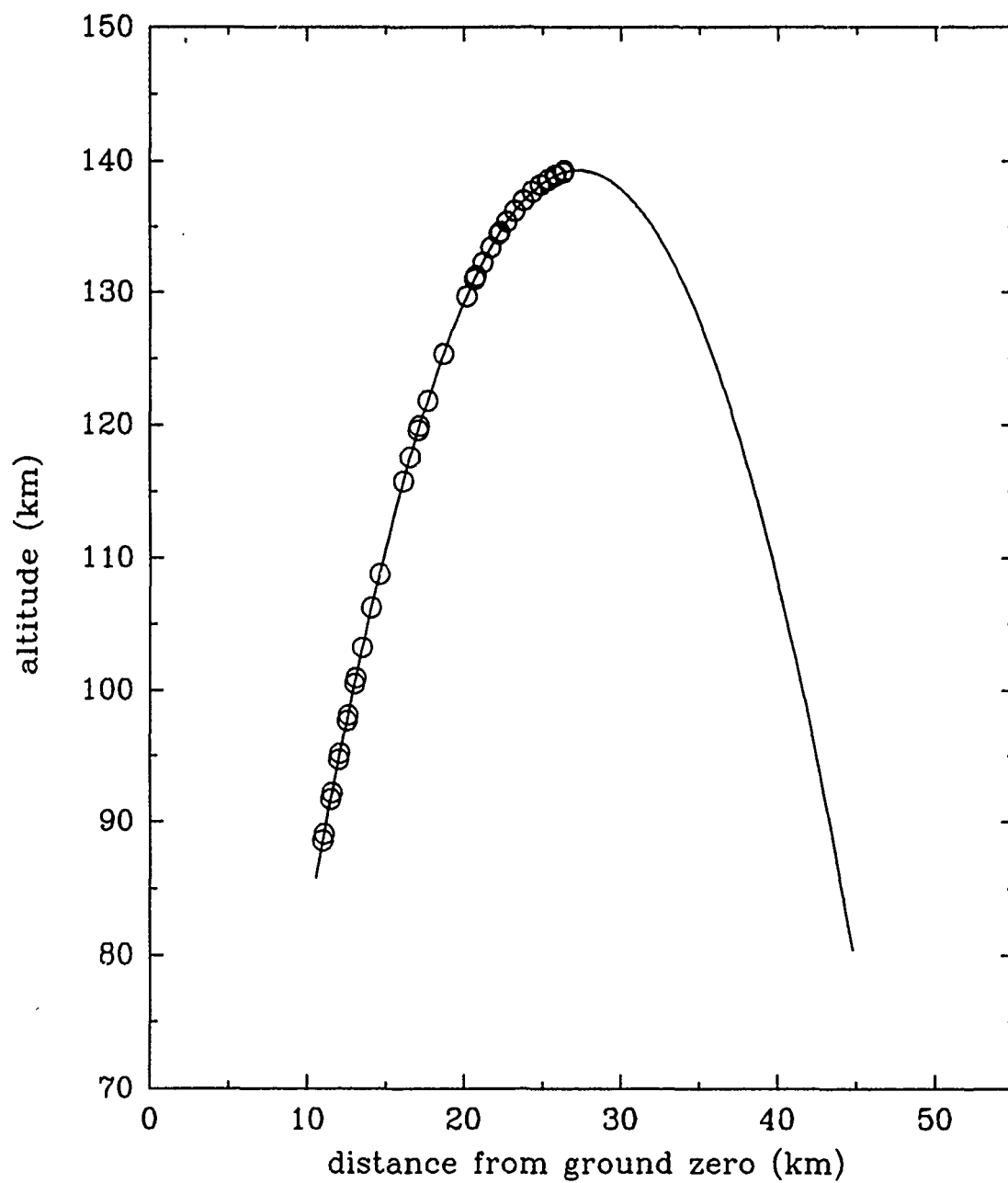
91

Figure 39. Flight path of the FWI experiment. Circles indicate positions of the scans which are included in the NO analysis.
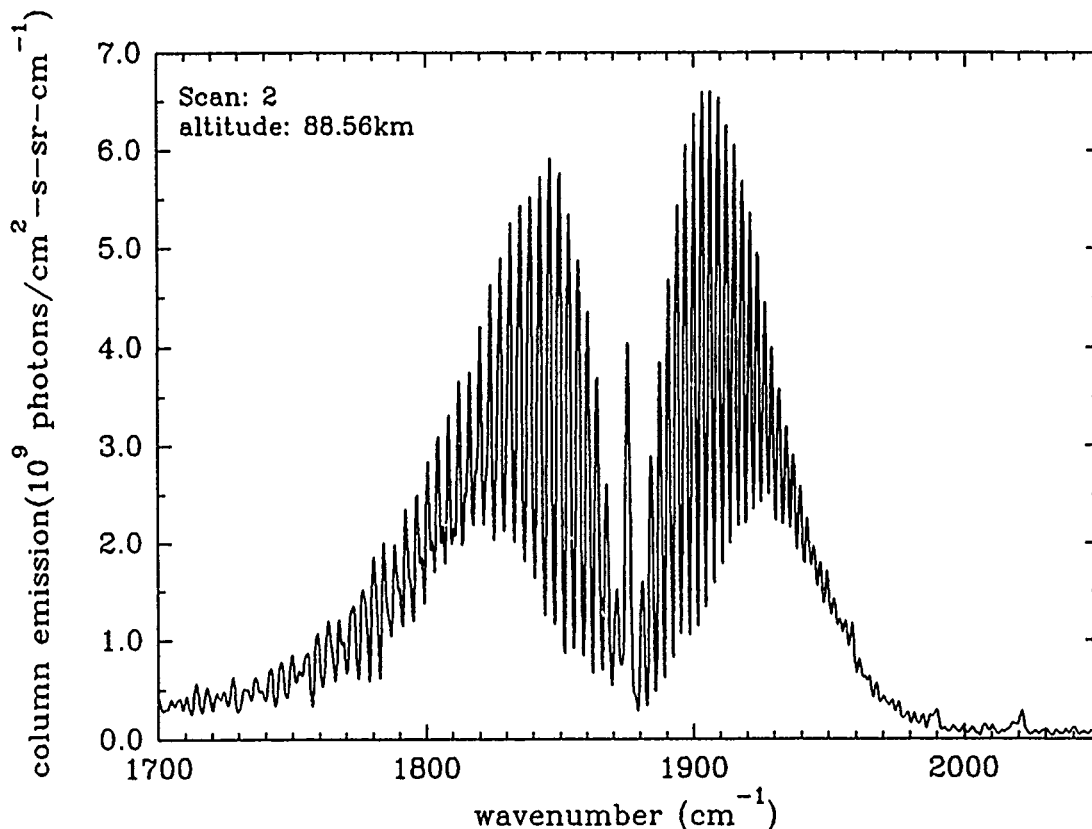
Figure 40. NO infrared emissions as seen in a low-altitude FWI scan (Scan 2, 88.6 km).

three branches, P, Q, and R, clearly seen. Also seen are three small features occurring at around 1960 cm^{-1}, 1990 cm^{-1}, and 2020 cm^{-1}. These are not experimental artifacts since they occur at the same position in all of the low altitude scans up to 105 km. Figure 41 shows them more clearly. The top portion of Figure 41 is the residual after removing the contributions from the background and auroral bands (the first nine bands of Table 10). The bottom portion shows synthetic spectra simulating the NO band heads for vibrational states $v' = 1, 2, 3$. The basis functions corresponding to the band heads were generated assuming uniform occupancy of rotational states $J' = 70.5 - 95.5$, and zero state occupancy outside of this region. Only emission in the R-branch, where the band head occurs, is included. The alignment in wavenumber is excellent, identifying these features as NO band heads. The close coincidence also validates use of the parameters of Goldman and Schmidt up to rotational states $J \simeq 100$. We have included these band heads in our analysis of the FWI data. Since these emissions are significant only in a small spectral region near the band head, no determination of rotational temperature is possible, nor is a rotational temperature expected to be defined since processes accounting for these band head emissions are likely to be very fast, prohibiting the establishment of rotational equilibrium.

93
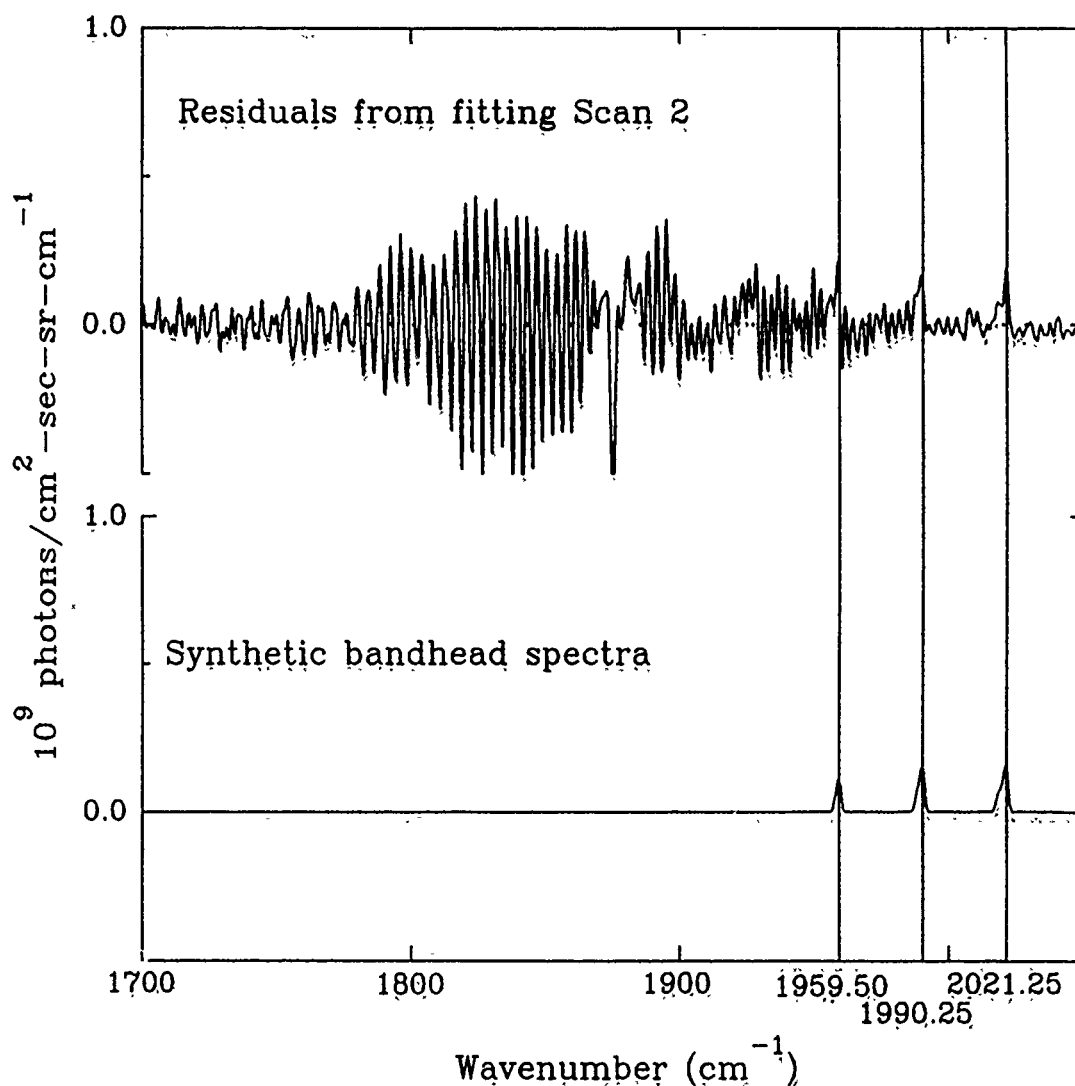
Figure 41. Top is the residual plot from Scan 2 showing the band heads. Bottom is the synthetic band head spectra for NO bands v′ = 1, 2, 3.

These band heads require a high degree of rotational excitation, on the order of 2-3 eV above the energy required to excite the molecule vibrationally. Since this is greater than the energy available from the reaction of $N(^2D)$ with O_2, other reactions must be involved. *Rawlins et al (1989)*, having observed the presence of NO band heads in laboratory data up to vibrational level $v = 8$, point out that a possible source of the high rotational states is the reaction

$$N(^2P) + O_2 \rightarrow NO(v) + O \qquad (71)$$

$$\Delta H = -4.95 \text{ eV}.$$

94

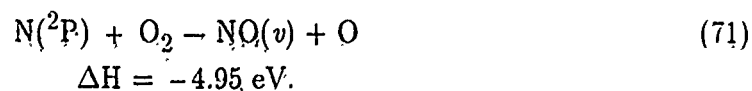Table 10. NO band radiances (photons/cm^2-sec-sr) from analysis of FWI Scan 2.

Scan: 2   USU filename: RBI. 2   date of scan: Apr 13 1983   time of scan: 9: 7:44:951
altitude at start of scan: 87.2   altitude at end of scan: 88.8   average altitude: 88.56

	Band	Band radiance	Source
1	$1 \to 0$	2.779×10^{11}	Background
2	$1 \to 0$	1.570×10^{11}	Aurora
3	$2 \to 1$	1.816×10^{10}	Aurora
4	$3 \to 2$	1.556×10^{10}	Aurora
5	$4 \to 3$	1.564×10^{10}	Aurora
6	$5 \to 4$	1.031×10^{10}	Aurora
7	$6 \to 5$	7.715×10^{9}	Aurora
8	$7 \to 6$	2.928×10^{9}	Aurora
9	$8 \to 7$	6.300×10^{9}	Aurora
11	$1 \to 0$	5.425×10^{8}	Band head
12	$2 \to 1$	4.291×10^{8}	Band head
13	$3 \to 2$	2.530×10^{8}	Band head

Other possible sources of the high-J NO states include collisional excitation from proton aurora and collisional quenching from high vibrational NO states (R. D. Sharma, private communication).

Using iterative nonlinear decomposition we have determined the magnitude of the NO fundamental emissions (Figure 42, circles), the magnitude of the NO hot band emissions (Figure 43, circles), the corresponding rotational temperatures (Figure 44), and the magnitude of the band head emissions (Figure 45), all as functions of altitude.

Also shown in Figures 42 and 43 are emissions predicted by the AARC model using atmospheric conditions at the time of the launch. Initial attempts to model the fundamental band emission underestimated the FWI data by approximately 50%. Examination of the problem indicated that an underestimate of the atomic oxygen density was the source of the discrepancy.

MSIS-86 (Hedin, 1987) was used to generate an atomic oxygen density profile appropriate to the solar-geophysical conditions (Solar-Geophysical Data, 1983) at the time of the FWI launch. This is shown in Figure 46a along with the standard oxygen profile that is hard-wired into the AARC code. Figure 46b shows the MSIS temperature profile used.

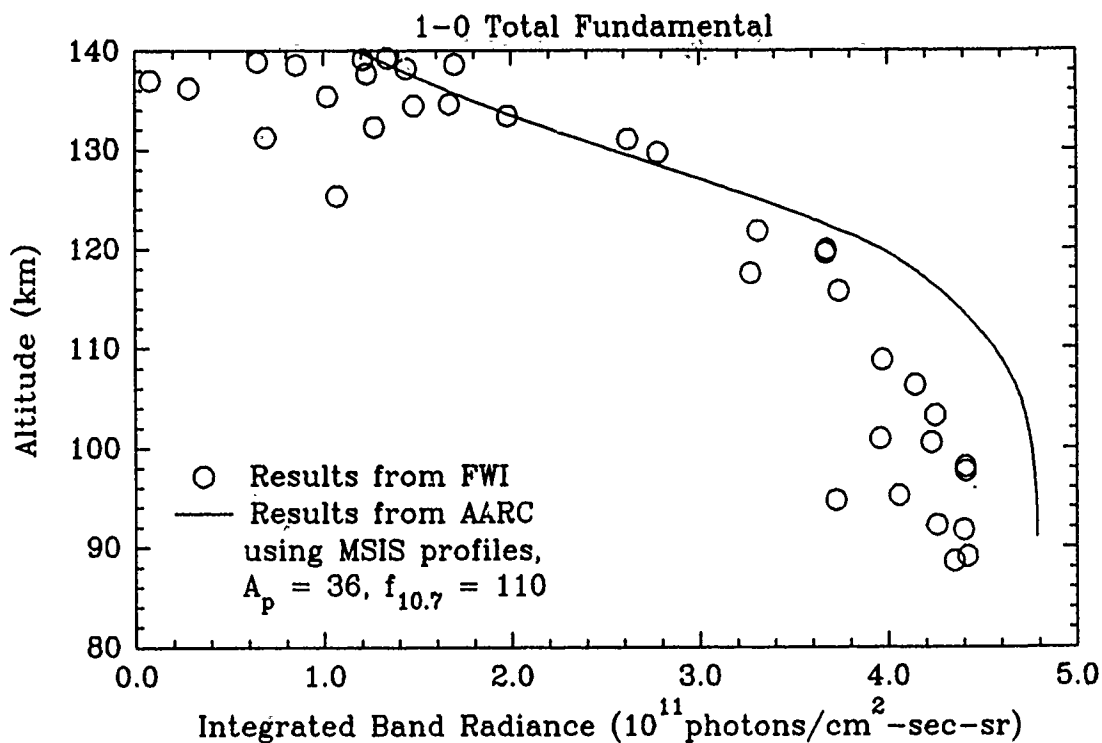**Figure 42.** NO fundamental emissions. Circles are the results from analyzing FWI data; the solid line is the result from AARC. In both cases, the emissions are the sum of background and auroral sources.
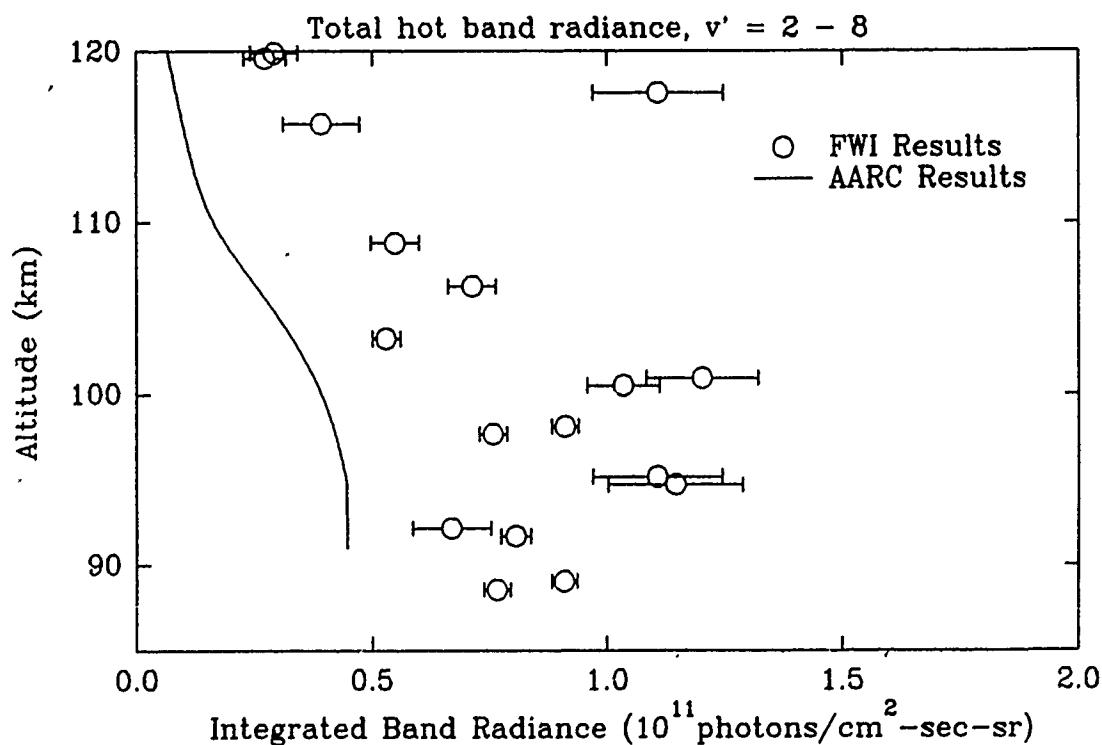

Figure 43. Hot band emissions. Circles represent FWI results; the solid line is the result from AARC. In both cases, the sum of hot bands $v' = 2 - 8$ is shown.
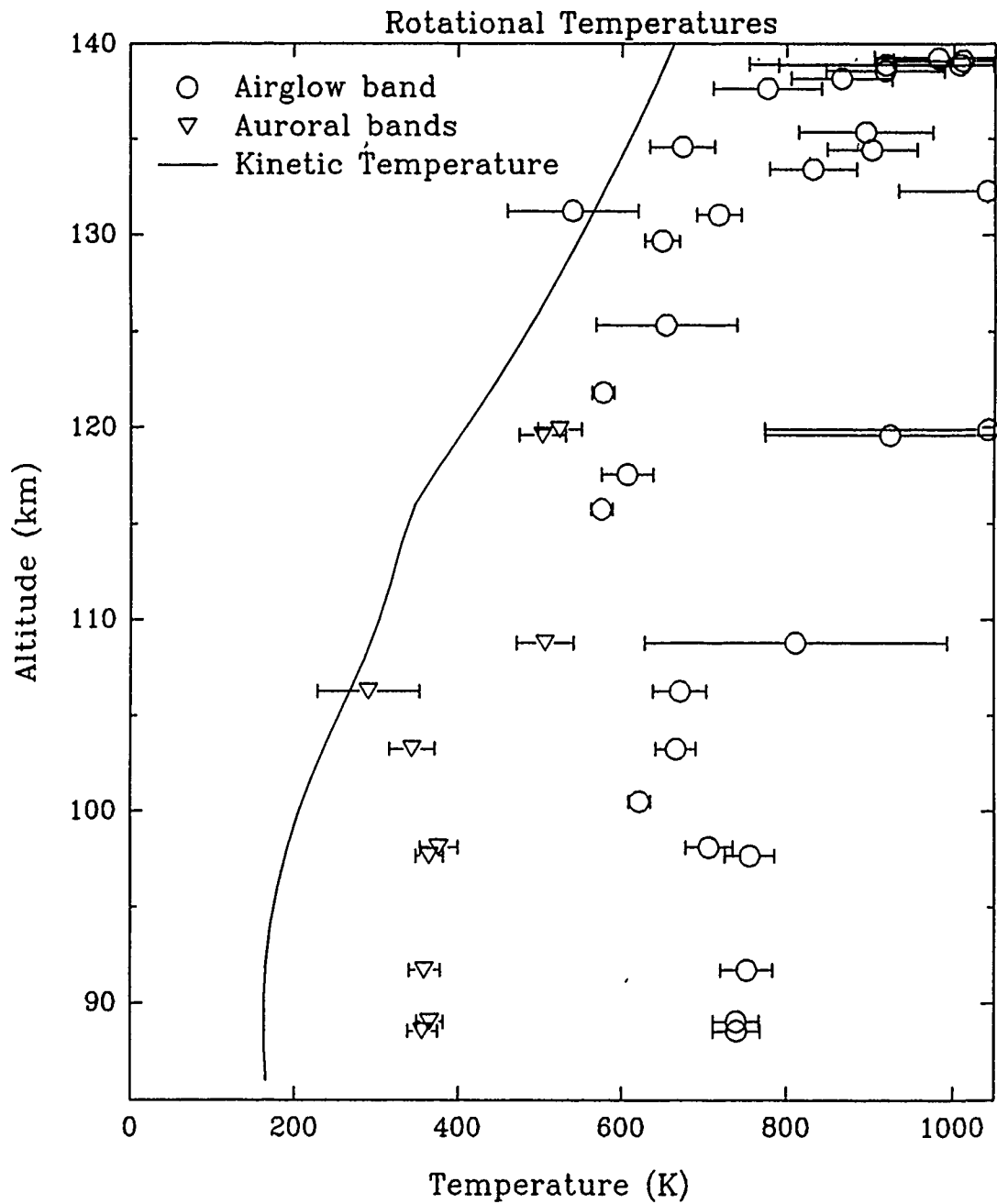
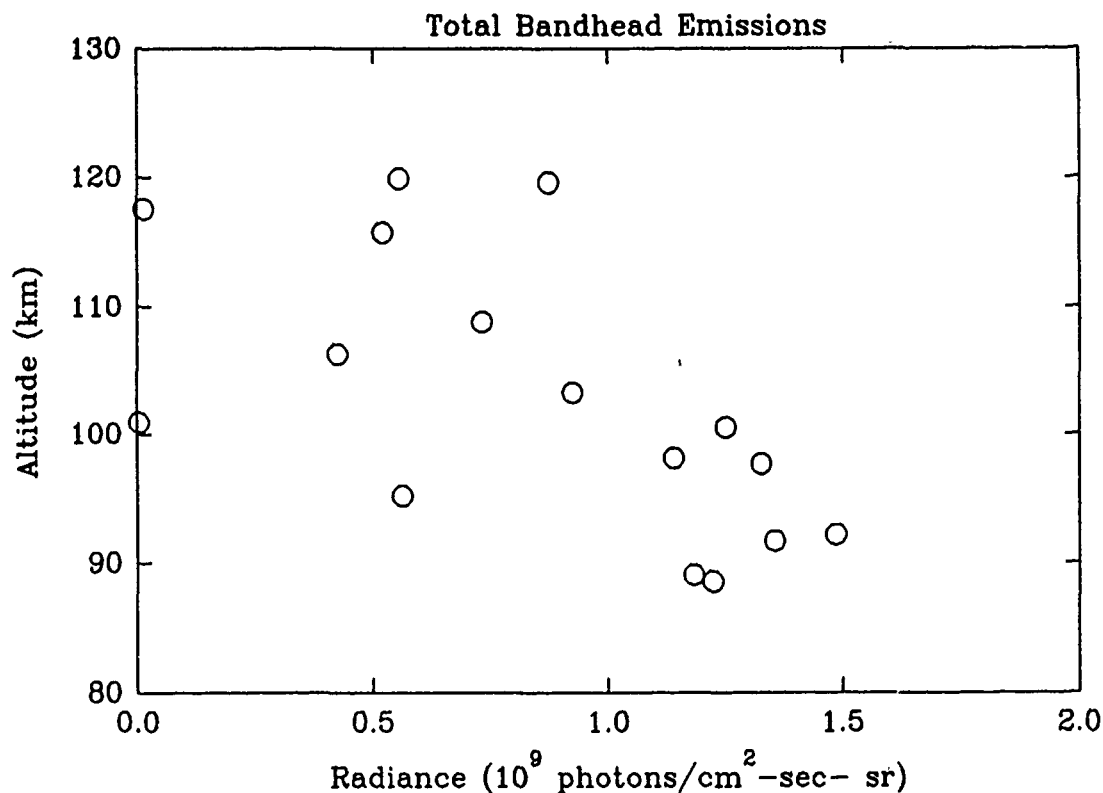Figure 44. NO background and auroral band rotational temperatures.

Total Bandhead Emissions

Figure 45. Band head emissions as determined by analysis of the FWI data. The sum of all three bands (v ' = 1, 2, 3) is shown.

Calculation of NO hot band auroral emissions requires knowledge of the electron dosing at the top of the atmosphere. Just before entering into the region of electron energy dissipation at an altitude of 85 km, onboard photometers monitoring 3914 Å N_2^+ (B $^2\Sigma$) 1N auroral emissions indicated an emission intensity of 6 kR (*Espy et al., 1988*). The ratio of total electron dosing to 3914 Å auroral emissions is approximately 1.15 ergs / cm^2- sec - kR (*Omholt, 1971*), implying an estimated auroral dosing of 6.9 ergs / cm^2 - sec. The rocket-borne photometry also indicated a Gaussian electron energy distribution function having a characteristic energy, E_o = 11 keV, and a distribution width, ΔE = 5.0 keV (*Picard et al., 1987*). These numbers were used in AARC to calculate the emissions shown in Figure 43.

As Figure 43 shows, the AARC model predicted auroral hot band emissions lower than the level seen in the FWI data. The source of this discrepancy is currently under active study. The resolution may involve a recalculation of the auroral production efficiencies used in the AARC model using updated rate constants and an atmospheric composition consistent with the conditions present at the time of the experiment.

Figure 47 shows the relative hot band radiances.

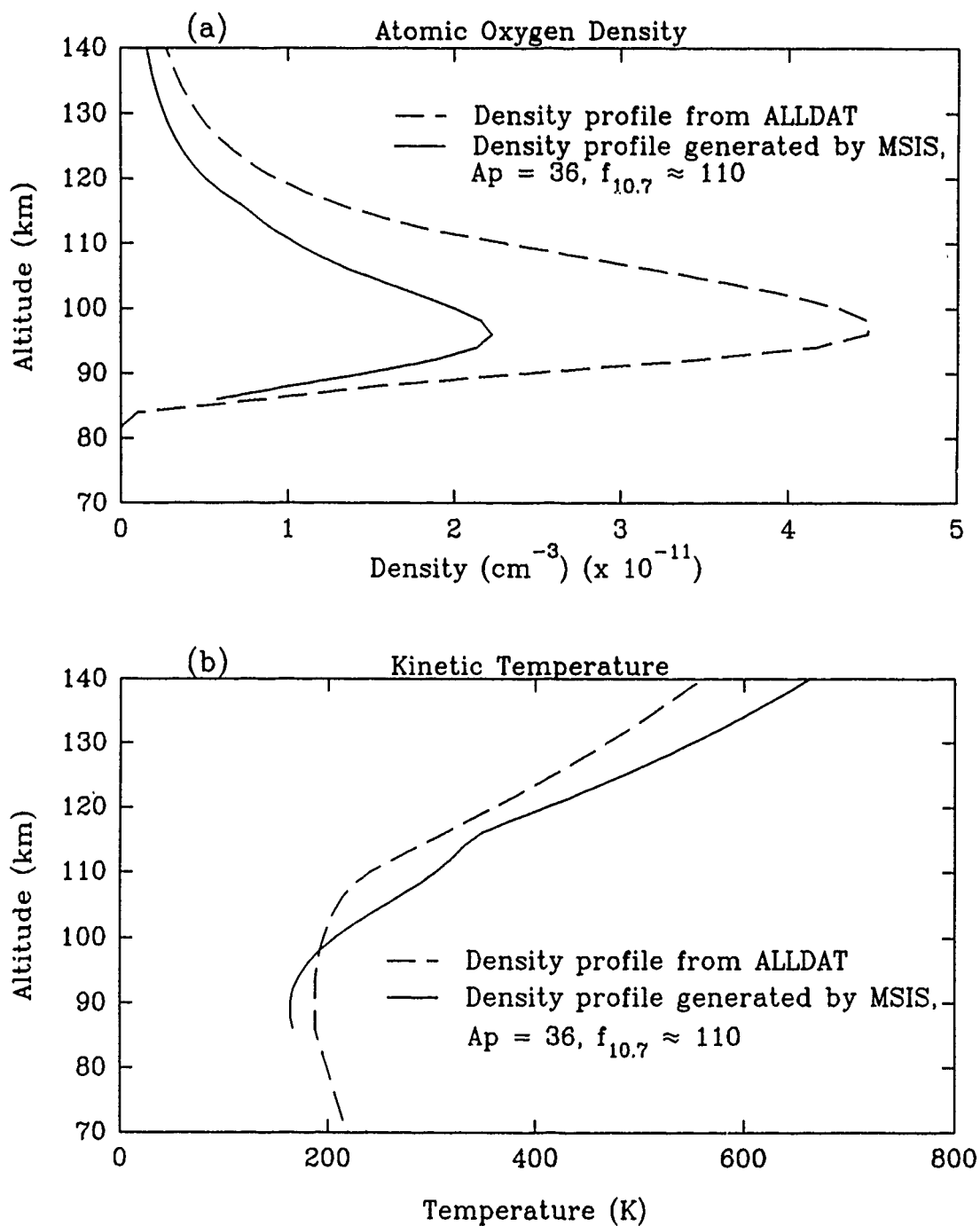Figure 46. (a) Two atomic oxygen profiles. The dashed line is the standard profile hard-wired into the AARC program; the solid line is generated by MSIS using the geomagnetic conditions at time of launch. (b) Two temperature profiles. The dashed line is the standard profile hard-wired into the AARC program; the solid line is generated by MSIS using the geomagnetic conditions at time of launch.
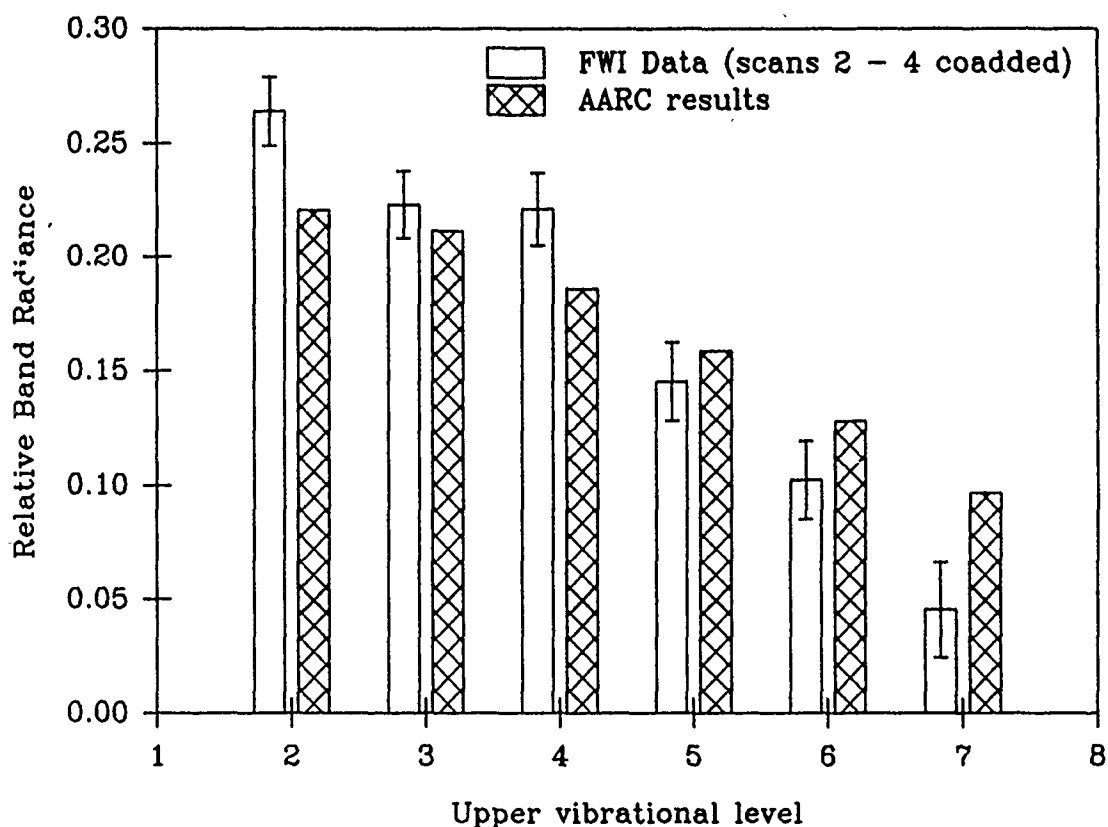
99

Figure 47. Relative hot band emissions for NO.

2. $CO_2(\nu_3)$ Emissions.

We have also used AARC to model the CO_2 emissions observed by the FWI experiment *(Joseph et al., 1986; Winick et al., 1988)*. A typical FWI CO_2 scan is shown in Figure 48.

The auroral dosing history used in AARC is shown in Figure 36. This figure shows the intensity of auroral 4278 Å $N_2^+(B\ ^2\Sigma)$ 1N emissions as seen by ground-based photometry in the direction toward the point in the sky where the rocket reaches an altitude of 100 km *(Espy et al., 1988)*. At 95 seconds into the flight (100 km altitude), the rocket-borne photometers indicated 3914 Å at 6 kR while the ground-based 4278 Å photometer, viewing the same region of the sky, indicated an intensity at approximately 1.2 kR. The two emissions originate from the same N_2^+ state with a branching ratio for 3914 Å a factor of 3 larger than that for 4278 Å *(Srivastava and Mirza, 1968)*. The rocket-borne photometers thus indicate auroral activity a factor of 1.6 greater than that indicated by the ground-based instruments. It is possible that emissions seen at ground level have experienced some atmospheric absorption. Since the time-dependent CO_2

100
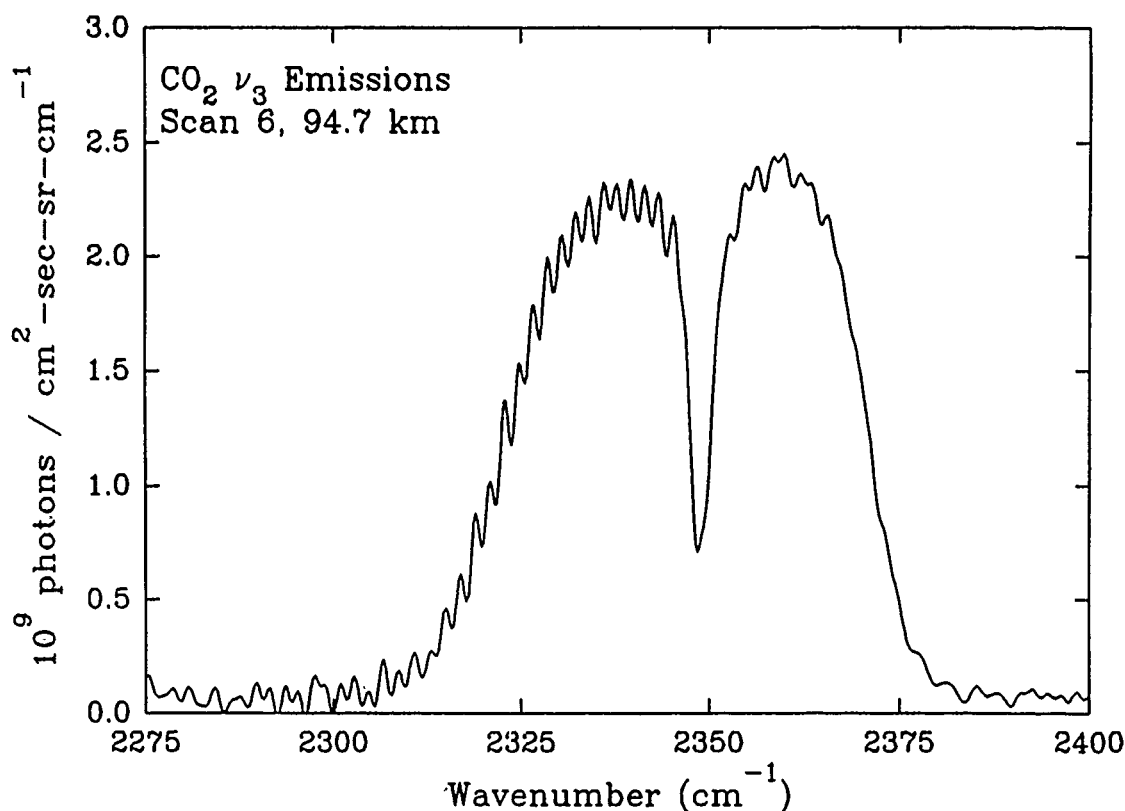
Figure 48. CO_2 Scan. Data from FWI Scan 10 (100 km).

calculation requires knowledge of dosing levels for periods of time not available from the rocket-borne data, we make the assumption that even though the ground-based measurement indicates a different level of dosing, the time-dependence indicated is valid. Thus the ground based measurements of auroral dosing have been used in the AARC model after being adjusted upward by a factor of 1.6. The time-steps used to approximate the time-varying aurora are shown in Figure 36.

A comparison of predicted and observed CO_2 integrated band emissions as a function of altitude is shown in Figure 49. The FWI band radiances shown are determined by integrating the data in the range of the CO_2 emissions (2300 cm^{-1} - 2400 cm^{-1}) and subtracting an appropriate baseline. The discrepancy below 95 km indicates a weakness in the escape-function approximation, which does not attempt to account for radiative transfer from other altitudes. Future modifications to the AARC model will address this shortcoming.

Figure 49. CO_2 (ν_3) total band radiance. Circles are radiances observed by FWI experiment; the solid line is radiance calculated by AARC.
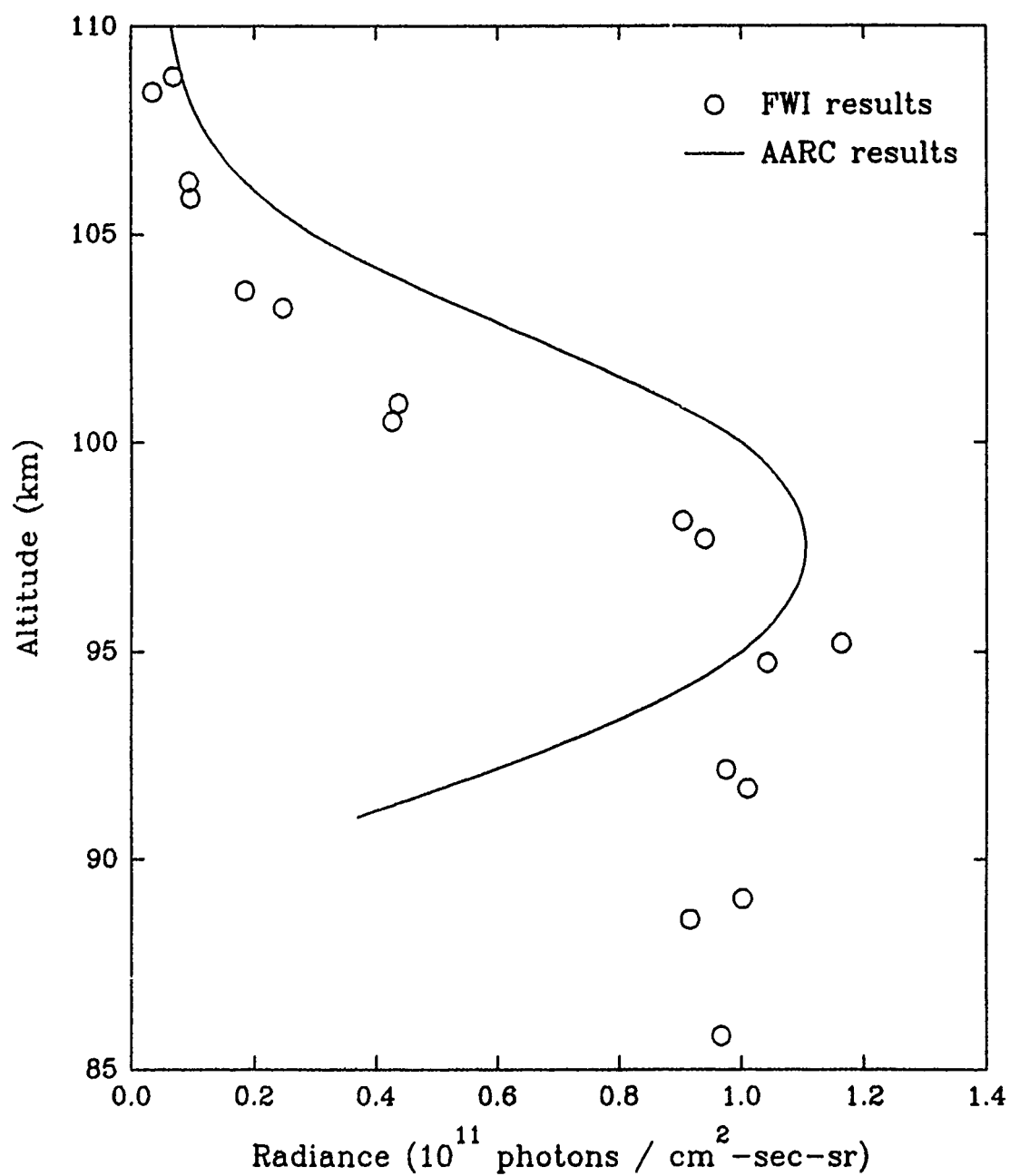
3. CO(v=1) Emissions.

The FWI data were also examined for CO(v=1) emissions in the range 2050 cm^{-1} to 2225 cm^{-1} using spectral decomposition methods similar to those used in the NO analysis. CO presents a simpler problem since only a single band is present. The data were fit to the form

$$y(\nu_i) = a + b\,\nu_i + c\,f(\nu_i)$$

where ν_i is the wavenumber, a, b, and c are the coefficients calculated by the fitting procedure, and $f(\nu_i)$ is the convolved synthetic spectrum. Note, the first two terms represent the equation of a line to account for the sloping baseline in the FWI data.

The synthetic spectra were generated using a Hamming response function with a FWHM of 1.65 cm^{-1}.

In Figure 50, the FWI data for Scan 2 (88.6 km) are shown. The P and R branches of CO are evident. Figure 51 is a fit of this scan. The P and R branches are clearly defined, reproducing the data quite well. Figure 52 is a plot of the residuals (data minus fit). The erratic pattern about zero magnitude indicates a good fit of this scan.

Some scans were unusable because of insufficient emissions. In some cases, an apparently good scan with strong emissions resisted analysis because of shifts in the wavenumber scale. Figure 53 shows, for example, Scan 133 (83.8 km) along with CO line positions. The FWI data shows P and R branches and appears to be a fittable scan; however, closer inspection of the data, especially the peaks, reveals a slight shift of the data. As previously discussed, the fitting process is not able to deal with situations with errors in the independent variable. Correcting this problem is difficult since the shifts do not remain constant even within a single scan.

Figure 54 is a plot of emission rate dependence on altitude as determined by fitting all usable scans. The plot indicates higher emission rates at lower altitudes.

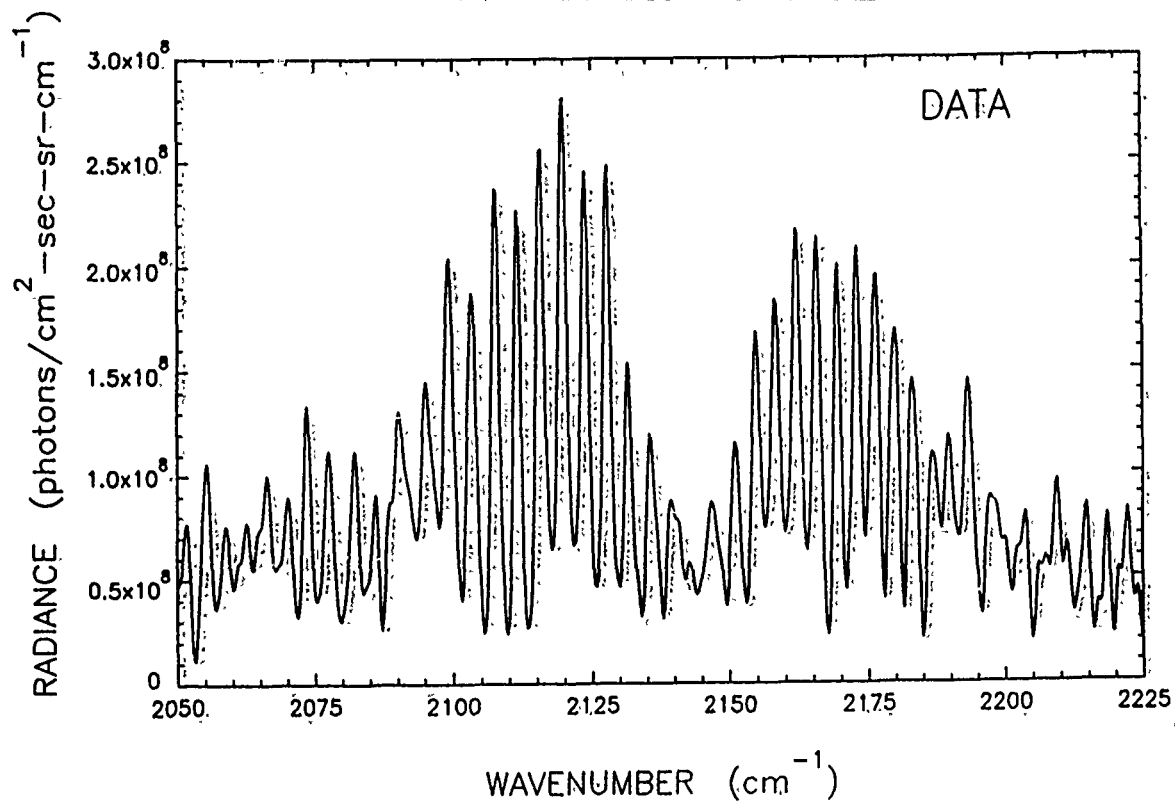Figure 50. CO emissions as seen in a low altitude, high resolution (FWHM = 1.65 cm^{-1}) FWI scan (Scan 2, 88.6 km).
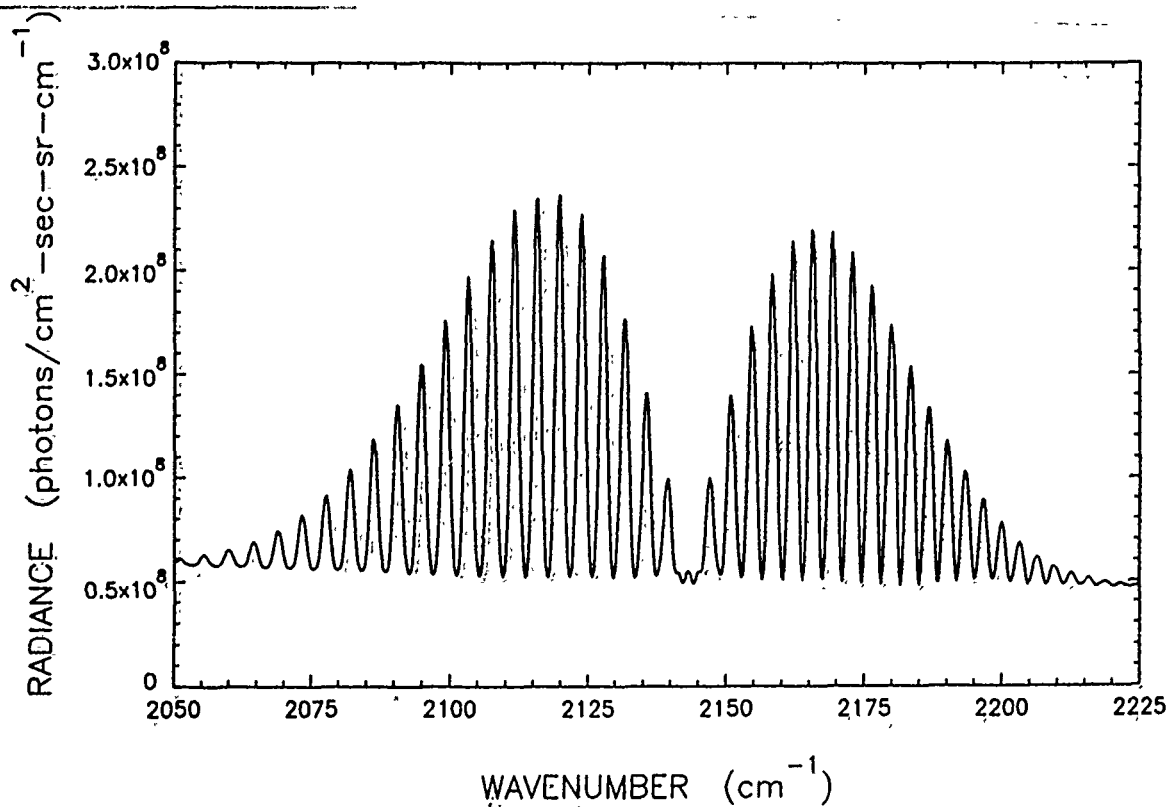
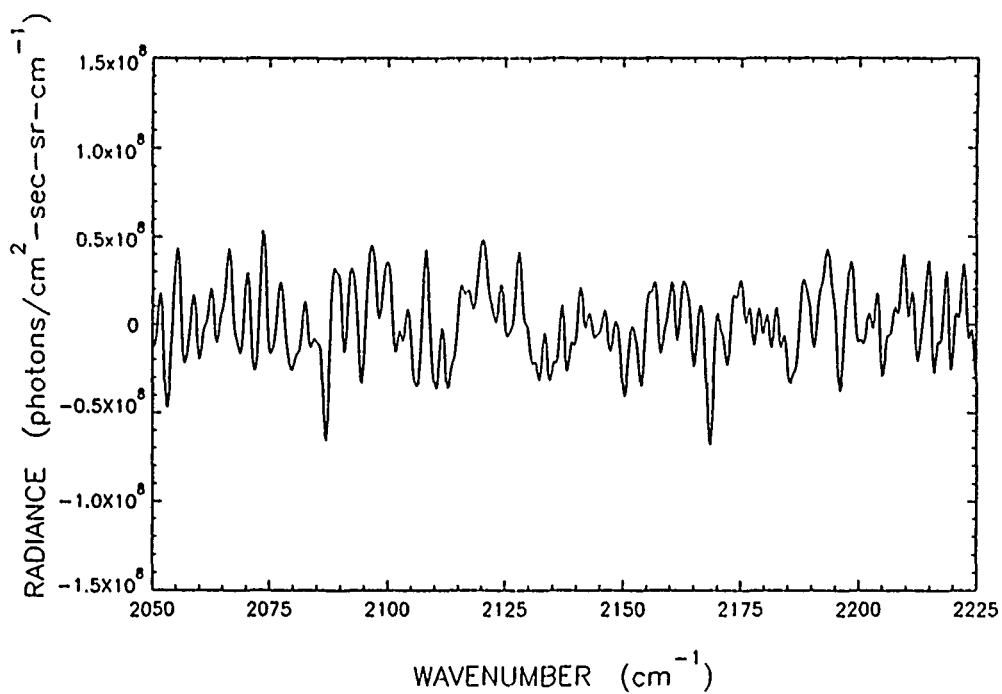Figure 51. Fit to FWI CO Scan 2 (88.6 km).

104

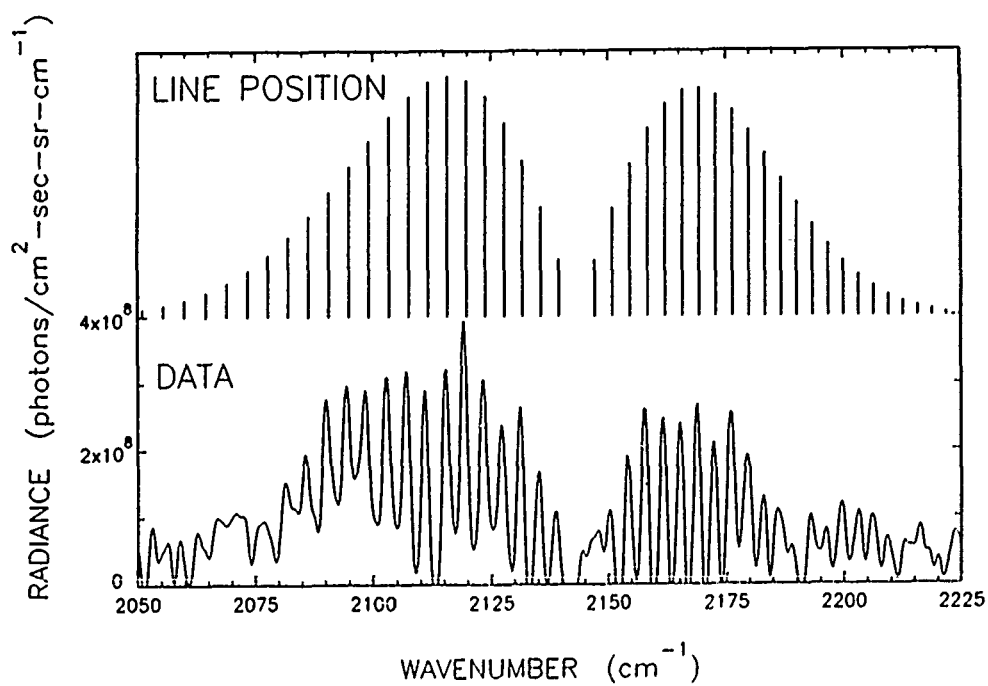**Figure 52.** Residuals from fitting Scan 2.

Figure 53. CO emissions from FWI Scan 133 (83.8 km). The lower plot is data from FWI; the upper plot shows CO line positions.

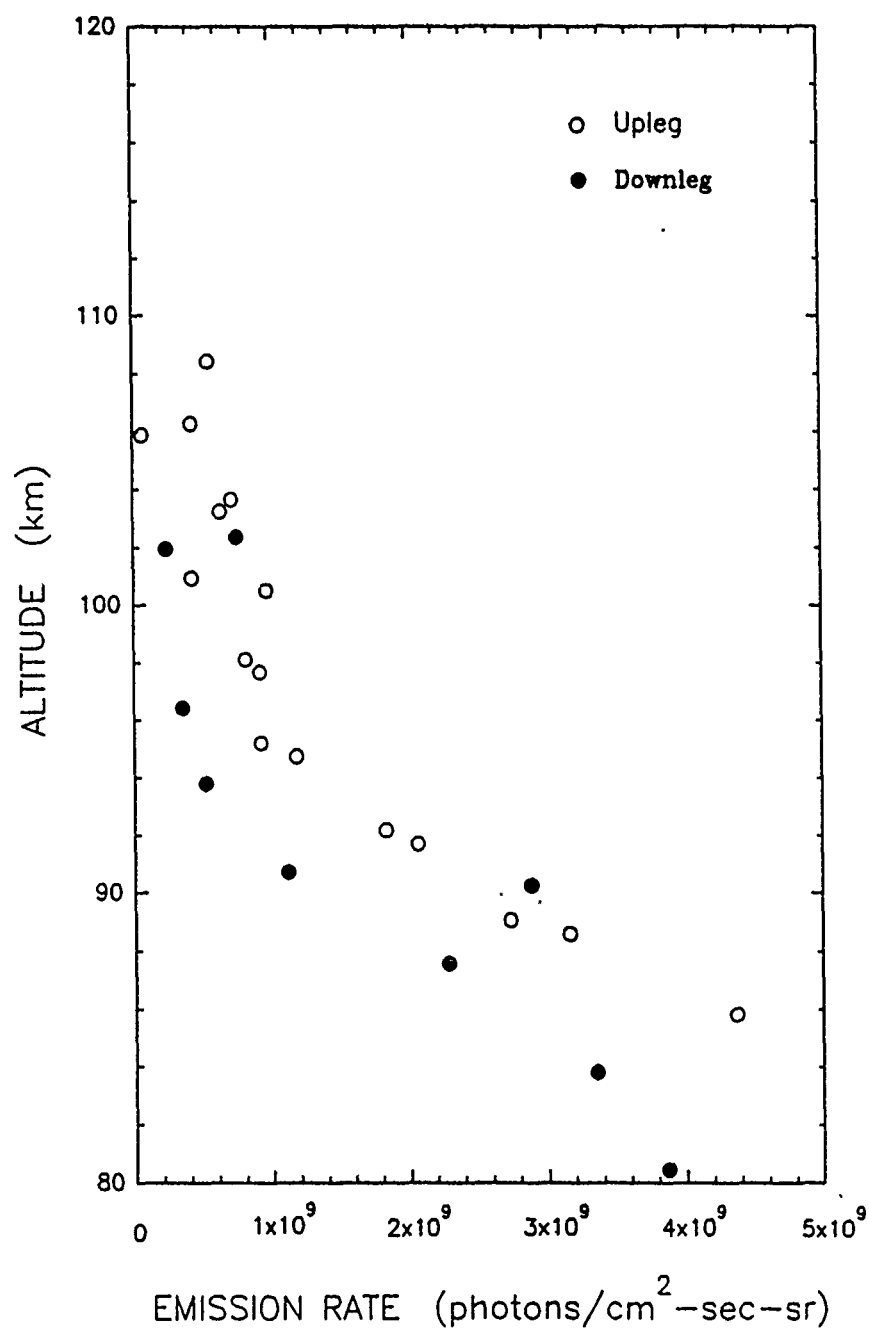105

CO (v=1) EMISSION RATE

Figure 54. CO(v=1) emission rate.

VI. APPLICATION PROGRAMS

In this section we review, very briefly, the current status of some of the codes we have written or modified that may be of some interest to others in the AFGL community.

A. MSIS-86 Driver

We have made extensive use of the MSIS-86 thermospheric model *(Hedin, 1987)*. In order to simplify our procedures, we modified the user-interface of the NSSDC code *(Bilitza, 1986)* that does the calculations. One reason for doing this is to make it a user-friendly program with menu-driven operation, which can load default values for the parameters and present the output data in a clear format. A second reason is to adhere to FORTRAN 77 standards. The program has been successfully executed on the VAX and APOLLO computers at AFGL.

The MSIS86 program which is accessed by the user interface, or driver, was modified only very slightly. On the Apollo system, this module must be compiled with the save option.

The MSIS driver modification has significantly facilitated use of the model. The original version required user specification of eight conditions, or parameters, such as altitude, latitude, and day of year. (When the code runs, seven of the eight conditions are held constant while the eighth becomes the variable parameter. The temperature and density profiles are then determined as a function of this variable parameter). Since specifying all of these conditions for each execution was a tedious and time consuming procedure, the MSIS driver was modified to load default values for all parameters and display them in the main menu (Figure 55). The user can review the parameter values and, if satisfied, can execute the program. Otherwise, the user can select which parameter to change and a submenu will appear querying the user for an input value. The program will then return to the main menu.

The parameter-input routines are similar to the routines developed for the AARC package (*Winick et al., 1987*). As with AARC, parameters default to the values used during the previous program execution. When the user is satisfied, parameter values are stored in a file so that they may be used as defaults the next time the program is run.

The MSIS driver modification has also created clearer data output. A header, explaining the program execution conditions, is displayed. It is followed by the output

```
*************************************************
********* MSIS THERMOSPHERE MODEL 1986 *********
*************************************************



     THIS PROGRAM ALLOWS YOU TO PRODUCE MSIS-PROFILES IN LATITUDE,
     LONGITUDE,SOLAR ACTIVITY,DAY,TIME,ALTITUDE OR MAGNETIC ACTIVITY.


     WHICH PARAMETER DO YOU WANT TO CHANGE?
     ----------------------------------------------------------------
                    0. NO FURTHER CHANGES

                    1. Selection of Variable     H/KM
                    2. Variable Range      85.00  100.00     5.00
                    3. Display or Store Output   MONITOR
                    4. ON/OFF Particular Variations    OFF

          5. Altitude       IS VARIABLE      9. Hour(LT)     0.0
          6. Latitude  GEOD    65.2         10. F10.7      220.0
          7. Longitude GEOD   212.4         11. F10.7M     220.0
          8. Day               280          12. AP         130.0

                 13. UPDATE DEFAULTS & EXIT PROGRAM
     ----------------------------------------------------------------
     ENTER NUMBER
     2


     CHOOSE YOUR VARIABLE RANGE:        BEGIN,     END, STEPWIDTH ?
                                #    85.0,   100.0,     5.0#


     ----------------------------------------------------------------

     90,120,5
         ----------------------------------------------------------------



     WHICH PARAMETER DO YOU WANT TO CHANGE?
     ----------------------------------------------------------------
                    0. NO FURTHER CHANGES

                    1. Selection of Variable     H/KM
                    2. Variable Range      90.00  120.00     5.00
                    3. Display or Store Output   MONITOR
                    4. ON/OFF Particular Variations    OFF

          5. Altitude       IS VARIABLE      9. Hour(LT)     0.0
          6. Latitude  GEOD    65.2         10. F10.7      220.0
          7. Longitude GEOD   212.4         11. F10.7M     220.0
          8. Day               280          12. AP         130.0

                 13. UPDATE DEFAULTS & EXIT PROGRAM
     ----------------------------------------------------------------
     ENTER NUMBER
     0
```

Figure 55. MSIS-86 driver menu.

data, with the variable parameter in the first column. The program output can be directed to the monitor screen or a file. An added feature is the ability to append data to an existing file. The program will read the existing file to determine which parameter is variable. The current execution output will be appended without a header only if it is consistent with the existing data file. Otherwise, a new header is written, followed by the data.

Originally, the driver file consisted of one main routine having many GO TO statements obscuring the flow of the program. Elimination of these branching statements was accomplished by dividing the program into seventeen routines, creating a logical, coherent program adhering to structured FORTRAN 77 standards (Figure 56). For example, subroutines for specification of parameters such as altitude were developed. Informational comments were inserted at the head of each routine as well as throughout the program. The format for the MSIS driver can serve as a template for drivers to other programs.

The purpose of the MAIN routine is to initialize variables and call other subroutines. The flow of execution always returns to the MAIN routine from a subroutine until the exit option is selected.

Subroutine MAINM displays the main menu of defaults for the various parameters from the prior execution.

Subroutine OUTDES designates whether the ouput should be displayed to the monitor or written to a file. A new file can be opened on Unit 16, or an existing file can be opened on Unit 17 for appending new data.

Subroutine APPF appends the output calculated from the current execution to the end of an existing output file from a prior execution. It will only append directly if the output is a continuation of the prior data in the file. If it is not a continuation then a new header will be added followed by the data.

Subroutine SELVAR queries the user to select any of the following parameters as the variable parameter: ALTITUDE, LATITUDE, LONGITUDE, DAY, HOUR, F10.7, F10.7M, or Ap.

Subroutine RANGE queries the user for the range of the variable by requiring a beginning, an ending, and an increment value.

Subroutine ONOFFP turns on/off various flags for calculations.

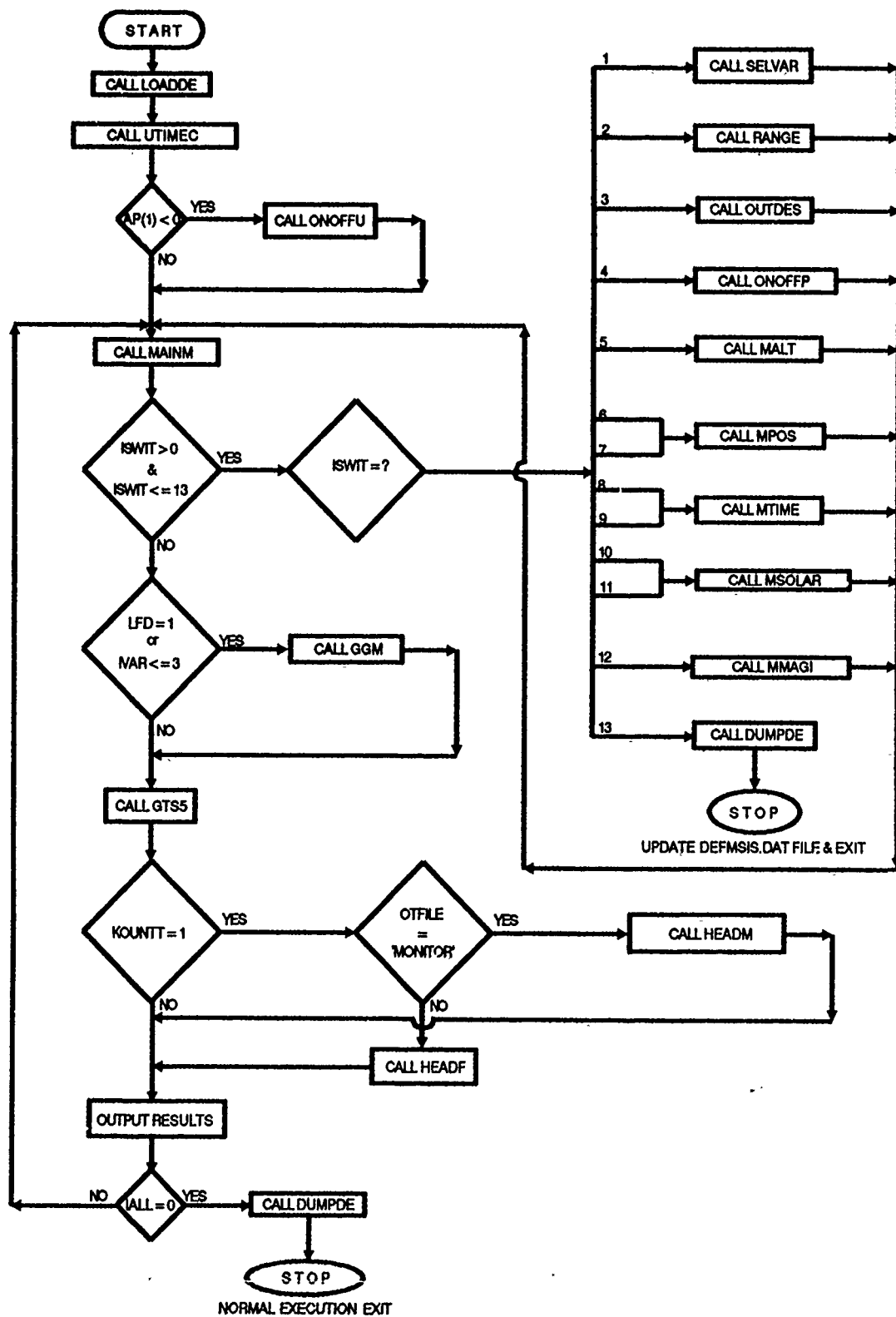Subroutine ONOFFU updates variables used in various flags for calculations.

Figure 56. MSIS-86 driver flow chart.

110

Subroutine MALT queries the user for altitude input.

Subroutine MPOS queries the user for position input: Latitude & Longitude (Geodetic or Geomagnetic).

Subroutine MTIME queries the user for time-of-year input: Day & Hour (LT or UT).

Subroutine UTIMEC queries the user for time and checks for universal time.

Subroutine MSOLAR queries the user for solar radio flux input, $F_{10.7}$: previous day and three-month average.

Subroutine MMAGI queries the user for magnetic index Ap input. Subroutine ONOFFU is called to update variables used in various flags for calculations.

Subroutine HEADM outputs a header of execution conditions to the monitor.

Subroutine HEADF outputs a header of execution conditions to a file.

Subroutine LOADDE loads parameter default values into the array DFLTS. If an error occurs while reading file DEFMSIS.DAT then secondary defaults stored in this subroutine will be read into array DFLTS. Then array DFLTS is read into variables. Another subroutine DUMPDE will update the file with the new values for the parameter defaults. Default values are input from file DEFMSIS.DAT on Unit 3. Previous default values are output to file BDEFMSIS.DAT on Unit 4.

Subroutine DUMPDE dumps the current parameter values to the file DEFMSIS.DAT. These then become the parameter defaults for the next execution. Default values are output to file DEFMSIS.DAT on Unit 3. Previous default values are input from file BDEFMSIS.DAT on Unit 4.

B. Programs to Facilitate Plotting of Results

The AURGRAF program is used to plot spectral radiance (SPECT output from AARC). The program was significantly enhanced for immediate visualization of spectral radiance data on the Apollo, Cyber, and VAX computers at AFGL. Program improvements allow more applications, easier use, and better graphics. The program uses the CDC PLOT Library Routines. A major application added is the ability to visualize stick plots of line data (LNSPEC output from AARC). The existing menu was elaborated for easier use and increased option selection. The program can calculate the beginning and ending axis limits from the data to be plotted or the user can select the axis limits. Two existing axis plotting subroutines were incorporated into the program

111

to enhance the graphics. Furthermore, semi-logarithmic and logarithmic axis features have been added. Finally, comments were inserted throughout the program.

The MULTIPLE PLOT program was written to plot x-y data on the Apollo computer. The program allows immediate visualization of data by the user. The program uses CDC PLOT Library Routines and is similar in design to the AURGRAF program. Also, the program is capable of plotting up to ten curves on one plot.

The DATA SMOOTHING program condenses a large x-y data set into an equivalent smaller set, facilitating data plotting and reducing storage requirements. For example, a program may generate a file of 10,000 data points, which may be too numerous to plot. The DATA SMOOTHING program will reduce the number of points without losing the plot's detailed characteristics. The user can select from two types of DATA SMOOTHING—the moving average method or the percent method. The moving average method averages n consecutive points, then the next n consecutive points, and so on. The percent method averages n consecutive points or less, depending upon whether two consecutive points fall within a certain tolerance. If the data are smooth, moving average can accurately reduce a large file into a small file. If the data are erratic, however, moving average will not produce acceptable results. In this case, the percent method is advisable, though the degree of condensation will be less than with the moving average method.

C. ARC Codes

The AFGL Atmospheric Radiance Code (ARC) consists of several stand-alone codes that are used for modeling non-LTE regions of the quiescent atmosphere. Most of these are line-by-line codes using the HITRAN database *(Rothman et al, 1987)*. They can also be used in the LTE regions of the lower atmosphere for all cases where line overlap is not a serious problem. They are all written in ANSI-standard FORTRAN 77, for ease of use on different machines. The only system-specific references are to subroutines giving the run date and run time.

1. RAD

RAD is the basic code that we use to model non-LTE populations of CO_2 and CO vibrational states, as described in Sections II-IV; as the name suggests, it is based on the RAD algorithm, described in Section I. It was written so that populations of different vibrational states, or combinations of states, could be calculated with the minimum number of state-specific source-code modifications. To this end, the code

112

consists of seven source modules. The first contains the driver and the principal line-by-line radiative transfer subroutine. Five others contain subprograms that are used for all applications. The seventh contains code that (1) sets up, or reads in, parameters for the rate constants that describe the kinetic processes involved in each specific case; and (2) does the vibrational-temperature calculation in question. (We call these "version modules", and give them names beginning with "VER".) We thus create a number of executable modules by linking the first six source modules with each of the version modules.

The current running code for RAD is Version 26. RAD continues to evolve, however, and there has been no formal release with accompanying documentation. At present it is used for (1) the CO_2 bend-stretch states as described in Section II; (2) the $^iCO_2(00011)$ states of each isotope, coupled individually with N_2 (but see the comments on RADC, below); (3) the $CO_2(01111)$ state as described in Section III; and (4) the $CO(v=1)$ state as described in Section IV.

Input requirements for each realization of RAD can be found in comments in the source code. All versions require a directive file on Unit 1, a principal atmospheric profile on Unit 2, and a line file consisting of an appropriate subset of the HITRAN database on Unit 3. Unless one is using the U.S. Standard Atmosphere (1976), a secondary atmospheric profile specifying total number density, $[N_2]$, $[O_2]$, and $[O]$ is read from Unit 9. Subsidiary vibrational-temperature or number-density profiles may be read from Unit 11, as needed. Unit 12 is reserved for solar-flux absorption coefficients, calculated by program SABS, that are used for simulating daytime conditions for solar-pumped states.

Units 4-7 are used for output. Detailed program output is written to units 4 and 5. This is used to report the input data and specific intermediate calculations, and to give all the final results. Unit 6 is used to report the progress of the calculation as it proceeds and to print diagnostic messages. One should always refer to this file after each production run to make sure that the process ran normally. Unit 7 is used as an output file, giving the vibrational temperatures as a function of altitude, and other information, in a format that is suitable for input to most of the other ARC programs.

2. RADC

RADC is the basic code that we use to model the $^iCO_2(00011)$-$N_2(v=1)$ vibrational temperatures, as described in Section III. This calculation couples four CO_2 isotopes, and it supercedes the RAD version for $CO_2(\nu_3)$ that is mentioned above. The structure

ol RADC is the same as that of RAD, and indeed most of the subprograms are the same, or very similar. Therefore, all of the comments of the previous section except some in the second paragraph apply here. The current running code for RADC is Version 2.

RADC can be used to model $CO_2(\nu_3)$ emissions in the presence of auroral dosing. In this case, unit 11 is used for input consisting of certain $N_2(v=1)$ production rates that are calculated by AARC (Section V). The usefulness of this capability is limited by the fact that the basic calculation assumes steady-state conditions. Nevertheless, it has proved to be valuable in identifying radiative-transfer effects both within and below the dosing region.

3. VPMP

In the past, we have reported calculations of vibrational temperatures of high-lying states of CO_2 that are pumped by short-wave solar radiation at 2.7 and 2.0 μm (*Sharma and Wintersteiner, 1985; Wintersteiner and Joseph, 1986;* also see Section III). The codes that perform these calculations have been rewritten, and consolidated as program VPMP. The basic processes involved are the same as those reported earlier. Other than having a single code for all the groups of states under consideration rather than four separate codes, the only substantive differences involve better facilities for reading input profiles, such as the N_2 vibrational temperature, and rate constants. It is thus easier to conform with our other calculations.

The current running code for VPMP is Version 3. This code is the only one among the ARC codes, save for the convolution program CONV2PA, that does not do a line-by-line calculation. However, it does rely upon results of the line-by-line solar-flux absorption code, SABS.

4. SABS

SABS is our code for calculating absorption coefficients for solar-pumped vibrational states by evaluating the attenuation of solar flux as it passes through a spherical-shell atmosphere (*Sharma and Wintersteiner, 1985; Wintersteiner and Joseph, 1986*). The principal modifications that have been made recently involve (1) the facility to calculate absorption for cases where the solar zenith angle is greater than 90^0; (2) an improved algorithm for integrating across the line profile for extremely self-absorbed lines, as may be found at low altitudes; (3) A finer-spaced data set for exoatmospheric solar flux (*Thekackara, 1973*); and (4) the procedure for adjusting the exoatmospheric flux for

114

solar absorption lines, as described in Section IV on the CO calculation.

The current running code for SABS is Version 7. The input units 1, 2, 3, and 9, and the output units 4, 5, and 6 are used in a manner that is very similar to the description given above for RAD. Unit 7 is an output file containing the solar flux absorption coefficients as a function of altitude.

5. NLTE

NLTE is our code for calculating the limb radiance, or zenith radiance, in infrared bands, provided that the vibrational temperatures of the emitting states are given. It has been described in detail by *Wintersteiner and Sharma (1985)*. Most of the important changes that have been implemented since that time should be transparent to the user. They mainly involve matters of program efficiency, although the same algorithm for integrating across the line profiles that was described above, in connection with SABS, has also been improved in NLTE. The only noticable change involves the spectral output data, which previously was written to Unit 7 and/or Unit 8 as completed synthetic spectra. Now it is possible, as an alternative, to write stick spectra to these units and then use CONV2PA to produce synthetic spectra.

The current running version for NLTE is version 48.

6. NLTEA

NLTEA is a program that we use for calculating radiance for cases in which the viewing path traverses a region of auroral dosing. We have also used it to simulate limb scans that cross the day/night boundary, as described in Section III. The code is a derivative of NLTE, but since its initial application to the auroral problem *(Wintersteiner and Joseph, 1986)*, it has not been updated as NLTE has. The current running code for NLTEA is version 3.

7. CONV2PA

The program CONV2PA is a modification of CONV, originally written as part of the AARC package (*Winick et al., 1987*). This program performs a convolution of the stick spectra generated by NLTE with an instrumental response function, producing synthetic spectra equivalent to spectra observed by experimental devices. The program is furnished with a user-friendly front end similar to the one developed for the AARC package. Like AARC, CONV2PA allows the user to change any user-specified parameter through a system of menus. If not changed, a parameter will default to the most

115

...ntly used value. When the user is satisfied with the parameters, those values are written to a file so that they may be used as defaults the next time the program is run.

In the case of CONV2PA, the user may specify the name of the input file containing the NLTE-generated stick spectra, the position of the data within the input file, the name of the output file which will receive the synthetic spectra, the bounds of the generated spectrum, and the type of instrumental response function to be used along with the Full-Width-at-Half-Maximum. The instrumental response functions available are: triangular, Gaussian, sinc, Hamming, and rectangular.

The current running code of CONV2PA is version 3.

D. AARC

AARC is a set of routines which calculate NO, NO^+, and CO_2 infrared emissions due to auroral excitation. The codes have been described in detail by *Winick, et al. (1987)*. Many enhancements have been made since the initial release. The changes include allowance for multiple auroral dosing levels, the ability to model zenith-looking geometries, and the ability to specify alternate input and output files. The latest version of AARC includes a "zeroth" attempt at including NO band head emissions in terms of efficiencies derived from the FWI field experiment.

REFERENCES

Allen, D. C., and C. J. S. M. Simpson, Vibrational energy exchange between CO and the isotopes of N_2 between 300° K and 80° K, *Chem. Phys. 45*, 203-211, 1980.

Allen, D. C., T. Scragg, and C. J. S. M. Simpson, Low temperature fluorescence studies of the deactivation of the bend-stretch manifold of CO_2, *Chem. Phys., 51*, 279-298, 1980.

Anderson, G. P., S. A. Clough, F. X. Kneizys, J. H. Chetwynd, and E. P. Shettle, AFGL atmospheric constituent profiles (0-120 km), *Rep. AFGL-TR-86-0110*, 43 pp., Air Force Geophysics Lab., Bedford, Mass., 1986, ADA175173.

Barnett, J. J., and M. Corney, Middle atmosphere reference model derived from satellite data, in *Middle Atmosphere Program, Handbook for MAP Volume 16*, edited by K. Labitzke, J. J. Barnett, and B. Edwards, pp. 47-85, 1985.

Beer, R., C. B Farmer, M. R. Gunson, and R. Zander, Observational evidence for anomalous CO and CO_2 depletion above 80 km in the Earth's atmosphere, in *Proc., Atmos. Spect. Applic. Workshop 1-3 Sept. 1987*, edited by J. Ballard, Rep. RAL-88-009, pp. 1-7, 1987.

Bilitza, D., NASA/GSFC MSIS-86 thermospheric model, National Space Science Data Center, code 630.2, NASA-Goddard Space Flight Center, Greenbelt, MD, 1986.

Caledonia, G. E., and J. P. Kennealy, NO infrared radiation in the upper atmosphere, *Planet. Space Sci., 30*, 1043-1056, 1982.

Caledonia, G. E., B. D. Green, and R. M. Nadile, The analysis of SPIRE measurements of atmospheric limb $CO_2(\nu_2)$ fluorescence, *J. Geophys. Res., 90*, 9783-9788, 1985.

Chandrasekhar, S., *Radiative Transfer*, 393 pp., Dover, New York, 1960.

Despain, A. M., D. J. Baker, A. J. Steed, and T. Tohmatsu, Extended-field large-aperture interferometer-spectrometer for airglow surveys, *Appl. Optics, 10*, 1870, 1971.

Dickinson, R. E., Infrared radiative cooling in the mesosphere and lower thermosphere, *J. Atmos. Terr. Phys.*, *46*, 995-1008, 1984.

Espy, P. J., C. R. Harris, A. J. Steed, J. C. Ulwick, R. H. Haycock, and R. Straka, Rocketborne interferometer measurement of infrared auroral spectra, *Planet. Space Sci.*, *36*, 543-551, 1988.

Farmer, C. B., and R. H. Norton, *A high-resolution atlas of the infrared spectrum of the Sun and the Earth atmosphere from space, a compilation of the ATMOS spectra of the region from 650 to 4800 cm^{-1} (2.3 to 16 μm). Volume I. The Sun*, NASA Ref. Pub. 1224, Washington, DC, 1989.

Fernando, R. P., and I. W. M. Smith, Vibrational relaxation of NO by atomic oxygen, *Chem. Phys. Lett.*, *66*, 218-222, 1979.

Girard, A., J. Besson, D. Brard, J. Laurent, M. P. Lemaitre, C. Lippens, C. Muller, J. Vercheval, and M. Ackerman, Global results of grille spectrometer experiment on board Spacelab 1, *Planet. Space Sci.*, *36*, 291-300, 1988.

Goldman, A., and S. C. Schmidt, Infrared spectral line parameters and absorptance calculations of NO at atmospheric and elevated temperatures for the $\Delta v = 1$ bands region, *J. Quant. Spectrosc. Radiat. Transfer*, *15*, 127-138, 1975.

Gordiets, B. F., Yu. N. Kulikov, M. N. Markov, and M. Ya. Marov, Numerical modeling of the thermospheric heat budget, *J. Geophys. Res.*, *87*, 4504-4514, 1982.

Gueguen, H., F. Yzambart, A. Chakroun, M. Margottin-Maclou, L. Doyenette, and L. Henry, Temperature dependence of the vibration-vibration transfer r..es from CO_2 and N_2O states excited in the 00^01 vibrational level to $^{14}N_2$ and $^{15}N_2$ molecules, *Chem. Phys. Lett.*, *35*, 198-201, 1975.

Harris, R. D., and G. W. Adams, Where does the $O(^1D)$ energy go?, *J. Geophys. Res.*, *88*, 4918-4928, 1983.

Haycock, R. H. and D. J. Baker, Infrared prism interferometer-spectometer using a gas-lubricated drive bearing, *Infrared Phys.*, *14*, 259, 1974.

Hedin, A. E., MSIS-86 thermospheric model, *J. Geophys. Res., 92*, 4649-4662, 1987.

Hedin, A. E., Atomic oxygen modeling in the upper thermosphere, *Planet. Space Sci., 36*, 907-920, 1988.

Huber, K.-P., and G. Herzberg, *Molecular Spectra and Molecular Structure IV. Constants of Diatomic Molecules*, Van Nostrand Reinhold Company, New York, 1979.

Inoue, G., and S. Tsuchiya, Vibration-to-vibration energy transfer of $CO_2(00^01)$ with N_2 and CO at low temperatures, *J. Phys. Soc. Jap., 39*, 479-486, 1975.

James, T. C., and J. B. Kumer, Fluorescence of CO_2 near 4.3 microns: application to daytime limb radiance calculations, *J. Geophys. Res., 78*, 8320-8329, 1973.

Joseph, R. A., R. H. Picard, J. R. Winick, and P. P. Wintersteiner, Analysis of CO_2 ν_3 infrared emission from the aurorally dosed lower thermosphere, *EOS Trans. A.G.U., 67*, 1135, 1986.

Joseph, R. A., A. J. Paboojian, R. H. Picard, J. R. Winick, and P. P. Wintersteiner, Analysis of NO $\Delta v = 1$ high-resolution rocketborne infrared spectra: Altitude dependence and bandheads, *EOS Trans. A.G.U., 70*, 1236, 1989.

Kahaner, D., C. Moler, and S. Nash, *Numerical Methods and Software*, Prentice Hall, Englewood Cliffs, NJ, 1989, pp. 218-222.

Keneshea, T. J., S. P. Zimmerman, and C. R. Philbrick, A dynamic model of the mesosphere and lower thermosphere, *Planet. Space Sci., 27*, 385-401, 1979.

Kumer, J. B., and T. C. James, $CO_2(001)$ and N_2 vibrational temperatures in the $50 \lesssim z \lesssim 130$ km altitude range, *J. Geophys. Res., 79*, 638-648, 1974.

Kumer, J. B., Atmospheric CO_2 and N_2 vibrational temperatures at 40- to 140-km altitude, *J. Geophys. Res., 82*, 2195-2202, 1977a.

Kumer, J. B., Theory of the CO_2 4.3-μm aurora and related phenomena, *J. Geophys. Res., 82*, 2203-2209, 1977b.

Kumer, J. B., A. T. Stair, Jr., N. Wheeler, K. D. Baker, and D. J. Baker, Evidence for an $OH^* \xrightarrow{vv} N_2^* \xrightarrow{vv} CO_2(\nu_3) \longrightarrow CO_2 + h\nu(4.3\mu m)$ mechanism for 4.3 μm airglow, *J. Geophys. Res.*, *83*, 4743-4747, 1978.

Kumer, J. B., and T. C. James, SPIRE data evaluation and nuclear IR fluorescence processes, *Rep. DNA 6237F*, 114 pp., Defense Nuclear Agency, Washington, D.C., 1982.

Lopez-Puertas, M., R. Rodrigo, A. Molina, and F. W. Taylor, A non-LTE radiative transfer model for infrared bands in the middle atmosphere. I. Theoretical basis and application to CO_2 15 μm bands., *J. Atmos. Terr. Phys.*, *48*, 729-748, 1986a.

Lopez-Puertas, M., R. Rodrigo, J. J. Lopez-Moreno, and F. W. Taylor, A non-LTE radiative transfer model for infrared bands in the middle atmosphere. II. CO_2 (2.7 and 4.3 μm) and water vapour (6.3 μm) bands and $N_2(1)$ and $O_2(1)$ vibrational levels, *J. Atmos. Terr. Phys.*, *48*, 749-764, 1986b.

Lunt, S. L., C. T. Wickham-Jones, and C. J. S. M. Simpson, Rate constants for the deactivation of the 15 μm band of carbon dioxide by the collision partners CH_3F, CO_2, N_2, Ar, and Kr over the temperature range 300 to 150 K, *Chem. Phys. Lett.*, *115*, 60-64, 1985.

Mastrocinque, G., A Chakroun, L. Doyennette, H. Gueguen, M. Margottin-Maclou, and L. Henry, Vibrational energy transfer from the v=1 level of carbon monoxide to the v=1 level of the two isotopic species of nitrogen: $^{14}N_2$ and $^{15}N_2$, *Chem. Phys. Lett.*, *39*, 347-349, 1976.

Offermann, D., and K. U. Grossmann, Thermospheric density and composition as determined by a mass spectrometer with cryo ion source, *J. Geophys. Res.*, *78*, 8296-8304, 1973.

Offermann, D., V. Friedrich, P. Ross, and U. von Zahn, Neutral gas composition measurements between 80 and 120 km, *Planet. Space Sci.*, *29*, 747-764, 1981.

Omholt, A., *The Optical Aurora*, 198 pp., Springer-Verlag, New York, 1971.

Ortega, J. M., *Matrix Theory*, Plenum Press, New York, 1987, p. 135.

Picard, R. H., J. R. Winick, R. D. Sharma, A. S. Zachor, P. J. Espy, and C. R. Harris, Interpretation of infrared measurements of the high-latitude thermosphere from a rocket-borne interferometer, *Adv. Space Res.*, *7*, (10)23-(10)30, 1987.

Press, W. H., B. P. Flannery, S. A. Teukolsky, and W. T. Vetterling, *Numerical Recipes*, Cambridge University Press, Cambridge, 1986.

Rawlins, W. T., M. E. Fraser, and S. M. Miller, Rovibrational excitation of nitric oxide in the reaction of O_2 with metastable atomic nitrogen, *J. Phys. Chem.*, *93*, 1097-1107, 1989.

Rees, M. H. Auroral ionization and excitation by incident energetic electrons, *Planet. Space Sci.*, *111*, 1209-1218, 1964.

Rosser, Jr., W. A., A. D. Wood, and E. T. Gerry, Deactivation of vibrationally excited carbon dioxide (ν_3) by collisions with carbon dioxide or with nitrogen, *J. Chem. Phys.*, *50*, 4996-5008, 1969.

Rothman, L. S., Infrared energy levels and intensities of carbon dioxide. Part 3, *Appl. Opt.*, *25*, 1795-1816, 1986.

Rothman, L. S., R. R. Gamache, A. Goldman, L. R. Brown, R. A. Toth, H. M. Pickett, R. L. Poynter, J.-M. Flaud, C. Camy-Peyret, A. Barbe, N. Husson, C. P. Rinsland, and M. A. H. Smith, The HITRAN database: 1986 edition, *Appl. Opt.*, *26*, 4058-4097, 1987.

Sharma, R. D., and P. P. Wintersteiner, CO_2 component of daytime earth limb emission at 2.7 micrometers, *J. Geophys. Res.*, *90*, 9789-9803, 1985.

Sharma, R. D., and P. P. Wintersteiner, Role of carbon dioxide in cooling planetary thermospheres, *Geophys. Res. Lett.*, in press, 1990.

Sharma, R. D., and R. M. Nadile, Carbon dioxide (ν_2) radiance results using a new nonequilibrium model, AIAA-81-0426, paper presented at AIAA 19th aerospace sciences meeting, St. Louis, Mo, 1981.

Sharp, W. E., Upper limits to [O] in the lower thermosphere from airglow, *Planet. Space Sci.*, *33*, 571-575, 1985.

121

Shved, G. M., G. I. Stepanova, and A. A. Kutepov, Transfer of 4.3 μm CO_2 radiation on departure from local thermodynamic equilibrium in the atmosphere of the Earth, *Izvestiya, Atmos. Ocean. Physa.*, *14*, 589-596, 1978.

Simpson, C. S. J. M., P. D. Gait, and J. M. Simmie, The vibrational deactivation of the bending mode of CO_2 by O_2 and by N_2, *Chem. Phys. Lett.*, *47*, 133-136, 1977.

Slanger, T. G., and G. Black, Electronic to vibrational energy transfer efficiency in the $O(^1D) - N_2$ and $O(^1D) - CO$ system, *J. Chem. Phys.*, *60*, 468, 1974.

Solar-Geophysical Data, 464 Part I, April 1983, U. S. Department of Commerce (Boulder, Colorado, USA 80303).

Srivistava, B. N., and I. M. Mirza, Measurements of the electron impact excitation cross section of $N_2{}^+$ first negative bands, *Phys. Rev.*, *176*, 137-140, 1968.

Stair, Jr., A. T., R. D. Sharma, R. M. Nadile, D. J. Baker, and W. F. Grieder, Observations of limb radiance with cryogenic spectral infrared rocket experiment, *J. Geophys. Res.*, *90*, 9763-9775, 1985.

Taine, J., and F. Lepoutre, A photoacoustic study of the collisional deactivation of the first vibrational levels of CO_2 by N_2 and CO, *Chem. Phys. Lett.*, *65*, 554-558, 1979.

Taine, J., F. Lepoutre, and G. Louis, A photoacoustic study of the collisional deactivation of CO_2 by N_2, CO, and O_2 between 160 and 375 K, *Chem. Phys. Lett.*, *58*, 611-615, 1978.

Taylor, R. L., Energy transfer processes in the stratosphere, *Can. J. Chem.*, *52*, 1436-1451, 1974.

Thekaekara, M. P., Solar energy outside the Earth's atmosphere, *Solar Energy*, *14*, 109-127, 1973.

Trinks, H., and K. H. Fricke, Carbon dioxide concentrations in the lower thermosphere, *J. Geophys. Res.*, *83*, 3883-3886, 1978.

Trinks, H., D. Offermann, U. von Zahn, and C. Steinhauer, Neutral composition measurements between 90- and 220-km altitude by rocket-borne mass spectrometer, *J. Geophys. Res., 83*, 2169-2176, 1978.

Vercheval, J., C. Lippens, C. Muller, M. Ackerman, M.-P. Lemaitre, J. Besson, A. Girard, and J. Laurent, CO_2 and CO vertical distribution in the middle atmosphere and lower thermosphere deduced from infrared spectra, *Annales Geophysicae, 4*, 161-164, 1986.

Winick. J. R., R. H. Picard, R. A. Joseph, R. D. Sharma, and P. P. Wintersteiner, An infrared spectral code for the auroral thermosphere (AARC), *Rep. AFGL-TR-87-0334*, 228 pp., Air Force Geophysics Lab., Bedford, Mass., 1987, AD202432.

Winick, J. R., R. H. Picard, R. D. Sharma, R. A. Joseph, and P. P. Wintersteiner, 4.3 μm radiation in the aurorally dosed lower thermosphere: modeling and analysis, in *Prog. in Atmos. Phys.*, edited by R. Rodrigo, J. J. Lopez-Moreno, M. Lopez-Puertas, and A. Molina, pp. 229-237, Kluwer, Dordrecht, 1988.

Winick, J. R., P. P. Wintersteiner, and R. H. Picard, Non-LTE emission from CO(v=1) in the mesosphere and lower thermosphere and its effect on remote sensing, Topical Meeting on Optical Remote Sensing of the Atmosphere, Incline Village, NV, 12-15 February, 1990.

Wintersteiner, P. P., and R. D. Sharma, Update of an efficient computer code (NLTE) to calculate emission and transmission of radiation through non-equilibrium atmospheres, *Rep. AFGL-TR-85-0240*, 155 pp., Air Force Geophysics Lab., Bedford, Mass., 1985, ADA172556.

Wintersteiner, P. P., and R. A. Joseph, Development of models for infrared emission in the upper atmosphere, *Rep. AFGL-TR-86-0163*, 91 pp., Air Force Geophysics Lab., Bedford, Mass., 1986, ADA173633.